

POLITECNICO DI MILANO

Facoltà di Ingegneria Industriale

Corso di Laurea Magistrale in  
Ingegneria Aeronautica



**An Hybrid Boundary Element Method  
for Free Surface Flows**

*Advisor:*

Prof. Luca FORMAGGIA

*Co-Advisor:*

Dott. Andrea MOLA

*Author:*

Nicola GIULIANI

Matr. 765684

Anno Accademico 2012-2013



*To Kate,  
sunshine in every rainy morning.*



# Contents

<b>Sintesi</b>	<b>13</b>
<b>Acknowledgements</b>	<b>23</b>
<b>Abstract</b>	<b>25</b>
<b>1 Introduction</b>	<b>27</b>
<b>2 Problem formulation for the Laplace equation</b>	<b>31</b>
2.1 Basic notation and governing equations . . . . .	31
2.2 Boundary Integral Formulation of the governing equations and BEM . . . . .	32
2.3 Discretization procedure and Isoparametric Collocation BEM . . . . .	34
2.4 Assembling the algebraic system . . . . .	36
<b>3 Preliminary validation</b>	<b>45</b>
3.1 Test Problem 1: Sphere . . . . .	46
3.1.1 Convergence Analysis . . . . .	47
3.1.2 Influence of the collocation points position in the hybrid method . . . . .	47
3.1.3 First order elements . . . . .	50
3.1.4 Second order elements . . . . .	53
3.1.5 Alternative implementation of Neumann condition . . . . .	56
3.2 Test Problem 2: Spheroid . . . . .	59
3.2.1 Convergence analysis . . . . .	60
3.2.2 First order elements . . . . .	60
3.2.3 First order elements. Convergence Analysis with isotropic grids . . . . .	62
3.2.4 Quadratic Elements. Convergence Analysis with isotropic grids . . . . .	66

3.2.5	Alternative implementation of Neumann condition . . . . .	68
3.2.6	Local refinement . . . . .	69
3.2.7	Hanging nodes . . . . .	70
3.2.8	Results . . . . .	71
3.3	Test Problem 3: solution over a sharp edge . . . . .	74
3.3.1	Convergence analysis . . . . .	75
<b>4</b>	<b>Free-Surface Flows</b>	<b>79</b>
4.1	Basic notation and governing equations . . . . .	80
4.2	Boundary Condition on the Free Surface . . . . .	82
4.3	Linearized Free Surface Boundary Condition . . . . .	83
4.4	Waves behavior . . . . .	86
<b>5</b>	<b>Test Cases</b>	<b>91</b>
5.1	Submerged prolate spheroid . . . . .	91
5.1.1	Treatment of the linearized free surface boundary condition .	93
5.1.2	Qualitative analysis of the wave pattern . . . . .	99
5.1.3	Free surface maximum variation and drag computation . . .	103
5.2	Wigley Hull . . . . .	106
5.2.1	Wigley Hull formulation . . . . .	106
5.2.2	Domain of the problem . . . . .	107
5.2.3	Qualitative analysis of the wave pattern . . . . .	108
5.2.4	Free surface elevation on the water line . . . . .	113
5.2.5	Local Refinement . . . . .	114
5.2.6	Free surface elevation on the water line with local refinement	116
5.2.7	Comparison with other models . . . . .	119
5.3	DTMB5415 . . . . .	121
5.3.1	Free surface elevation on the water line . . . . .	123
<b>6</b>	<b>Conclusions</b>	<b>127</b>

# List of Figures

1	Schema del dominio utilizzato nel caso di un corpo sommerso . . . . .	19
2	Schema del dominio utilizzato nel caso di un corpo che tagli la superficie libera . . . . .	20
2.1	Reference cell transformation . . . . .	39
2.2	Treatment for a cell on Diriclet boundary . . . . .	41
2.3	Treatment for a cell on Neumann boundary . . . . .	41
3.1	Sphere test case, global refinement strategy mesh . . . . .	46
3.2	Convergence analysis for $\phi$ . Different choices of points are compared in a linear isoparametric BEM . . . . .	49
3.3	Convergence analysis for $\partial\phi/\partial n$ . Different choices of points are compared in a linear isoparametric BEM . . . . .	49
3.4	Convergence analysis for $\phi$ for a linear isoparametric BEM on the sphere . . . . .	51
3.5	Convergence analysis for $\partial\phi/\partial n$ for a linear isoparametric BEM on the sphere . . . . .	52
3.6	Convergence analysis for $\phi$ for a second order isoparametric BEM on the sphere . . . . .	54
3.7	Convergence analysis for $\partial\phi/\partial n$ for a second order isoparametric BEM on the sphere . . . . .	55
3.8	Convergence analysis for $\phi$ for a linear isoparametric BEM on the sphere with weak formulation of Neumann conditions . . . . .	57
3.9	Convergence analysis for $\partial\phi/\partial n$ for a linear isoparametric BEM on the sphere, with weak formulation of Neumann conditions . . . . .	58
3.10	Spheroid test case, global refinement strategy mesh . . . . .	59
3.11	Convergence analysis for $\phi$ for a linear isoparametric BEM on the spheroid . . . . .	61
3.12	Convergence analysis for $\partial\phi/\partial n$ for a linear isoparametric BEM on the spheroid . . . . .	62
3.13	Spheroid test case, global refinement strategy mesh with anisotropies removed . . . . .	63

3.14	Convergence analysis for $\phi$ for a linear isoparametric BEM on the spheroid. The mesh anisotropies are removed . . . . .	64
3.15	Convergence analysis for $\partial\phi/\partial n$ for a linear isoparametric BEM on the spheroid. The mesh anisotropies are removed . . . . .	65
3.16	Convergence analysis for $\phi$ for a quadratic isoparametric BEM on the spheroid. The mesh anisotropies are removed . . . . .	67
3.17	Convergence analysis for $\phi$ for a linear isoparametric BEM on the spheroid. The mesh anisotropies are removed. The Neumann conditions are implemented in weak form. . . . .	68
3.18	Convergence analysis for $\partial\phi/\partial n$ for a linear isoparametric BEM on the spheroid. The mesh anisotropies are removed. The Neumann conditions are implemented in weak form. . . . .	69
3.19	Hanging node scheme . . . . .	70
3.20	Spheroid test case, locally refined mesh . . . . .	71
3.21	Convergence analysis for $\phi$ for a linear isoparametric BEM on the locally refined spheroid. The mesh anisotropies are removed. The Neumann conditions are implemented in weak form. . . . .	72
3.22	Convergence analysis for $\partial\phi/\partial n$ for a linear isoparametric BEM on the locally refined spheroid. The mesh anisotropies are removed. The Neumann conditions are implemented in weak form. . . . .	73
3.23	Edge test case, globally refined mesh . . . . .	74
3.24	Convergence analysis for $\partial\phi/\partial n$ for a linear isoparametric BEM on the edge. . . . .	76
3.25	Error visualization over the edge . . . . .	77
4.1	Vertical section of the domain for the simulation of the flow past a body beneath the water free surface. . . . .	79
4.2	Vertical section of the domain for the simulation of the flow past a boat located across the water free surface . . . . .	80
4.3	Typical Kelvin wake for a piercing surface body. Well defined V-shaped wake with typical featherlets. . . . .	86
4.4	The domain of the model for 2D waves . . . . .	87
4.5	Graphic construction of the Kelvin waves angle for a little wavenumber	89
4.6	Graphic construction of the Kelvin waves angle for a large wavenumber	89
5.1	Sketch of the domain for a submerged body . . . . .	92
5.2	View of prebuilt meshes in the spheroid case . . . . .	92
5.3	Importance of the SUPG stabilization . . . . .	99
5.4	Qualitative analysis of wave pattern around the spheroid for $Fr = 0.4$ .	100
5.5	Qualitative analysis of wave pattern around the spheroid for $Fr = 0.5$ .	101
5.6	Qualitative analysis of wave pattern around the spheroid for $Fr = 0.6$ .	101



5.7	Qualitative analysis of wave pattern around the spheroid for $Fr = 0.7$ .	102
5.8	Kelvin angle analysis for the submerged spheroid . . . . .	102
5.9	Maximum elevation of the free surface around the spheroid . . . . .	103
5.10	Wave coefficient computation . . . . .	105
5.11	Wigley Hull CAD. . . . .	106
5.12	Sketch of the domain for a surface piercing body . . . . .	107
5.13	Views of the prebuilt meshes around the Wigley hull. . . . .	108
5.14	Qualitative analysis of the wave pattern around the Wigley hull for $Fr = 0.250$ . . . . .	109
5.15	Qualitative analysis of the wave pattern around the Wigley hull for $Fr = 0.267$ . . . . .	109
5.16	Qualitative analysis of the wave pattern around the Wigley hull for $Fr = 0.289$ . . . . .	110
5.17	Qualitative analysis of the wave pattern around the Wigley hull for $Fr = 0.316$ . . . . .	110
5.18	Qualitative analysis of the wave pattern around the Wigley hull for $Fr = 0.354$ . . . . .	111
5.19	Qualitative analysis of the wave pattern around the Wigley hull for $Fr = 0.408$ . . . . .	111
5.20	Waterline analysis using the prebuilt mesh around the Wigley hull .	113
5.21	Locally refined mesh around the Wigley hull . . . . .	115
5.22	Waterline analysis using the locally refined mesh around the Wigley hull . . . . .	116
5.23	Linearized method comparison on Wigley hull . . . . .	117
5.24	Kelvin angle analysis for the Wigley hull . . . . .	118
5.25	Comparison of the waterline with the continuous BEM. . . . .	119
5.26	Comparison of the waterline with the non linear BEM. . . . .	120
5.27	DTMB5415 CAD . . . . .	121
5.28	Views of the prebuilt meshes around the DTMB5415 hull. . . . .	122
5.29	Final mesh around the DTMB5415 hull. . . . .	122
5.30	Waterline analysis using the locally refined mesh around the DTMB5415	123
5.31	Sketch of high curvature at the stern of the DTMB5415 . . . . .	124
5.32	Kelvin angle analysis for the DTMB5415 . . . . .	124



# List of Tables

3.1	Scheme 2D of the reference cell employed for the choice of the collocation points . . . . .	48
3.2	Scheme 2D of the reference cell employed for the first order analysis in the sphere test case. . . . .	50
3.3	Scheme 2D of the reference cell employed for the second order analysis in the sphere test case. . . . .	53
3.4	Scheme 2D of the reference cell employed for the first order analysis in the spheroid test case. . . . .	61
3.5	Scheme 2D of the reference cell employed for the first order analysis in the spheroid test case with weak implementation of Neumann condition. . . . .	64
3.6	Scheme 2D of the reference cell employed for the second order analysis in the spheroid test case. . . . .	66
3.7	Scheme 2D of the reference cell employed for the local refinement on the spheroid. . . . .	72
3.8	Scheme 2D of the reference cell employed on the sharp edge test case. . . . .	75
4.1	Kelvin angle for the 2D model . . . . .	90
5.1	Kelvin angle for the Wigley hull . . . . .	118
5.2	Kelvin angle for the DTMB5415 hull . . . . .	125



# Sintesi

Nell'ambito dell'ingegneria vi è sempre stato il bisogno di previsioni accurate delle prestazioni idrodinamiche delle navi. Queste sono fortemente influenzate dal campo ondoso generato dal moto dell'imbarcazione. Il costo computazionale, inerente alla risoluzione numerica delle equazioni di Navier–Stokes, ha stimolato lo studio di modelli più semplici in grado comunque di fornire previsioni accurate del flusso attorno ad uno scafo. Storicamente i modelli basati sull'uso del potenziale cinetico hanno avuto maggior successo nello studio della dinamica delle onde non frangenti.

Le ipotesi di fluido incomprimibile e flusso irrotazionale riducono le equazioni di conservazione della massa del sistema di Navier–Stokes all'equazione di Laplace mentre l'equazione di bilancio di quantità di moto diviene l'equazione di Bernoulli. Il sistema risultante da queste semplificazioni ha costi computazionali notevolmente ridotti rispetto a quello originale.

Il moto di un corpo vicino alla superficie libera produce un moto ondoso, se la superficie è trattata con un'opportuna condizione al contorno allora il modello a potenziale non solo è in grado di riprodurre in modo accurato questa situazione ma è anche in grado di stimare la resistenza all'avanzamento che viene esercitata sul corpo; visto che è una conseguenza del moto ondoso generato essa è detta resistenza d'onda.

L'equazione di Laplace viene spesso risolta tramite l'ausilio di metodi agli elementi al contorno (BEM) sfruttando la formulazione integro differenziale dell'equazione stessa. Quello che rende vantaggioso l'uso di questi metodi è il fatto di richiedere la discretizzazione solamente dei contorni del dominio, che è anche dove deve essere calcolata la pressione per ottenere la stima della resistenza d'onda.

Lo scopo del presente lavoro è lo sviluppo di un BEM in grado di calcolare accuratamente il moto ondoso sulla superficie libera attorno a un corpo in moto vicino ad essa. Condizioni linearizzate, fra quelle ritrovabili nella letteratura navale, sono state applicate sulla superficie libera; questo consente un'ulteriore semplificazione per lo studio iniziale del BEM che si intende sviluppare. Si è deciso di ricercare solamente la soluzione stazionaria cosicché da dover risolvere un solo sistema algebrico per ogni simulazione.

Quest'ultima semplificazione introduce anche una problematica in quanto porta alla scrittura di un sistema di equazioni simmetrico nella direzione di avanzamento del corpo in acqua. Questo porterebbe all'insorgere di onde non fisiche che si propagherebbero davanti al corpo. Negli ultimi cinquant'anni si sono prodotte numerose soluzioni a questo problema nell'ambito dell'ingegneria navale.

Il modo storicamente più usato si basa su una particolare formulazione del BEM dove viene definita una funzione di Green che soddisfi automaticamente le condizioni al contorno linearizzate sulla superficie libera. Tra gli altri si ricorda qui il lavoro di J.N.Newmann [21], F.Huang e C.Yang in [23]. Questa particolare funzione di Green è di difficile utilizzo e soprattutto anche di non banale integrazione. Sulla base di queste considerazioni nel 1977 C.W.Dawson sviluppò una formulazione BEM dove tutte le derivate nella direzione di avanzamento del corpo sono calcolate da differenze finite decentrate (upwind nella direzione del flusso). Oltre a questo suggerì anche una particolare decomposizione del flusso complessivo attorno al corpo in uno ottenuto con condizioni al contorno nulle sulla superficie libera e in una perturbazione rispetto a tale condizioni; questo approccio è seguito da C.Raven nella sua tesi di dottorato [24].

Tipicamente le derivate upwind nelle condizioni al contorno sono ottenute tramite differenze finite decentrate che sono però basate su una griglia strutturata. Nel presente lavoro si è invece scelto di usare una derivazione in forma debole unita a una stabilizzazione di tipo Streamline Upwind Petrov Galerkin(SUPG), che è spiegata da J.E.Akin in [1]. Questo approccio è basato sull'introduzione di termini addizionali nelle equazioni del flusso e consente l'uso di griglie di calcolo non conformi e non strutturate, questo fatto dà al metodo il vantaggio di poter usare strategie di raffinamento locali.

Il lavoro è suddiviso in due parti. Nella prima lo scopo è quello di sviluppare un nuovo codice in grado di realizzare un BEM ibrido per la risoluzione dell'equazione di Laplace considerando le incognite del problema come un'unica incognita vettoriale, usando quindi un approccio detto monolitico. Per la validazione di questo codice si usano dei casi test derivanti da [14, 19, 16] che non presentano il trattamento della superficie libera.

Nella seconda parte invece il metodo BEM sviluppato viene modificato per poter trattare i problemi a superficie libera, raffrontandosi sia con i risultati su uno sferoide sommerso ottenuti da D.C.Sculen in [25], sia con quanto ottenuto dall'università di Tokyo [18] nello studio dello scafo di Wigley. Come ultima analisi si riportano i risultati relativi a uno scafo complesso di interesse industriale, il DTMB5415; come raffronto si usano i dati ottenuti con un codice BEM non lineare [20].

Tutto il software utilizzato nel presente lavoro di tesi è sviluppato in ambiente C++ sfruttando alcune librerie OpenSource: `deal.II`, [3, 2], nell'approssimazione degli elementi al contorno e `OpenCASCADE`, [6], per il trattamento del disegno CAD

dello scafo. Il lavoro è stato sviluppato in collaborazione con il laboratorio Matlab presso SISSA a Trieste.

Una sintesi dei contenuti del lavoro viene riportata nei seguenti paragrafi.

**Capitolo 2** In questo capitolo viene fornita una descrizione del metodo a elementi a contorno (BEM) che si è sviluppato durante il lavoro di tesi. Esso riguarda la risoluzione dell'equazione di Laplace con condizioni al contorno miste. Per poter verificare che il BEM sviluppato sia in grado di risolvere adeguatamente il sistema in esame verranno affrontati tre semplici casi test, in cui viene affrontato un problema esterno ad un corpo di superficie  $\Omega$

$$\Delta\phi = 0 \quad \text{in } \mathbb{R}^n \setminus \Omega \quad (1)$$

$$\frac{\partial\phi}{\partial n}(\mathbf{x}) = h(\mathbf{x}) \quad \text{on } \Gamma_N \quad (2)$$

$$\phi(\mathbf{x}) = g(\mathbf{x}) \quad \text{on } \Gamma_D \quad (3)$$

$$\lim_{|r| \rightarrow \infty} \phi(r) = \phi_\infty. \quad (4)$$

Il BEM viene scritto tramite l'uso della formulazione integrale dell'equazione di Laplace, ottenuta grazie alla seconda identità di Green. Viene quindi discretizzata la sola superficie  $\Omega$ , e questo grazie alla scelta di un metodo a elementi al contorno. Una volta che è fissata la rappresentazione discreta del dominio  $\Gamma$  la scelta naturale è utilizzare la stessa discretizzazione anche per il potenziale  $\phi$  approssimato in modo continuo. Grazie a questa sua caratteristica il metodo utilizzato è detto BEM isoparametrico.

Si è deciso di implementare un BEM ibrido cioè le incognite del problema, il potenziale  $\phi$  e la sua derivata normale  $\partial\phi/\partial n$ , sono approssimate diversamente in quanto la prima segue una classica implementazione continua mentre la seconda è rappresentata in modo discontinuo. Questo è fatto per il seguente motivo: se il vettore normale alla superficie  $\mathbf{n}$  è discontinuo, cosa molto comune in domini complessi come quelli trattati nella seconda parte della presente tesi, lo è anche la derivata normale del potenziale. Il modo più comune per riuscire a calcolare le incognite del problema è quello di usare un metodo di collocazione: l'equazione integrale ottenuta in precedenza viene soddisfatta in un numero di punti pari al numero di incognite in modo da ottenere un sistema ben posto. Tale scelta è seguita in questo lavoro e come punti di collocazione sono usati i gradi di libertà sulla cella di riferimento una volta che sono stati mappati sulla superficie reale discretizzata; questi punti sono detti nodi o punti di supporto. Abbiamo deciso di utilizzare un BEM ibrido detto monolitico, cioè assembliamo una sola matrice in cui tutti i valori di  $\phi$  e  $\partial\phi/\partial n$  sono considerati come incogniti e dove le condizioni al contorno sono imposte agendo algebricamente sulle righe della matrice. Siccome il BEM

è ibrido l'approssimazione scelta per il potenziale non coincide con quella per la derivata normale e quindi la scrittura di un BEM monolitico, in cui tutti i gradi di libertà vengono trattati come incognite, risulta di più immediata implementazione rispetto alla forma classica in cui vengono prima applicate le condizioni al contorno e successivamente viene scritto un sistema per le sole incognite.

In questo capitolo è presentata anche una maniera alternativa di imporre le condizioni al contorno di tipo Neumann in forma debole, questa parte dalla considerazione che in molti problemi non sia nota la soluzione esatta di  $\partial\phi/\partial n$  e quindi si sfrutta il fatto che questa derivata sia uguale al gradiente del potenziale per la normale alla superficie, cioè  $\partial\phi/\partial n = \nabla\phi \cdot \mathbf{n}$ . Inoltre il valore della normale non è noto sugli spigoli della cella, dove sono però posti i gradi di libertà di un' approssimazione continua, difatti la normale solitamente è noto unicamente all'interno della cella, con questa tecnica si sfrutta la conoscenza di  $\nabla\phi$  e  $\mathbf{n}$  nei punti di quadratura all'interno della cella. Per quanto riguarda la scelta dei gradi di libertà per l'approssimazione discontinua della derivata normale ci si rifà a quanto esposto nella sezione 3.1.2 della presente tesi.

**Capitolo 3** In questo capitolo viene validato il metodo BEM sviluppato tramite il confronto con tre semplici casi test.

1. Per prima cosa viene affrontato lo studio del potenziale attorno a una sfera di raggio  $R = 1$  come riportato da [9, 14, 19]. In questo caso test si effettua una serie di raffinamenti globali in maniera da fornire un'analisi di convergenza. Vista l'estrema semplicità, anche geometrica, di questo primo esempio le stesse analisi vengono ripetute su un secondo caso più complesso. Siccome si vuole analizzare la convergenza del metodo sia per quanto riguarda il potenziale che la sua derivata normale si è scelto di imporre condizioni di Dirichlet se  $y < 0$  e di Neumann se  $y \geq 0$ .

Quando viene effettuata un' analisi con elementi del prim'ordine il potenziale  $\phi$  è approssimato con elementi lineari di forma quadrangolare, mentre viene cambiata l'approssimazione per la derivata normale  $\partial\phi/\partial n$ . Per quanto riguarda  $\phi$  il metodo converge al secondo ordine utilizzando il metodo di riferimento che utilizza anche per  $\partial\phi/\partial n$  l'approssimazione continua usata per il potenziale, lo stesso ordine è ripreso anche dai due BEM ibridi analizzati. Gli stessi ordini di convergenza sono recuperati anche usando l'implementazione in forma debole delle condizioni di Neumann. In valore assoluto invece è interessante notare come siano lievemente migliori i risultati ottenuti con l'imposizione in forma debole delle condizioni di Neumann. Per dimostrare che il metodo sviluppato sia in grado di considerare anche approssimazioni con elementi non lineari viene sviluppata anche un'analisi di convergenza di ordine 2. In tutti i casi considerati il potenziale  $\phi$  è approssimato con



elementi quadratici continui, mentre viene cambiata l'approssimazione per la derivata normale  $\partial\phi/\partial n$ . Le condizioni di Neumann non sono implementate in forma debole ma sfruttando l'implementazione classica. Per quanto riguarda la convergenza del potenziale  $\phi$  alla soluzione esatta, la soluzione di riferimento, con anche  $\partial\phi/\partial n$  approssimato in modo continuo, e la soluzione con approssimazione quadratica discontinua per la derivata normale convergono con un ordine pari a 4. Il BEM ibrido con  $\partial\phi/\partial n$  approssimata in maniera lineare discontinua invece ha una convergenza del terz'ordine mentre quello ottenuto mediante un' approssimazione costante a tratti della derivata solamente al second'ordine. Per quanto riguarda  $\partial\phi/\partial n$  solo la soluzione di riferimento mantiene un ordine di convergenza al quart'ordine; i tre BEM ibridi considerati presentano convergenza di ordine  $\sim 2$ .

Questi ordini di convergenza estremamente positivi potrebbero essere dovuti ad un fenomeno di superconvergenza dato dalla semplicità di questo primo caso test.

2. Viene considerato il potenziale attorno uno sferoide allungato, la soluzione di riferimento è riportata in [16]. Lo sferoide presenta i suoi assi principali allineati con gli assi del sistema di riferimento, i semiassi lungo  $x, y$  sono lunghi 1 mentre il semiasse lungo  $z$  è lungo 2. Lo sferoide non presenta tutte le simmetrie della sfera ed è quindi un buon caso test per verificare se l'imposizione delle condizioni di Neumann in forma debole, così come presentata in questo lavoro, sia una valida alternativa al metodo classico di imporre tali condizioni, e se gli elevati ordini di convergenza del BEM isoparametrico di ordine 2 siano merito del metodo sviluppato o di un fenomeno di superconvergenza. Per quanto riguarda l'analisi del prim'ordine si mantengono gli stessi ordini di convergenza ottenuti sulla sfera. Si può notare come l'implementazione in forma debole delle condizioni di Neumann riesca ad ottenere risultati migliori per quanto riguarda la convergenza di  $\partial\phi/\partial n$ . Si ricorda a questo punto che l'approssimazione discontinua lineare per la derivata normale del potenziale ha costi computazionali superiori alle altre e non sembra riuscire a ottenere risultati quantitativamente migliori. Per quanto riguarda l'analisi di convergenza con elementi di ordine superiore al primo le convergenze del quart'ordine ottenute con il dominio sferico non sono ritrovate sullo sferoide, dove il caso continuo di riferimento si attesta su una convergenza al terz'ordine su  $\phi$  e quasi del terz'ordine su  $\partial\phi/\partial n$ . La migliore approssimazione ibrida risulta essere quella lineare discontinua che ottiene convergenze di terzo e second'ordine rispettivamente su  $\phi$  e  $\partial\phi/\partial n$ . Si ricorda a questo punto che l'approssimazione quadratica discontinua della derivata normale del potenziale ha costi computazionali superiori sia di quella continua di riferimento sia degli altri BEM ibridi e non ottiene migliori ordini

di convergenza. Come ultima cosa sullo sferoide viene testata una tecnica di raffinamento locale ottenuta stimando l'errore con un estimatore introdotto da Kelly, Gago, Zienkiewicz e Babuska e riportato in [17]. Questo estimatore di errore calcola il salto delle variabili attraverso i lati della cella. Questa tecnica di raffinamento non porta a risultati quantitativamente migliori in questo semplice caso test ma comunque offre risultati attendibili che ne giustificano l'uso su esempi più complicati come quelli affrontati nei capitoli successivi.

3. L'ultimo caso test tratta una peculiarità del BEM. Quando sono presenti degli spigoli nel dominio la normale alla superficie ha un salto, questo causa un errore se l'approssimazione usata per  $\partial\phi/\partial n$  è continua. Per riprodurre una mesh con un consistente salto di normale si è scelto uno sferoide con aspect ratio pari a 4 se  $z \geq -0.4$  e una sfera di raggio 2.5 centrata in  $(0, 0, 1.89)$  se  $z < 0.4$ . L'errore nel caso continuo non è concentrato dove la soluzione ha maggiori variazioni ma anche sullo spigolo, mentre nel caso BEM ibrido l'errore sullo spigolo è molto contenuto. Riuscire a recuperare il corretto valore di  $\partial\phi/\partial n$  sullo spigolo gioca un ruolo fondamentale nei flussi a superficie libera dove il valore sullo spigolo tra scafo e superficie libera serve a calcolare la linea d'acqua su di esso.

**Capitolo 4** In questo capitolo si introduce il problema di un flusso a superficie libera. Si è scelto di studiare il flusso di un oggetto in moto uniforme in acqua calma nelle vicinanze della superficie libera. Nel presente lavoro si considera come dominio solo l'acqua trascurando quindi di discretizzare l'aria e la parte emersa dell'oggetto. Il problema è descritto dalle note equazioni di Eulero della fluidodinamica, il termine inerziale legato all'accelerazione  $\mathbf{g}$  ricopre un ruolo fondamentale nella dinamica delle onde che si creano sul pelo dell'acqua che infatti sono anche chiamate onde gravitazionali. Si considera il flusso composto da due velocità, quella della corrente indisturbata  $\mathbf{V}_\infty$  e quella di perturbazione dovuta alla presenza del corpo  $\mathbf{V}_p$ . Visto che si è deciso di trascurare gli effetti della viscosità, considerati confinati in uno strato limite di spessore trascurabile, si considera il flusso come irrotazionale. La dinamica del sistema è recuperata a posteriori, visto che l'equazione di conservazione della massa è indipendente da quella di conservazione della quantità di moto, quando è già noto il valore di  $\phi$ . In questo modo si possono calcolare le azioni sul corpo dovute alla creazione del campo ondosio. E' necessario scrivere una condizione al contorno sulla superficie, due ipotesi forti vengono introdotte riguardo al suo comportamento: che la superficie libera sia una funzione cartesiana a singolo valore e che la pressione su di essa sia sempre eguale alla pressione atmosferica. La condizione completa, non stazionaria e non lineare, sulla superficie libera viene quindi linearizzata considerando solo le soluzioni

stazionarie, ottenendo la condizione effettivamente imposta nel presente lavoro. In questo capitolo viene presentato anche un modello semplificato per spiegare la morfologia di una tipica scia di un corpo in moto vicino ad una superficie libera come presentato da Frank S. Crawford in [7].

**Capitolo 5** Il BEM sviluppato nei precedenti capitoli viene modificato per poter venire applicato a flussi a superficie libera. Si è scelto di usare una derivazione in forma debole assieme ad una stabilizzazione di tipo SUPG, [1], alle derivate in  $x$  recuperando l'idea avuta da Dawson nel 1977 in [8] e ripresa da Raven in [24], mantenendo però la formulazione tradizionale del BEM con l'uso della sorgente di Rankine per evitare ulteriori complicazioni. Per poter imporre la condizione linearizzata sulla superficie libera si è scelto di aggiungere una nuova incognita al problema e cioè la derivata di  $\phi$  in direzione  $x$  e cioè  $\partial\phi/\partial x$  che può venire approssimata sia in modo continuo che discontinuo. Viene usata una derivazione in forma debole simile a quella utilizzata per l'imposizione delle condizioni di Neumann. Per tutti i casi analizzati si è deciso, a valle delle analisi di convergenza del terzo capitolo, di considerare: per  $\phi$  un' approssimazione lineare continua, per  $\partial\phi/\partial n$  un' approssimazione discontinua costante a tratti per evitare errori concentrati sugli spigoli del dominio, per  $\partial\phi/\partial x$  la stessa approssimazione continua usata per  $\phi$ .

Vengono considerati tre problemi modello tipici dell'ingegneria navale.

1. Come primo caso viene considerato uno sferoide allungato che presenta i suoi tre assi principali allineati con gli assi del sistema di riferimento. L'asse lungo  $x$  ha lunghezza 10, quelli lungo  $y$  e  $z$  sono invece lunghi 2. E' immerso in acqua ad una profondità pari a 0.5 metri.

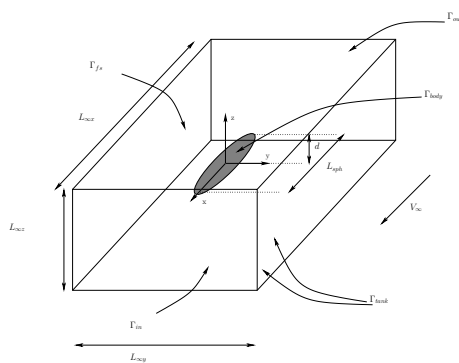


**Figure 1:** Lo sferoide allungato è posto sotto il pelo dell'acqua ad una profondità ben precisa, è possibile vedere anche la vasca esterna a  $L_{\infty x}, L_{\infty y}, L_{\infty z}$ . Il flusso entra da  $\Gamma_{in}$ ,  $\Gamma_{tank}$  rappresenta le superfici laterali della vasca e il suo fondo

Per prima cosa viene effettuata un'analisi qualitativa del campo di onde generato attorno al corpo: i risultati sono consistenti con quanto si ritrova sperimentalmente. Si può osservare come la classica forma a V della scia di Kelvin sia molto più marcata all'aumentare della velocità. Questa prima analisi permette di capire come il BEM sviluppato sia in grado di riprodurre uno degli effetti più importanti della vera scia di Kelvin. Dal punto di vista quantitativo si confronta la massima altezza della superficie libera con quanto ottenuto in [25] usando lo stesso tipo di sferoide sommerso, ma con un metodo stazionario e non lineare. Il metodo sviluppato riproduce l'andamento atteso ma sottostima l'ampiezza delle onde. Si compara anche il coefficiente di resistenza a quello teorico presentato da Havelock in [13]. Il BEM ibrido sviluppato in questo lavoro riproduce molto bene, anche per questa seconda analisi, l'andamento non monotono della curva ma ne continua a sottostimare il valore. Questo è coerente con la sottostima evidenziata in precedenza dell'altezza massima delle onde.

2. Come secondo caso si analizza uno scafo di Wigley e quindi un corpo che tagli la superficie libera

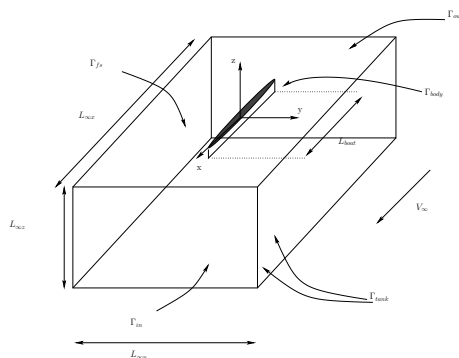


**Figure 2:** Lo scafo di Wigley è posto al centro della superficie libera  $z = 0$ , è possibile vedere anche la vasca esterna a  $L_{\infty x}$ ,  $L_{\infty y}$ ,  $L_{\infty z}$ . Il flusso entra da  $\Gamma_{in}$ ,  $\Gamma_{tank}$  rappresenta le superfici laterali della vasca e il suo fondo

Per prima cosa si effettua una prima analisi qualitativa analoga a quella effettuata sullo sferoide, e che dimostra come il BEM ibrido monolitico isoparametrico sviluppato sia in grado di cogliere alcuni effetti tipici della scia di Kelvin attorno ad un'imbarcazione. Si riporta quindi il raffronto quantitativo tra il metodo sviluppato e i risultati sperimentali dell'università di Tokyo [18]. Vengono utilizzate due diverse tipologie di griglie di calcolo: una mesh precostruita e una mesh frutto di 4 cicli di raffinamento locale usando lo stesso estimatore d'errore introdotto nel terzo capitolo. La mesh

utilizzata in una prima analisi è più raffinata dove ci si aspetta che le onde della scia a V di Kelvin siano presenti. Sullo scafo le due mesh sono uguali e cioè hanno 4 celle in altezza e 32 in lunghezza lungo lo scafo. Il metodo sviluppato riproduce in modo corretto l'onda lungo lo scafo, i picchi in orizzontale sono nelle posizioni corrette e la lunghezza di questa onda aumenta all'aumentare del numero di Froude e questa è una caratteristica fondamentale del fenomeno fisico che si sta riproducendo. Il metodo però sottostima l'entità dei picchi e presenta una forte instabilità evidente soprattutto per i numeri di Froude maggiori. Questa instabilità potrebbe essere accentuata dalla scelta dei sottospazi discreti utilizzati per la soluzione. Altre scelte di sottospazi vengono provate in questo momento. La sottostima dell'altezza dei picchi è riconducibile al metodo linearizzato adottato, questa infatti è riportata anche in [24]. Dal punto di vista qualitativo si può osservare la doppia scia di Kelvin attorno allo scafo di Wigley che anche in questo caso, coerentemente con le rilevazioni sperimentali, mantiene un angolo praticamente costante all'aumentare del numero di Froude.

3. Come ultimo caso si analizza uno scafo derivante da un CAD non analitico, questo grazie all'integrazione nel codice di funzioni della libreria OpenCASCADE [6]. Lo scopo è di verificare se il metodo BEM sviluppato sia effettivamente in grado di trattare una geometria complessa. Per questo scopo si sceglie lo scafo DTMB5415, modello sviluppato negli anni '80 come nave da combattimento della marina. Il dominio utilizzato per il calcolo è lo stesso usato per lo scafo di Wigley. Viene scelto un affondamento tale per cui la poppa piatta non sia immersa in acqua e questo per evitare la presenza di un'estesa zona turbolenta a valle della poppa stessa, cosa che il BEM sviluppato ancora non è in grado di trattare. Non essendo presenti dati sperimentali per questo affondamento si operano i raffronti con quanto si può ottenere utilizzando un BEM non lineare e non stazionario come presentato in [20]. Ancora una volta l'onda lungo lo scafo è riprodotta in modo corretto, i picchi vengono sottostimati ma in maniera minore rispetto a quanto accadeva sullo scafo di Wigley. In questo caso le differenze sono dovute anche alla linearizzazione delle condizioni al contorno sulla superficie libera che si è adoperata nel nostro metodo: essa considera la superficie libera ferma e quindi le onde non sono portate a seguire le curvature dello scafo che in questo caso non sono trascurabili.

Riassumendo, il metodo ibrido agli elementi al contorno sviluppato nella presente tesi è in grado di riprodurre i medesimi risultati di un tipico metodo continuo su dei casi test riguardanti la risoluzione di un problema esterno per l'equazione di Laplace.

Il metodo è stato poi modificato in modo da poter trattare un flusso a superficie libera, per semplicità di calcolo si è scelta l'implementazione di condizioni al contorno linearizzate sulla superficie libera. Nell'implementazione di queste condizioni è stata utilizzata una stabilizzazione di tipo SUPG che consente, contrariamente ai classici schemi upwind alle differenze finite, un naturale impiego di griglie non strutturate e non conformi. Nei flussi a superficie libera considerati questa possibilità gioca un ruolo chiave per contenere il numero di gradi di libertà. Nei tre casi affrontati il nostro metodo ha dimostrato di riprodurre alcuni aspetti essenziali del fenomeno fisico in esame come l'angolo di apertura della scia di Kelvin oppure il variare della lunghezza d'onda sulla linea dello scafo. Il metodo è inoltre in grado di trattare il CAD di uno scafo non analitico. Vengono però sottostimati i picchi delle onde anche se in questo caso le imprecisioni del metodo linearizzato appaiono meno rilevanti.

Lo scopo principale della presente tesi era di indagare la possibilità di impiegare metodi BEM ibridi nello studio di flussi a superficie libera. I risultati ottenuti in questo senso sono soddisfacenti, è chiaro che per un eventuale sviluppo di tipo industriale sono necessari ulteriori studi riguardo all'approssimazione discontinua di  $\partial\phi/\partial n$ , in modo da eliminare l'oscillazione presente nel caso di corpo che tagli la superficie libera.

Altro aspetto che si vuole aggiungere al codice sviluppato fino ad ora è la capacità di trattare flussi con poppa bagnata. In questi casi la poppa verticale impone al flusso un'ampia regione in cui le ipotesi di flusso a potenziale non sono più valide, per questo è necessario trattare tali zone in maniera specifica. Questa trattazione non era però oggetto di questo studio iniziale dei metodi BEM ibridi applicati a flussi a superficie libera.

Si ritiene che una scelta ottimizzata degli spazi discreti possa stabilizzare ulteriormente il problema, per questa ragione nuove combinazioni di spazi vengono provate al momento. Anche la ricerca di uno stimatore di errore ottimizzato viene studiata per limitare le oscillazioni nella soluzione. Infine per ridurre il tempo di calcolo una scelta possibile è cambiare il metodo di soluzione del sistema lineare da UMFPACK a GMRES. Il secondo ha un costo computazionale minore specie per alti numeri di gradi di libertà ma richiede lo studio di un preconditionatore per risolvere il sistema, e questo non era fra gli obiettivi del presente lavoro.

## Acknowledgements

In first place I would like to thank my advisor, Professor Luca Formaggia for the numerous suggestions and hints all along the developing of the present thesis. This work would not have been possible without the help and the continuous support of my co-advisor Dott. Andrea Mola. I hope that our work cooperation will proceed in the future.

Then I want to thank Professor Antonio De Simone and the rest of the SISSA mathlab who have made me feel comfortable from the very first moment. A particular thanks goes to Assistant professor Luca Heltai who has guided me through the hardest programming moments and to Dott. Giovanni Noselli who has helped not to worry when things went wrong.

The greatest thanks are for my parents, you have always let me search my own way, you have always supported me and for that I will be forever thankful. Without your help I would not be where I've arrived and these moments would not exist.





## Abstract

A hybrid Boundary Element Method to solve the Laplace equation is presented. The method solves the Boundary Integral Equation coming from the Laplace equation. Both Neumann and Dirichlet boundary conditions are presented. The Neumann boundary conditions are implemented also in a weak formulation. This formulation is inserted into the algebraic system of the hybrid BEM in an innovative way. We present the convergence analysis of the method applied to three known reference solution.

Then the hybrid BEM is modified in order to treat free surface flow, namely the case of a body in motion in water. Both a submerged body and a surface piercing body are considered. Linearized free surface boundary conditions are implemented. A Streamline Upwind Petrov Galerkin stabilization is used to implemented the linearized free surface condition. This allows us to use non conformal unstructured grids.

**Keywords:** hybrid boundary element method, high order elements, edge treatment, weak Neumann boundary conditions, linearized free surface, submerged spheroid, Wigley hull, DTMB5415



# Chapter 1

## Introduction

In nautical engineering there has always been the need for accurate prediction of the hydrodynamic performance of ships. The elevated computational cost of Navier–Stokes equations is nowadays prompting the studies on reduced order models able to give reliable predictions of the flow around the hulls. In particular, models based on potential flow theory have historically been among the most successful in the simulation of the dynamics of non breaking waves.

The assumptions of incompressibility and irrotational flow respectively reduce Navier–Stokes mass conservation and momentum balance equation to the less computationally intensive Laplace’s and Bernoulli’s equations. The motion of a body near the free surface creates a wave pattern.

According to D’Alembert paradox, such model would not be able to predict any drag force exerted by the fluid on the moving hull. Yet, if complemented with a reliable free surface treatment, a potential model is able to reproduce with sufficient accuracy the wave elevation pattern generated by the boat motion. As a consequence it is able to predict the resistance component due to wave generation, which accounts for a fraction of the total drag of a boat.

Over the last decades the Laplace equation has often been solved using a boundary integral formulation, and indeed in many fields of engineering it is quite common to solve the Laplace equation through the Boundary Element Method(BEM).

What makes the BEM appealing for the present application is the fact that it requires only the discretization of the domain boundaries, which is where the pressure has to be evaluated and integrated to obtain the wave drag. This leads to a considerable reduction of the computational cost, as no effort is done to calculate the solution far from the boundaries, where it is not needed.

The purpose of the present work is then to develop a collocation BEM application that can compute accurately the wave pattern around surface piercing or submerged bodies in steady motion. The linearized free surface potential model has been here chosen among the possible potential models available in the literature.

In this early stage of the development of a BEM application in fact, this choice allowed a simplification of the implementation. In addition, only the steady solution is searched so that a single algebraic BEM system needs to be solved for each simulation.

Searching only the steady state solution of the linearized problem leads to a peculiar situation since the resulting equations are completely symmetric in the direction longitudinal to the main flow. For this reason, a set of non physical waves arises upstream of the body, unless proper radiation conditions are implemented to select the meaningful solution of the problem, see [25], and to prevent the propagation of unphysical waves upwards the flow.

In naval engineering this approach has been frequently used in the last fifty years, and many methods have been developed and documented in the literature(see [24, 4, 25]). The most classical approach is to implement a BEM formulation in which peculiar Green functions are defined, so as to automatically satisfy the linearized free surface boundary condition. Among others the works of R.W.Yeung in [26], J.N.Newmann in [21], F.Noblesse, F.Huang, C.Yang in [23] should be mentioned. In [4] K. A. Belibassakis *et al.* employed this peculiar implementation to obtain fairly accurate results in comparison to experimental data.

It is clear though, that the usage is not trivial, and in particular the integration over cells of these Green functions. Moving from such a consideration, in 1977 C.W. Dawson suggested in [8] a different BEM approach in which all the derivatives in the main stream direction that appear in the linearized free surface boundary condition were computed by means of upwind finite difference formulas, so as to suppress upstream propagating waves. He also suggested the usage of a particular potential decomposition in terms of a main double body flow and perturbation potential that is particularly effective for low velocity flows. This approach is followed also by Hoyte C. Raven in his PhD thesis [24]. Typically, [8] and [24], the upwind derivatives are implemented through a finite difference scheme based on a structured mesh. In the present work, the derivative are computed in weak form. An upwinding technique is proposed, but it is realized by means of a Streamline Upwind Petrov Galerkin (SUPG) stabilization that follows what is well explained by J. E. Akin in [1]. Being based on the introduction of additional terms in the flow equations, the SUPG stabilization allows for unstructured non conformal grids. This possibility is of great advantage, as it allows for the application of local refinement strategies.

In the present work a collocation hybrid BEM application is developed to perform free surface flow simulation past floating or submerged bodies moving in calm water. In particular, the specific hybrid formulation here proposed is first described and tested, on simple geometrical configurations not involving the treatment of a free surface. The BEM developed is able to treat mixed boundary condition,

both Neumann and Dirichlet, and has been tested on three test cases derived from [9, 19, 16].

Then the hybrid BEM is applied to a free surface flow problem. The cases considered are a submerged prolate spheroid, a Wigley hull and a DTMB5415 in steady motion in water. These three cases are common benchmarks in naval engineering literature.

The software used in the present work has been developed using the C++ programming language and two available open source libraries, `deal.II`, [3, 2], for what involves the boundary element approximation, and `OpenCASCADE`, [6], for the creation of meshes from hull CAD files.

The organization of this thesis goes as follows. Chapter 2 gives an explanation of the boundary integral formulation of the Laplace equation. Chapter 2 also presents the numerical discretization and the assembling of the Boundary Element Method algebraic system. Chapter 3 presents the three test cases employed to validate the developed hybrid BEM code. Chapter 4 introduces the complete boundary conditions needed to treat free surface flows and gives a simple explanation of the wave system around an object moving in calm water. Successively, it presents a linearization of the free surface boundary condition. The first part of Chapter 5 treats the case of the motion of a submerged prolate spheroid proposed by David C. Scullen in [25]. The second part of Chapter 5 presents instead the test case of the Wigley hull and the comparison of the computed water wave elevations on the hull surface. These results are compared with the results of the corresponding experimental work carried out at Tokyo University [18]. The last part of Chapter 5 shows the behavior of the developed BEM on a non analytical boat, the DTMB5415. The results are compared to what can be obtained with a fully non linear unsteady method, presented in [20].



# Chapter 2

## Problem formulation for the Laplace equation

This first chapter focuses on the Laplace equation and its discretization via the Boundary Element Method. The Laplace equation is first introduced along with a set of boundary conditions which ensure the well posedness of the partial differential problem in 3D domains. Then it will be shown how the Laplace equation is reformulated into a boundary integral equation. Finally the discretization strategy is presented.

### 2.1 Basic notation and governing equations

The Laplace equation can be solved in a closed bounded domain called  $\Omega$ . Dirichlet and Neumann boundary conditions are imposed on the portions  $\Gamma_D$ , and  $\Gamma_N$  of  $\partial\Omega$ , such that  $\Gamma_D \cup \Gamma_N = \partial\Omega$ ,  $\Gamma_D \cap \Gamma_N = \emptyset$ , and  $|\Gamma_D| \neq \emptyset$ .

$$\Delta\phi = 0 \qquad \text{in } \Omega \qquad (2.1a)$$

$$\frac{\partial\phi}{\partial n} = h(\mathbf{x}) \qquad \text{on } \Gamma_N \qquad (2.1b)$$

$$\phi = g(\mathbf{x}) \qquad \text{on } \Gamma_D. \qquad (2.1c)$$

Another possibility is to consider the solution over an unbounded region, namely the space surrounding a region  $\Omega$ . The problems tackled in this first chapter are of this type. Thus the Laplace equation is solved on  $\mathbb{R}^n \setminus \Omega$ , introducing the same

decomposition of  $\partial\Omega$  seen before

$$\Delta\phi = 0 \quad \text{in } \mathbb{R}^n \setminus \Omega \quad (2.2a)$$

$$\frac{\partial\phi}{\partial n} = h(\mathbf{x}) \quad \text{on } \Gamma_N \quad (2.2b)$$

$$\phi = g(\mathbf{x}) \quad \text{on } \Gamma_D \quad (2.2c)$$

$$\lim_{|r| \rightarrow \infty} \phi(r) = \phi_\infty. \quad (2.2d)$$

Where  $h(\mathbf{x})$ , and  $g(\mathbf{x})$  represent the boundary values for  $\phi$ , and  $\partial\phi/\partial n$  respectively. These problems are well posed because the presence of the Dirichlet boundary conditions ensures uniqueness to the solution.

## 2.2 Boundary Integral Formulation of the governing equations and BEM

Now, following [9], the Laplace equation (2.2a) is reformulated using the second Green identity

$$\int_{\mathbb{R}^n \setminus \Omega} (-\Delta\phi)G \, dx - \int_{\partial\Omega \cup \Gamma_\infty} \frac{\partial\phi}{\partial \mathbf{n}} G \, ds = \int_{\mathbb{R}^n \setminus \Omega} (-\Delta G)\phi \, dx - \int_{\partial\Omega \cup \Gamma_\infty} \phi \frac{\partial G}{\partial \mathbf{n}} \, ds \quad (2.3)$$

where  $\mathbf{n}$  is the normal to  $\partial\Omega$  pointing towards the fluid, *i.e.* towards  $\mathbb{R}^n \setminus \Omega$ .  $G$  is called the Green operator. Notice that the integral  $\int_{\Gamma_\infty} f \, ds$  should be interpreted in the following sense:

$$\int_{\Gamma_\infty} f \, ds := \lim_{r \rightarrow \infty} \int_{\partial B_r(0)} f \, ds,$$

where  $\partial B_r(0)$  indicates a sphere centered in the origin with radius  $r$ . The Green operator here employed is the Rankine source, given by:

$$G(\mathbf{x} - \mathbf{y}) = -\frac{1}{2\pi} \ln |\mathbf{x} - \mathbf{y}| \quad \text{for } n = 2, \quad (2.4)$$

$$G(\mathbf{x} - \mathbf{y}) = \frac{1}{4\pi} \frac{1}{|\mathbf{x} - \mathbf{y}|} \quad \text{for } n = 3. \quad (2.5)$$

The Rankine source satisfies, in distributional sense, the equation

$$-\Delta G(\mathbf{x} - \mathbf{y}) = \delta(\mathbf{x} - \mathbf{y}), \quad (2.6)$$



where the differentiation in the left hand side is done with respect to  $\mathbf{x}$ . Making use of equation (2.6) the boundary integral equation (2.3) can be rewritten as:

$$\begin{aligned}\phi(\mathbf{x}) &= - \int_{\partial\Omega \cup \Gamma_\infty} G(\mathbf{x} - \mathbf{y}) \frac{\partial\phi}{\partial\mathbf{n}_y}(\mathbf{y}) ds_y + \int_{\partial\Omega \cup \Gamma_\infty} \frac{\partial G(\mathbf{x} - \mathbf{y})}{\partial\mathbf{n}_y} \phi(\mathbf{y}) ds_y \\ &= \phi_\infty - \int_{\partial\Omega} G(\mathbf{x} - \mathbf{y}) \frac{\partial\phi}{\partial\mathbf{n}_y}(\mathbf{y}) ds_y + \int_{\partial\Omega} \frac{\partial G(\mathbf{x} - \mathbf{y})}{\partial\mathbf{n}_y} \phi(\mathbf{y}) ds_y\end{aligned}\quad (2.7)$$

for all  $\mathbf{x} \in \mathbb{R}^n \setminus \Omega$ . We have employed the fact that  $\lim_{\mathbf{x} \rightarrow \infty} \phi(\mathbf{x}) = \phi_\infty \in \mathbb{R}$ . Only the background field in fact has to be considered on  $\Gamma_\infty$ :

$$\int_{\Gamma_\infty} \frac{\partial G(\mathbf{x} - \mathbf{y})}{\partial\mathbf{n}_y} \phi(\mathbf{y}) ds_y = - \lim_{r \rightarrow \infty} \int_{\partial B_r(0)} \frac{\mathbf{r}}{r} \nabla G(\mathbf{x} - \mathbf{y}) \phi_\infty ds_y = \phi_\infty.$$

Equation (2.7) can be rewritten in a more compact form introducing the Single Layer Potential (S) and the Double Layer Potential (D) operators:

$$(S\dots) = \int_{\partial\Omega} G(\mathbf{x} - \mathbf{y}) \dots ds_y \quad (2.8a)$$

$$(D\dots) = \int_{\partial\Omega} \frac{\partial G(\mathbf{x} - \mathbf{y})}{\partial\mathbf{n}_y} \dots ds_y \quad (2.8b)$$

$$\phi(\mathbf{x}) = \phi_\infty - \left( S \frac{\partial\phi}{\partial\mathbf{n}_y} \right) (\mathbf{x}) + (D\phi)(\mathbf{x}) \quad \text{for all } \mathbf{x} \in \mathbb{R}^n \setminus \Omega. \quad (2.8c)$$

It is essential to highlight that the last equation allows to compute the potential  $\phi$  everywhere in the domain  $\mathbb{R}^n \setminus \Omega$  if  $\phi$  is known on the boundary  $\partial\Omega$ .

Moreover, the collocation of equation (2.8c) on points of the domain boundary  $\partial\Omega$  is typically used, in the framework of Boundary Element Methods (BEM) as the base of a discretization algorithm for Laplace problems (2.1a) or (2.2a), which only require the discretization of  $\partial\Omega$ .

To do so we evaluate (2.8c) on the boundary. Taking the limit for  $\mathbf{x}$  tending to  $\partial\Omega$  equation (2.8c) can be reduced to the following expression

$$\alpha(\mathbf{x})\phi(\mathbf{x}) = \phi_\infty - \left( S \left( \frac{\partial\phi}{\partial n} \right) \right) (\mathbf{x}) + (D\phi)(\mathbf{x}) \quad \text{for all } \mathbf{x} \in \partial\Omega, \quad (2.9)$$

known as *boundary integral equation* (BIE), see [19, 9]. The quantity  $\alpha(\mathbf{x})$  is the fraction of angle, in 2D, or of solid angle, in 3D, by which point  $\mathbf{x}$  sees the fluid domain  $\mathbb{R}^n \setminus \Omega$ . The complete expression for S and D are substituted obtaining:

$$\alpha(\mathbf{x})\phi(\mathbf{x}) = \phi_\infty + \frac{1}{2\pi} \int_{\partial\Omega} \ln |\mathbf{x} - \mathbf{y}| \frac{\partial\phi}{\partial n} ds_y + \frac{1}{2\pi} \int_{\partial\Omega} \frac{(\mathbf{x} - \mathbf{y}) \cdot \mathbf{n}_y}{|\mathbf{x} - \mathbf{y}|^2} \phi(\mathbf{y}) ds_y \quad (2.10)$$

and

$$\alpha(\mathbf{x})\phi(\mathbf{x}) = \phi_\infty - \frac{1}{4\pi} \int_{\partial\Omega} \frac{1}{|\mathbf{x} - \mathbf{y}|} \frac{\partial\phi}{\partial n} ds_y + \frac{1}{4\pi} \int_{\partial\Omega} \frac{(\mathbf{x} - \mathbf{y}) \cdot \mathbf{n}_y}{|\mathbf{x} - \mathbf{y}|^3} \phi(\mathbf{y}) ds_y \quad (2.11)$$

for two dimensional and for three dimensional flows, respectively. The quantity  $\alpha(\mathbf{x})$  can also be seen as the coefficient needed to satisfy the BIE if a constant solution, for example  $\phi = \phi_\infty$ , is considered. This kind solution is a solution of the original Laplace problem therefore it must be solution of the Boundary Integral problem,  $\alpha(\mathbf{x})$  can be seen as the quantity that allows for that to be the case. We have the following expression,

$$\alpha(\mathbf{x}) := 1 - \frac{1}{2(n-1)\pi} \int_{\partial\Omega} \frac{(\mathbf{y} - \mathbf{x}) \cdot \mathbf{n}_y}{|\mathbf{y} - \mathbf{x}|^n} ds_y = 1 + \int_{\partial\Omega} \frac{\partial G(\mathbf{y} - \mathbf{x})}{\partial \mathbf{n}_y} ds_y. \quad (2.12)$$

This way to compute the quantity  $\alpha(\mathbf{x})$  is called "rigid mode" method, see Brebbia in [5]. This technique has been tested in [10], and it improves both the conditioning and the accuracy of the solution of the algebraic system resulting from the discretization of (2.9), as assessed by S. Grilli *et al.* [11]. This equation has been used to compute  $\alpha(\mathbf{x})$  in this work. Although in this chapter the formulation both for a two and a three dimensional problems have been reported, in the rest of the present work only the three dimensional case is considered.

We look for a solution of the problem (2.11) in spaces  $V, Q$  defined as

$$V := \left\{ \phi \in H^{\frac{1}{2}}(\Gamma) \right\} \quad (2.13a)$$

$$Q := \left\{ \gamma \in H^{-\frac{1}{2}}(\Gamma) \right\}. \quad (2.13b)$$

We recall that  $H^{\frac{1}{2}}(\Gamma)$  can be defined as the space of traces on  $\Gamma$  of function in  $H^1(\mathbb{R}^n \setminus \Omega)$ . While  $H^{-\frac{1}{2}}(\Gamma)$  is the dual space of  $H^{\frac{1}{2}}(\Gamma)$ .

## 2.3 Discretization procedure and Isoparametric Collocation BEM

A discretization of the Laplace problem based on the BIE obtained in the previous chapter is here discussed. It leads to a linear system whose solution is an approximated solution of the original Laplace problem.

Firstly, as reported by [20], a decomposition  $\Gamma_h$  of the boundary  $\partial\Omega$  made of quadrilateral cells is introduced. The following regularity hypothesis are considered satisfied:

- Any two cells  $K, K'$  only intersects on common faces, edges or vertices

- $\Gamma_D = \bigcup K$  for some  $K \in \Gamma_h$ , the same applies to  $\Gamma_N$ .

One of the most common strategies to solve a boundary integral equation is the collocation boundary element method. In this framework the continuous functions  $\phi, \partial\phi/\partial n$  are replaced by their numerical approximations and then the equation is collocated on a sufficient number of points on  $\Gamma$ . To this end, the following finite dimensional subspaces are defined:

$$V_h := \{ \phi_h \in V : \phi_{h|K} \in \mathbb{P}^r(K), K \in \Gamma_h \} \equiv \text{span}\{\psi_i\}_{i=1}^{N_V} \quad (2.14a)$$

$$Q_h := \{ \gamma_h \in Q : \gamma_{h|K} \in \mathbb{P}^s(K), K \in \Gamma_h \} \equiv \text{span}\{\omega_i\}_{i=1}^{N_Q}, \quad (2.14b)$$

where  $\phi_h$  and  $\gamma_h$  represent the discretized potential and potential normal derivative respectively. On each cell  $K$   $\phi_{h|K}, \gamma_{h|K}$  are polynomial representations of degree  $r$  and  $s$  respectively. The corresponding Lagrangian basis functions of the spaces  $V_h$  and  $Q_h$  are denoted  $\psi_i$  and  $\omega_i$  respectively. In this work, since our aim is to build a monolithic BEM, a vectorial representation of all the degrees of freedom has been used. The finite element approximation is created so that the first component is represented by  $\phi_h$ , while the second component is  $\gamma_h$ .

In addition to these two unknowns even the geometry has to be discretized. In principle, it is possible to choose arbitrary discretizations of the functional spaces  $V_h, Q_h$  once the geometrical representation  $\Gamma_h$  is set. Every element  $K \in \Gamma_h$  is generated from a reference cell  $\hat{K}$ , which is mapped on the real domain through a mapping function. The most natural and common choice is to employ the same discretization used for the geometrical mapping also for the unknowns of the problem. This method is often referred to as Isoparametric Collocation Boundary Element Method. The typical isoparametric BEM implementations employ the same approximation space for the geometrical coordinates  $x, y, z$ , for the potential  $\phi$  and its normal derivative  $\partial\phi/\partial n$ . Generally the elements of such a space are chosen to be continuous.

Nevertheless the domain may present edges (even if the domain is smooth its geometrical approximation has edges), where the normal to the boundary is not continuous, and so is the approximation of  $\partial\phi/\partial n$ . For this reason, the present method is implemented so that a continuous or discontinuous  $Q_h$  space can be selected at the start of each computation, along with the degrees  $r$  and  $s$  of the finite dimensional spaces  $V_h$  and  $Q_h$ .

Thus our method is an Isoparametric Collocation BEM in that the potential  $\phi$  has been discretized using the same approximation method employed for the geometry. As for the potential normal derivative, we will evaluate both continuous and discontinuous approximation strategies thus using a hybrid BEM.

## 2.4 Assembling the algebraic system

In the collocation BEM framework, the linear algebraic system which approximates the original Laplace equation is obtained via discretization of a suitable set of BIEs. The boundary discretization  $\Gamma_h$  of the domain will more frequently be referred to as triangulation. It is assumed regular in the sense explained in the previous paragraph. The unknowns  $\phi$  and  $\partial\phi/\partial n$  are approximated via finite elements, namely

$$\phi_h(\mathbf{x}) = \sum_i \psi_i(\mathbf{x})\phi_i \quad (2.15)$$

$$\frac{\partial\phi}{\partial n_h}(\mathbf{x}) = \sum_i \omega_i(\mathbf{x})\frac{\partial\phi}{\partial n_i}. \quad (2.16)$$

Where  $\{\psi_i\}$  and  $\{\omega_i\}$  are the set of basis functions that have cardinality  $N_\phi = \dim V_h$  and  $N_{\partial\phi/\partial n} = \dim Q_h$ . We have chosen to use Lagrangian basis functions, so that the unknowns  $\phi_i$  and  $\frac{\partial\phi}{\partial n_i}$  are the values of the potential and its normal derivative on the support points. The  $i$ -th basis function has value 1 on the corresponding  $i$ -th degree of freedom and 0 on all the others

$$\psi_i(\mathbf{x}_j) = \delta_{ij} \quad i, j = 1, \dots, N_\phi \quad (2.17a)$$

$$\omega_i(\mathbf{x}_j) = \delta_{ij} \quad i, j = 1, \dots, N_{\partial\phi/\partial n} \quad (2.17b)$$

If  $p = 1$  is chosen, such basis functions are commonly called "hat functions". The degrees of freedom on the reference element  $\hat{K}$  are mapped in the current element  $K$  through a mapping function. The points in the real space which correspond to the degrees of freedom in each cell are called support points. In the framework of the collocation BEM, the BIE must be satisfied on the support points, which are in fact the collocation points of the scheme.

In a typical collocation BEM approach, the following BIE

$$\alpha(\mathbf{x}_i)\phi_h(\mathbf{x}_i) - \int_{\Gamma_y} \frac{\partial G(\mathbf{y} - \mathbf{x}_i)}{\partial \mathbf{n}_y} \phi_h(\mathbf{y}) ds_y - \int_{\Gamma_y} G(\mathbf{y} - \mathbf{x}_i) \frac{\partial\phi}{\partial n_h} ds_y = 0,$$

$\mathbf{x}_i$  being a generic collocation point, is transformed into a single line of the following algebraic system

$$(\mathbf{A} + \mathbf{N})\phi + \mathbf{D}\frac{\partial\phi}{\partial \mathbf{n}} = 0. \quad (2.18)$$

where

$$\begin{aligned}
\mathbf{A}_{ij} &= \alpha(\mathbf{x}_i)\psi_j(\mathbf{x}_i) = 1 + \int_{\Gamma} \frac{\partial G(\mathbf{y} - \mathbf{x}_i)}{\partial \mathbf{n}_y} \psi_j(\mathbf{y}), ds_y \\
\mathbf{N}_{ij} &= - \int_{\Gamma} \frac{\partial G(\mathbf{y} - \mathbf{x}_i)}{\partial \mathbf{n}_y} \psi_j(\mathbf{y}) ds_y \\
\mathbf{D}_{ij} &= - \int_{\Gamma} G(\mathbf{y} - \mathbf{x}_i) \psi_j(\mathbf{y}) ds_y \\
\boldsymbol{\phi} &= \{\phi_1, \dots, \phi_{N_\phi}\} \\
\frac{\partial \boldsymbol{\phi}}{\partial \mathbf{n}} &= \left\{ \frac{\partial \phi}{\partial n_1}, \dots, \frac{\partial \phi}{\partial n_{N_{\partial \phi / \partial n}}} \right\}
\end{aligned}$$

If a Neumann problem is considered, the normal derivative is known so the system can be rewritten as follows

$$(\mathbf{A} + \mathbf{N})\boldsymbol{\phi} = -\mathbf{D} \frac{\overline{\partial \boldsymbol{\phi}}}{\partial \mathbf{n}} = \mathbf{b}, \quad (2.19)$$

where the  $i$ -th element of vector  $\frac{\partial \boldsymbol{\phi}}{\partial \mathbf{n}}$  is  $\frac{\overline{\partial \phi}}{\partial n_i} = h(\mathbf{x}_i)$ . In case of Dirichlet problem instead, the value of  $\boldsymbol{\phi}$  is known so the system is rewritten as follows

$$\mathbf{D} \frac{\partial \boldsymbol{\phi}}{\partial \mathbf{n}} = -(\mathbf{A} + \mathbf{N})\overline{\boldsymbol{\phi}} = \mathbf{c}, \quad (2.20)$$

where the  $i$ -th element of  $\boldsymbol{\phi}$  is  $\overline{\phi}_i = g(\mathbf{x}_i)$ .

When the more general case, with mixed boundary condition, is considered, a typical approach is, see [19],

$$\boldsymbol{\phi} = \overline{\boldsymbol{\phi}}_D + \boldsymbol{\phi}_N \quad \frac{\partial \boldsymbol{\phi}}{\partial \mathbf{n}} = \frac{\partial \boldsymbol{\phi}}{\partial \mathbf{n}_D} + \frac{\overline{\partial \boldsymbol{\phi}}}{\partial \mathbf{n}_N},$$

where

$$\overline{\phi}_{iD} = \begin{cases} \overline{\phi}_i & \mathbf{x}_i \in \Gamma_D \\ 0 & \mathbf{x}_i \in \Gamma_N \end{cases} \quad \phi_{iN} = \begin{cases} 0 & \mathbf{x}_i \in \Gamma_D \\ \phi_i & \mathbf{x}_i \in \Gamma_N \end{cases} \quad (2.21a)$$

and

$$\frac{\partial \boldsymbol{\phi}}{\partial \mathbf{n}_{iD}} = \begin{cases} \frac{\partial \phi}{\partial n_i} & \mathbf{x}_i \in \Gamma_D \\ 0 & \mathbf{x}_i \in \Gamma_N \end{cases} \quad \frac{\overline{\partial \boldsymbol{\phi}}}{\partial \mathbf{n}_{iN}} = \begin{cases} 0 & \mathbf{x}_i \in \Gamma_D \\ \frac{\overline{\partial \phi}}{\partial n_i} & \mathbf{x}_i \in \Gamma_N. \end{cases} \quad (2.21b)$$

As seen before, the overlined symbol indicates known values, prescribed by imposing the boundary conditions. The final form of the linear problem to be solved reads

$$(\mathbf{A} + \mathbf{N})\phi_N - \mathbf{D}\frac{\partial\phi}{\partial\mathbf{n}_D} = \mathbf{D}\frac{\overline{\partial\phi}}{\partial\mathbf{n}_N} - (\mathbf{A} + \mathbf{N})\overline{\phi}_D, \quad (2.22)$$

which can be recast in the more familiar form

$$\mathbf{M}\mathbf{u} = \mathbf{b} \quad (2.23)$$

where

$$\mathbf{u} = \phi_N + \frac{\partial\phi}{\partial\mathbf{n}_D}, \quad \mathbf{b} = \mathbf{D}\frac{\overline{\partial\phi}}{\partial\mathbf{n}_N} - (\mathbf{A} + \mathbf{N})\overline{\phi}_D,$$

and where  $\mathbf{M}$  is defined by

$$M_{ij} = \begin{cases} \alpha_j\delta_{ij} + N_{ij} & \mathbf{x}_j \in \Gamma_N \\ D_{ij} & \mathbf{x}_j \in \Gamma_D. \end{cases}$$

However, in the present work we follow a different strategy. We want to study an hybrid method which approximates the potential and its normal derivative differently, on different collocation points, so it is easier to treat the problem with a monolithic BEM. It is clear that our monolithic BEM is based on a system of  $N_\phi + N_{\partial\phi/\partial n}$  equations in  $N_\phi + N_{\partial\phi/\partial n}$  unknowns which is equivalent to system (2.22).

To do so we consider 2 different scalar unknowns that will be determined by the solution of the system, namely the potential  $\phi$  and the potential normal derivative  $\partial\phi/\partial n$ . As the space for the discrete potential normal derivative is discontinuous across elements, it is necessary to treat these components differently. This is achieved by creating a multicomponent finite element, in which continuous or discontinuous basis functions can be selected for each component. Such multicomponent approach will result in a block system. The main difference from the classical approach is that at every collocation point the BEM is written considering both  $\phi$  and  $\partial\phi/\partial n$  as unknowns. Thus all the collocation points are related to an unknown, and the algebraic system line is obtained through the discretization of a BIE.

For what concerns the lines of the algebraic system coming from the discretization of the BIE, all integrations are performed on a planar reference domain, i.e. we assume that each element  $K_i$  of  $\Gamma_h$  has a transformation of the reference boundary element  $\hat{K} := [0, 1]^{n-1}$

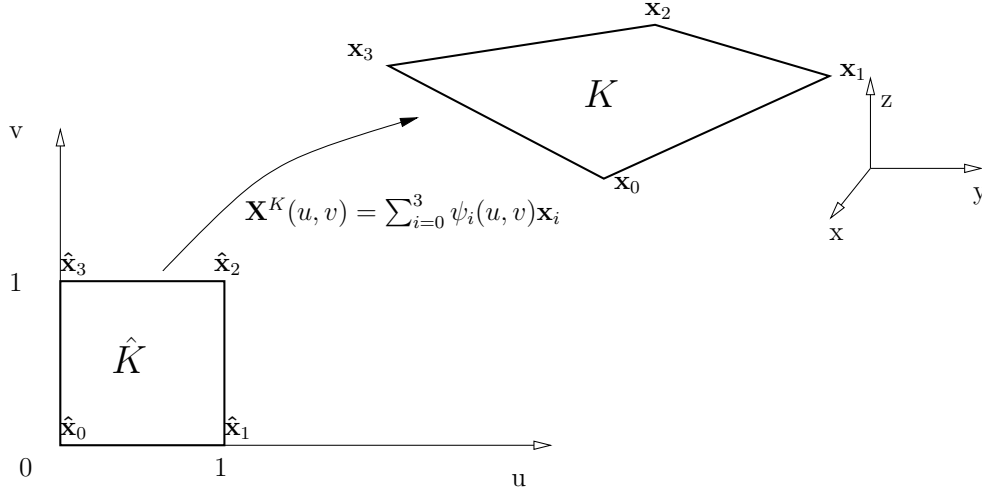


**Figure 2.1:** Transformation from reference to real cell. In this example we have considered a linear continuous approximation for the geometry. The BEM is isoparametric because the geometry is described by the same finite element approximation of the potential  $\phi$

The integrations can be performed after a change of variables from the real element  $K_i$  to the reference element  $\hat{K}$ .

For every collocation point  $\mathbf{P}$  we obtain the following line of the BEM system,

$$\alpha(\mathbf{P})\phi(\mathbf{P}) + \sum_{k=1}^M \sum_{i=1}^n \phi_i \int_0^1 \int_0^1 \frac{\partial G}{\partial n}(\mathbf{X}^K(u, v), \mathbf{P}) \psi_i(u, v) J^{X^K}(u, v) dudv - \sum_{k=1}^M \sum_{j=1}^m \left( \frac{\partial \phi}{\partial n} \right)_j \int_0^1 \int_0^1 G(\mathbf{X}^K(u, v), \mathbf{P}) \omega_j(u, v) J^{X^K}(u, v) dudv = 0,$$

where  $M$  is the number of cells,  $n$  the number of  $\phi$  degrees of freedom on a cell,  $m$  the number of  $\partial\phi/\partial n$  degrees of freedom on a cell and  $\mathbf{X}$  is the point on the cell where the current integration is performed. The operation is repeated for every collocation points to recover the typical matrix formulation of a BEM

$$(\mathbf{A} + \mathbf{N})\phi + \mathbf{D} \frac{\partial \phi}{\partial \mathbf{n}} = 0.$$

This formulation can be reordered so as to compose a single vectorial unknown in order to have the typical linear algebraic formulation  $\mathbf{M}\mathbf{u} = \mathbf{b}$ . The entire BEM algebraic matrix is a block matrix of the form

$$\begin{bmatrix} [\mathbf{NN}] & [\mathbf{ND}] \\ [\mathbf{DN}] & [\mathbf{DD}] \end{bmatrix} \begin{Bmatrix} \phi_i \\ \frac{\partial \phi}{\partial n_j} \end{Bmatrix} = \begin{Bmatrix} 0 \\ 0 \end{Bmatrix}. \quad (2.24)$$

To obtain the first block line it is sufficient to collocate the boundary integral equation on the  $N_\phi$  support points corresponding to the potential degrees of freedom. The other block line is obtained using the  $N_{\partial\phi/\partial n}$  support points of the normal derivative as collocation points. So if  $\mathbf{P}_i$  is a  $\phi$  collocation point we write

$$NN_{ij} = \alpha(\mathbf{P}_i) + \sum_{k=1}^M \sum_{i=1}^n \int_0^1 \int_0^1 \frac{\partial G}{\partial n}(\mathbf{X}^K(u, v), \mathbf{P}_i) \psi_j(u, v) J^{X^K}(u, v) dudv, \quad (2.25a)$$

$$ND_{ij} = \sum_{k=1}^M \sum_{j=1}^m \left( \frac{\partial \phi}{\partial n} \right)_j \int_0^1 \int_0^1 G(\mathbf{X}(u, v), \mathbf{P}) \omega_j(u, v) J^{X^K}(u, v) dudv = 0, \quad (2.25b)$$

and if  $\mathbf{P}_i$  is a  $\frac{\partial\phi}{\partial n}$  collocation point

$$DN_{ij} = \alpha(\mathbf{P}_i) + \sum_{k=1}^M \sum_{i=1}^n \int_0^1 \int_0^1 \frac{\partial G}{\partial n}(\mathbf{X}^K(u, v), \mathbf{P}_i) \psi_j(u, v) J^{X^K}(u, v) dudv, \quad (2.26a)$$

$$DD_{ij} = \sum_{k=1}^M \sum_{j=1}^m \left( \frac{\partial \phi}{\partial n} \right)_j \int_0^1 \int_0^1 G(\mathbf{X}(u, v), \mathbf{P}) \omega_j(u, v) J^{X^K}(u, v) dudv = 0. \quad (2.26b)$$

Such matrix system would be singular since no boundary condition has been imposed yet. So, in Dirichlet regions the matrix lines corresponding to potential degrees of freedom, are substituted with 1 on the principal diagonal, and the exact value of  $\phi$  in the right hand side line; on Neumann boundaries the matrix lines corresponding to the potential normal derivative degrees of freedom, are substituted with a 1 on the principal diagonal, and the exact  $\partial\phi/\partial n$  values as right hand side

$$\phi_i = g(\mathbf{x}_i) \quad \text{on } \Gamma_D \quad (2.27)$$

$$\frac{\partial \phi}{\partial n_j} = h(\mathbf{x}_j) \quad \text{on } \Gamma_N. \quad (2.28)$$

Using this technique a nonsingular system is obtained. To explain better the process used in this work, we consider Figures 2.2 and 2.3, they report two examples of such matrix assembling. For the sake of simplicity we consider a linear continuous approximation for  $\phi$  and a piecewise constant one for  $\partial\phi/\partial n$ . In the example a single cell has been considered. The figures only show the reference cell, but it is important to remind that all the calculations have to be performed on the real triangulation, as shown in Figure 2.1



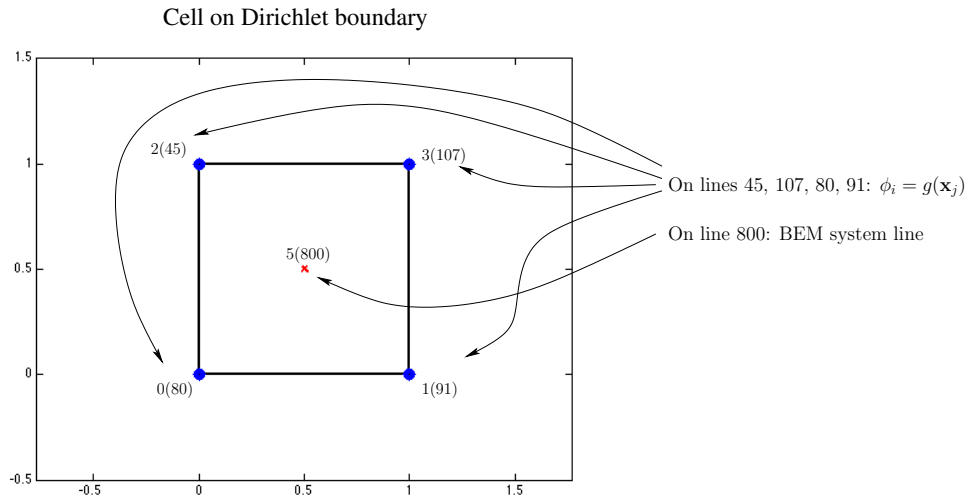


**Figure 2.2:** Blue dots represent the  $\phi$  degrees of freedom. Red crosses indicate instead the  $\partial\phi/\partial n$  degrees of freedom. The global degree of freedom numeration for this degree is reported between brackets. The imposition of boundary values, along with collocation of BIEs on the  $\partial\phi/\partial n$  degrees of freedom, is used to assemble the proper blocks in equation (2.29)

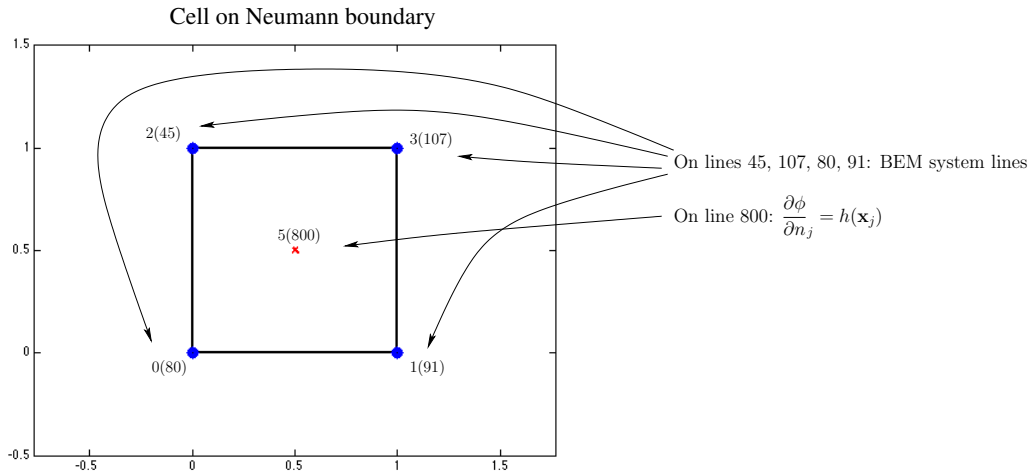


**Figure 2.3:** Blue dots represent the  $\phi$  degrees of freedom. Red crosses indicate instead the  $\partial\phi/\partial n$  degrees of freedom. The global degree of freedom numeration for this degree is reported between brackets. The imposition of boundary values, along with collocation of BIEs on the  $\phi$  degrees of freedom, is used to assemble the proper blocks in equation (2.29)

Using the previous modifications to system (2.24) it is possible to rewrite the complete BEM system as

$$\begin{bmatrix} [\overline{\mathbf{NN}}] & [\overline{\mathbf{ND}}] \\ [\overline{\mathbf{DN}}] & [\overline{\mathbf{DD}}] \end{bmatrix} \begin{Bmatrix} \phi_i \\ \frac{\partial \phi}{\partial n_j} \end{Bmatrix} = \begin{Bmatrix} \mathbf{b} \end{Bmatrix}, \quad (2.29)$$

where,

$$\overline{NN}_{ij} = \begin{cases} NN_{ij} & \text{if } \mathbf{x}_i \notin \Gamma_D \\ \delta_{ij} & \text{if } \mathbf{x}_i \in \Gamma_D \end{cases} \quad \overline{ND}_{ij} = \begin{cases} ND_{ij} & \text{if } \mathbf{x}_i \notin \Gamma_D \\ 0 & \text{if } \mathbf{x}_i \in \Gamma_D \end{cases} \quad (2.30a)$$

$$\overline{DN}_{ij} = \begin{cases} DN_{ij} & \text{if } \mathbf{x}_i \notin \Gamma_N \\ 0 & \text{if } \mathbf{x}_i \in \Gamma_N \end{cases} \quad \overline{DD}_{ij} = \begin{cases} DD_{ij} & \text{if } \mathbf{x}_i \notin \Gamma_N \\ \delta_{ij} & \text{if } \mathbf{x}_i \in \Gamma_N \end{cases} \quad (2.30b)$$

$$b_i = \begin{cases} 0 & \text{if } \mathbf{x}_i \notin \Gamma_D \text{ and } \mathbf{x}_i \text{ is a } \phi \text{ support point} \\ \overline{\phi}_i & \text{if } \mathbf{x}_i \in \Gamma_D \text{ and } \mathbf{x}_i \text{ is a } \phi \text{ support point} \\ 0 & \text{if } \mathbf{x}_i \notin \Gamma_N \text{ and } \mathbf{x}_i \text{ is a } \frac{\partial \phi}{\partial n} \text{ support point} \\ \overline{\frac{\partial \phi}{\partial n_i}} & \text{if } \mathbf{x}_i \in \Gamma_N \text{ and } \mathbf{x}_i \text{ is a } \frac{\partial \phi}{\partial n} \text{ support point} \end{cases} \quad (2.30c)$$

This is a well posed algebraic linear system. Since the boundary conditions have been imposed system (2.29) is different from (2.24).

From a linear algebra point of view, the best possible choice of the collocation points is the one that is able to make the first submatrix of the BEM system  $[\overline{\mathbf{NN}}]$  as diagonally dominant as possible. It is important to highlight that this submatrix, in the lines where the BIE equations have been imposed, comes from  $[\mathbf{A} + \mathbf{N}]$  in (2.4). On the Neumann boundaries the choice is then to select the collocation points to be the support points of the potential. As a consequence of (2.17a), the matrix  $\mathbf{A}$  is diagonal with entries,

$$A_{ii} = 1 - \sum_j \overline{NN}_{ij}$$

where we used the property  $\sum_j \psi_j(\mathbf{y}) = 1$ .

Another similar operation is performed for the second block line of the BEM block subsystem. The submatrix  $[\overline{\mathbf{DN}}]$  still comes from  $[\mathbf{A} + \mathbf{N}]$  in (2.4). Since here we collocate the BIEs at the support points for the potential normal derivative finite element approximation also in this case  $\alpha$  is computed adding the elements of each line of  $[\overline{\mathbf{DN}}]$ . All the consideration done for the first subpart can be repeated here with a very important exception. We have to recall that the quantity  $\alpha(\mathbf{x}_i) = A_{ii}$  is the solid angle computed on the collocation point, so on  $\mathbf{x}_i$  which is now a

support point for the normal derivative. In the BIE, the value of  $\alpha$  multiplies the potential on the support point, namely

$$\alpha(\mathbf{x}_i)\phi(\mathbf{x}_i) = \alpha(\mathbf{x}_i) \sum_{j=1}^n \psi_j(\mathbf{x}_i)\phi_j, \quad (2.31)$$

where  $\psi_j(\mathbf{x}_i)$  is one of the  $n$  basis functions of the potential evaluated at  $\mathbf{x}_i$  on the cell where the points  $\mathbf{x}_i$  is located. So to every element of the matrix  $\overline{\mathbf{DN}}$  in the  $i$ -th line we must add the quantity  $\alpha(\mathbf{x}_i)\psi_j(\mathbf{x}_i)$  in order to consider the solid angle properly.

Once the  $\alpha$  contribution is correctly considered in the submatrix  $\overline{\mathbf{DN}}$  the BEM system for the Laplace equation is completely assembled.

In Figures 2.2 and 2.3 we can see that our method can treat different approximations, which mean different collocation points, for the potential  $\phi$  and its normal derivative  $\partial\phi/\partial n$ ; for this reason it is called hybrid BEM. A typical approach provides instead the same linear continuous approximation for both the unknowns.

We want to stress that Figures 2.2 and 2.2 are only two examples of the technique used to assemble the monolithic BEM. In Chapter 3 of the present work different approximations of the unknown will be presented and discussed.

In case of a first order analysis the potential  $\phi$  is always approximated through linear continuous linear elements while the normal derivative  $\partial\phi/\partial n$  through continuous linear elements (to create the continuous reference BEM), linear discontinuous elements and piecewise constant elements. When a second order analysis is performed the potential  $\phi$  is always approximated through quadratic continuous linear elements while the normal derivative  $\partial\phi/\partial n$  through quadratic continuous elements (to create the continuous reference BEM), quadratic discontinuous elements, linear discontinuous elements and piecewise constant elements.



# Chapter 3

## Preliminary validation

Firstly we want to explain the terms we use in this section. The BEM method we present in the present work is called hybrid because we have the possibility of choosing different finite element approximations for the two unknowns. In particular we always maintain a continuous approximation for the potential  $\phi$  but we can choose a discontinuous approximation for its normal derivative  $\partial\phi/\partial n$ . The typical BEM approach provides the same continuous approximation for the two unknowns, we call this approach reference BEM.

The aim of this section is to verify the behavior of the formulation of the Boundary Element Method implemented through some significant cases.

The first one is the same problem tackled by L. Heltai, C. Manigrasso, A. De Simone, in the example step 34 of the library `deal.II` [9, 14] and by A. Mola in [19]. Such problem is the irrotational flow past a sphere moving in an inviscid fluid at constant speed. For this interesting problem also a second order analysis has been performed to show how the developed method can treat higher order boundary elements. Nevertheless this case is not suited to show all the peculiarities of the present method. A sphere is in fact a very peculiar domain since it is completely isotropic. Therefore the only meaningful refinement strategy is a classical global refinement one. To present an example of how the present method deals with this local refinement the analytical potential, as reported in [16], around a spheroid has been considered. The spheroid isn't isotropic as the sphere therefore a local refinement strategy may be applied as will be explained in the following chapters. This test case is able to confirm the convergence results of the sphere. Moreover it would allow for better estimation of convergence order, as the peculiar symmetry of the sphere, together with the simplicity of the first test case, may cause a superconvergence for the method. The last of these cases aims to assess a very important feature of the present method, which is the ability of treating an edge naturally without needing any additional treatment. A continuous approximation, as presented in [20], needs the implementation of double nodes, [12], around edges

to recover the discontinuity in the normal vector. Our hybrid method should be able to treat this discontinuity naturally. A comparison between one hybrid approximation and the classical continuous one is performed.

### 3.1 Test Problem 1: Sphere

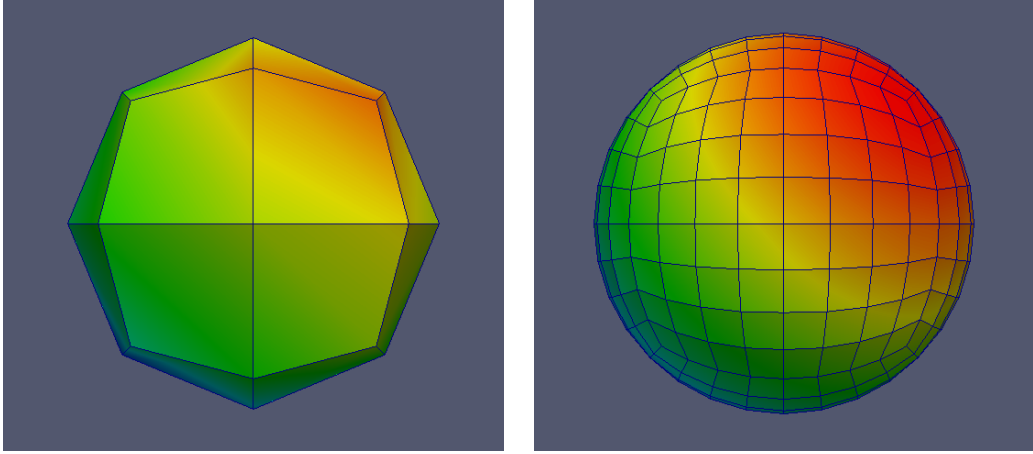


**Figure 3.1:** On the left, the mesh refined only once. On the right, the final mesh, after three uniform refinement cycles

The domain of the problem is a sphere of radius  $R = 1$ , the analytical potential and potential normal derivative are known. The surface where the Laplace equation is studied is a sphere centered in the origin with radius  $R = 1$ . The exact potential solution is

$$\phi(r, \theta) = \frac{2\sqrt{3}R^3}{2r^3} \cos \theta \quad (3.1)$$

Where  $\theta$  is the angle between the direction  $(1, 1, 1)$  and the position on the sphere, and  $r$  is the distance of the point from the center of the sphere, the origin in this case. The exact expression for  $\phi$  is written on the sphere and it is simplified in equation (3.2)

$$\phi(x, y, z) = \frac{2\sqrt{3}}{2R^3} \frac{(x + y + z)}{\sqrt{3}} = x + y + z. \quad (3.2)$$

The exact normal derivative to be imposed is

$$\frac{\partial \phi}{\partial n} = 2(x + y + z). \quad (3.3)$$

These two functions can be used to impose the boundary conditions on the sphere surface. Since mixed boundary conditions are wanted it is chosen to impose a Dirichlet condition if  $y < 0$  and a Neumann condition if  $y \geq 0$ . In this way is possible to evaluate the convergence of both the potential and its normal derivative. In order to show the possibility of the present method to use also non linear boundary element approximation for this first case a convergence analysis has been performed also for quadratic elements. This potential represents the perturbation potential due to sphere in the presence of an external flow  $(2, 2, 2)$  as it can be seen in [22] pag.127.

### 3.1.1 Convergence Analysis

The purpose is to study the convergence of our hybrid method, characterized by a continuous approximation for  $\phi$  and a discontinuous one for  $\partial\phi/\partial n$ . The results are compared to equivalent solutions obtained using a continuous approximation both for the potential and its normal derivative. As explained in the previous chapters, an isoparametric BEM is employed. If the solution  $\phi$  is approximated linearly a linear mapping function is used, while if  $\phi$  is approximated with a second order, the same order is used for the mapping degree. At every refinement cycle, every quadrilateral cell is divided into four new ones.

For this test case an analysis of the position of the discontinuous collocation points in each cell is also carried out. The purpose is to study how the position of the collocation points influences the solution. Successively two convergence analyses are performed for linear and quadratic elements, in order to characterize how the degree of the approximations affects the solution.

The errors in all the convergence analyses of the present work are evaluated through the  $L_2$  norm, defined as

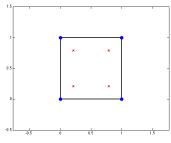
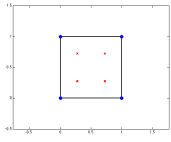
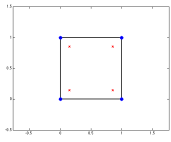
$$e_{L_2}^{u_h} = \frac{\int_{\Gamma} (u_h - u_{exact})^2 d\gamma}{\int_{\Gamma} u_{exact}^2 d\gamma} \quad (3.4)$$

### 3.1.2 Influence of the collocation points position in the hybrid method

The position of the degrees of freedom of the discontinuous approximation, which are the collocation points of the discontinuous approximation to use in the BEM, has been chosen according to Sriganesh and Ramachandran [15]. They suggested to find the collocation points, in one dimensional elements, finding the roots of the Rodrigues' formula, namely

$$(1-x)^\alpha x^\beta P_n^{(\alpha,\beta)}(x) = (-1)^n \frac{\Gamma(\beta+1)}{\Gamma(n+\beta+1)} \frac{d^n}{dx^n} [(1-x)^{n+\alpha} x^{n+\beta}]. \quad (3.5)$$

Where  $\Gamma$  is the Gamma function. To have a discontinuous element of degree  $p$ , it is necessary to solve the Rodrigues' formula with  $n = p+1$ . Such roots are found in the the interval  $[0, 1]$ . This one dimensional procedure has been here extended to 2D cells via tensor product of 1D collocation points. In this section a short analysis of the influence of parameters  $\alpha, \beta$  is performed in order to choose a valid couple of coefficients for the rest of the present work. Negative values mean that the points are nearer to the boundary of the cells and positive that the points are clustered near the cell center. If  $\alpha$  and  $\beta$  are chosen equal to 0 the collocation points are the Gauss quadrature nodes. A linear continuous approximation is chosen for the potential, while a discontinuous linear one is employed for its normal derivative. Table 3.1 shows the influence of  $\alpha$ , and  $\beta$  on the position of the collocation points for the linear discontinuous approximation.

Label	Collocation points	$\alpha$	$\beta$
LinLin0		0	0
LinLin1		1	1
LinLin-0.5		-0.5	-0.5

**Table 3.1:** Scheme of the 2D reference cell employed. Blue dots depict the collocation point of the linear continuous approximation. Red crosses indicate collocation points for the discontinuous approximation

To evaluate if the values of  $\alpha$ , and  $\beta$  affect the convergence properties of the solution three refinement steps are here performed. The resulting meshes are depicted in Figure 3.1 Figure 3.2 shows the convergence results for  $\phi$ , Figure 3.3 shows the convergence results for  $\partial\phi/\partial n$  for each of the three hybrid approximations in the sphere case test reported in Table 3.1.



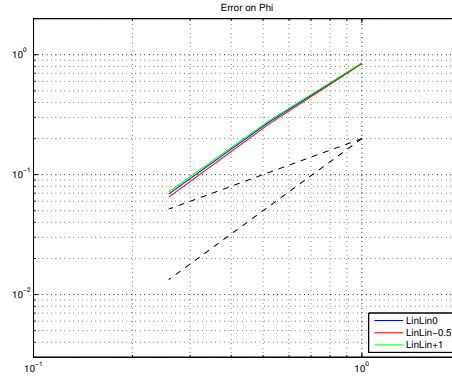


**Figure 3.2:** The blue line represents the  $L_2$  error of  $\phi$  for the reference case  $\alpha = \beta = 0$ . The red line refers to the results with  $\alpha = \beta = -0.5$  and the green one to  $\alpha = \beta = 1$ . For convergence sake the black dotted lines show reference slopes of linear and quadratic convergence

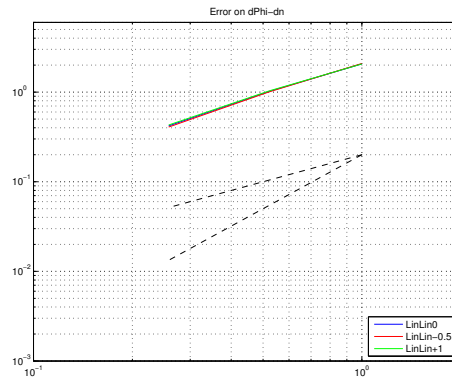


**Figure 3.3:** The blue line represents the  $L_2$  error of  $\partial\phi/\partial n$  for the reference case  $\alpha = \beta = 0$ . The red line refers to the results with  $\alpha = \beta = -0.5$  and the green one to  $\alpha = \beta = 1$ . For convergence sake the black dotted lines show reference slopes of linear and quadratic convergence

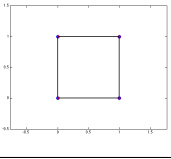
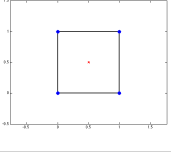
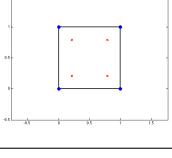
The plots of Figure 3.2 and 3.3 show a very small sensitivity of the convergence rate to the location of the discontinuous collocation points. Both for the potential and its normal derivative, the curves almost overlap. For this reason in the following investigations a 0 value has been chosen both for  $\alpha$  and  $\beta$ , as in such case the collocation points coincide with the Gauss quadrature points, which are readily available in any finite element library. In the original work Sriganesh and Ramachandran suggest that improvements may derive by using of unbalanced

hybrid points near an edge or a boundary. Since one of the purposes of the present work is to avoid any particular treatment at the edges any unbalanced choice of  $\alpha$  and  $\beta$  has been avoided.

### 3.1.3 First order elements

Two hybrid BEM formulations are considered in this section. While the potential is in both cases represented by a continuous linear approximation, its derivative is represented in a first case by a piecewise constant approximation, and in a second case by a discontinuous linear approximation. The degrees of freedom of the discontinuous linear approximation are the Gauss quadrature points, given the choice  $\alpha, \beta = 0$ . The hybrid methods are compared with the reference case, which employs linear continuous approximations both for the potential and its normal derivative.

The tested approximations are labeled as depicted in Table 3.2

Label	Collocation points	Coarse	Medium	Refined
Cont		52 dofs	196 dofs	772 dofs
Lin-Const		50 dofs	194 dofs	770 dofs
LinLin		122 dofs	482 dofs	1922 dofs

**Table 3.2:** Scheme of the 2D reference cell employed. Blue dots depict the collocation points of the linear continuous approximation, used for  $\phi$  in all three methods. Red crosses indicate the collocation points for the discontinuous approximation of  $\partial\phi/\partial n$  used in the hybrid method. Coarse, Medium, and refined indicate the degrees of freedom employed by a single BEM at every refinement step.

The results of the analysis are reported in the following plots. The  $L_2$  norm of the error of  $\phi$  is presented in Figure 3.4. In this convergence analysis 5 global refinement cycles have been carried out.

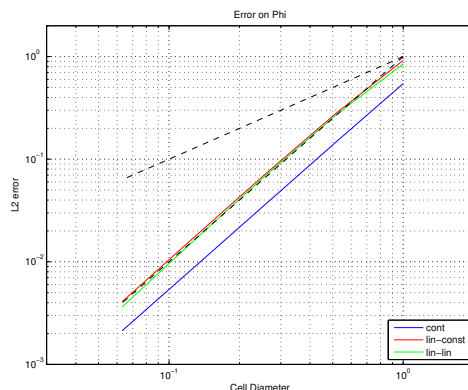


**Figure 3.4:** The blue line represents the  $L_2$  error of  $\phi$  for the reference case, which employs continuous linear elements both for  $\phi$ , and  $\partial\phi/\partial n$ . The red line refers to the results of the hybrid BEM with continuous element for  $\phi$ , and piecewise constant elements for  $\partial\phi/\partial n$ . The green line is the hybrid BEM error obtained with continuous linear elements for  $\phi$ , and discontinuous linear elements for  $\partial\phi/\partial n$ . The black dotted lines show reference slopes per linear and quadratic convergence

While the reference case still has the lower error something very interesting can be noticed. The three methods have the same second order convergence. More importantly the error of the piecewise constant hybrid method and linear discontinuous hybrid method almost overlap. So adopting linear discontinuous elements for  $\partial\phi/\partial n$  results in additional degrees of freedom of the linear problem, with consequent increase of the computational cost. But it does not lead to smaller error, making this strategy less efficient than piecewise constant  $\partial\phi/\partial n$  approximation.

In Figure 3.5 of this section, the  $L_2$  norm of the error of  $\partial\phi/\partial n$  is presented

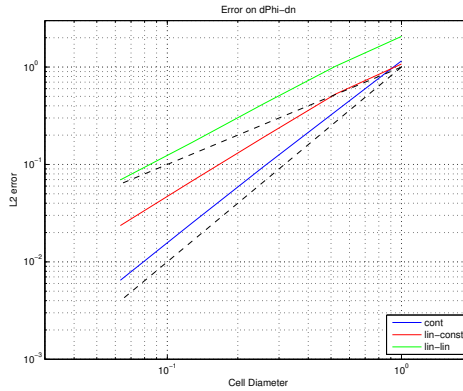


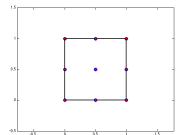
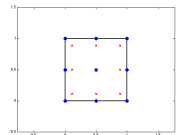
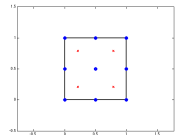
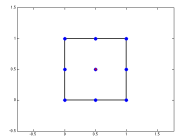
**Figure 3.5:** The blue line represents the  $L_2$  error of  $\partial\phi/\partial n$  for the reference case, which employs continuous linear elements both for  $\phi$ , and  $\partial\phi/\partial n$ . The red line refers to the results of the hybrid BEM with continuous element for  $\phi$ , and piecewise constant elements for  $\partial\phi/\partial n$ . The green line is the hybrid BEM error obtained with continuous linear elements for  $\phi$ , and discontinuous linear elements for  $\partial\phi/\partial n$ . The black dotted lines show reference slopes per linear and quadratic convergence

The continuous linear element is still the best also for the normal derivative of the potential. Remarkably, the piecewise constant approximation reaches better results than the linear discontinuous approximation. They both almost show a second order convergence, but the first one has lower values of the error and lower computational cost.

In conclusion the linear continuous case seems the best choice in terms of accuracy but the piecewise constant hybrid method appears to be better than the linear discontinuous one and could represent a viable compromise between accuracy and computational cost. In the following convergence analyses three global refinement cycles will be carry out in order to value the convergence rate especially. With 5 global refinement cycles the computational cost are very high, so in the following only 3 cycles will be performed.

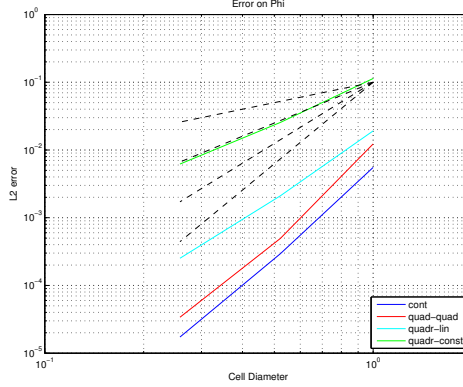
### 3.1.4 Second order elements

Three hybrid methods are here compared. While for  $\phi$  a second order continuous approximation is always chosen, for its normal derivative is represented by a discontinuous quadratic approximation, a linear discontinuous approximation and by a piecewise constant approximation respectively. The reference case is characterized by quadratic continuous representation both for  $\phi$  and  $\partial\phi/\partial n$ . The degree of the mapping has been set equal to 2 to maintain an isoparametric BEM. Three global refinement have also in this case been performed to produce the convergence analysis. The tested approximations are labeled as depicted in Table 3.3

Label	Collocation points	Coarse	Medium	Refined
Cont		196 dofs	772 dofs	3076 dofs
Quad-Quad		314 dofs	1250 dofs	4994 dofs
Quad-Lin		194 dofs	770 dofs	3074 dofs
Quad-Const		122 dofs	482 dofs	1742 dofs

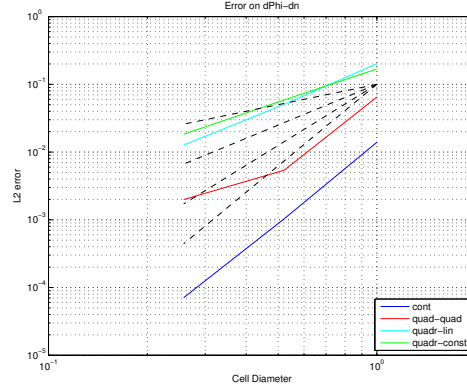
**Table 3.3:** Scheme of the 2D reference cell employed. Blue dots depict the collocation points of the linear continuous approximation, used for  $\phi$  in all three methods. Red crosses indicate the collocation points for the discontinuous approximation of  $\partial\phi/\partial n$  used in the hybrid method. Coarse, Medium, and refined indicate the degrees of freedom employed by a single BEM at every refinement step.

Figure 3.6 presents the  $L_2$  norm of the error of the computed potential  $\phi$ .



**Figure 3.6:** The blue line represents the  $L_2$  error of  $\phi$  for the reference case, which employs continuous quadratic elements both for  $\phi$ , and  $\partial\phi/\partial n$ . The red line refers to the results of the hybrid BEM with continuous quadratic element for  $\phi$ , and quadratic discontinuous elements for  $\partial\phi/\partial n$ . The cyan line is the hybrid BEM error obtained with continuous quadratic elements for  $\phi$ , and discontinuous linear constant elements for  $\partial\phi/\partial n$ . The green line is the hybrid BEM error obtained with continuous quadratic elements for  $\phi$ , and discontinuous piecewise constant elements for  $\partial\phi/\partial n$ . The black dotted lines show reference slopes per first, second, third and fourth order of convergence.

The reference method with continuous quadratic discretization for both  $\phi$  and  $\partial\phi/\partial n$  is showing a convergence order which approaches 4. The hybrid method with continuous quadratic elements for  $\phi$  and quadratic discontinuous elements for  $\partial\phi/\partial n$  is also showing nearly fourth order convergence. The hybrid BEM in which linear discontinuous elements are used for  $\partial\phi/\partial n$  converges almost third order, while employing piecewise constant elements leads to second order convergence. As mentioned, it is important to remember that the quadratic discontinuous approximation has the greater number of degrees of freedom, as shown in Table 3.3. The reference case and the linear approximation almost have the same number of unknowns, while the piecewise constant has the lowest computational cost. Figure 3.7 presents the  $L_2$  norm of the error for the potential normal derivative  $\partial\phi/\partial n$ .



**Figure 3.7:** The blue line represents the  $L_2$  error of  $\partial\phi/\partial n$  for the reference case, which employs continuous quadratic elements both for  $\phi$ , and  $\partial\phi/\partial n$ . The red line refers to the results of the hybrid BEM with continuous quadratic element for  $\phi$ , and quadratic discontinuous elements for  $\partial\phi/\partial n$ . The cyan line is the hybrid BEM error obtained with continuous quadratic elements for  $\phi$ , and discontinuous linear constant elements for  $\partial\phi/\partial n$ . The green line is the hybrid BEM error obtained with continuous quadratic elements for  $\phi$ , and discontinuous piecewise constant elements for  $\partial\phi/\partial n$ . The black dotted lines show reference slopes per first, second, third and fourth order of convergence.

As shown for  $\partial\phi/\partial n$  in Figure 3.7 the reference case still has the highest order of convergence, almost four. The quadratic hybrid method with discontinuous  $\partial\phi/\partial n$  elements presents the same behavior in the initial refinement, but settles for lower convergence rate in the last refinement step. The hybrid BEM with linear  $\partial\phi/\partial n$  approximation has a slightly higher order with respect to the piecewise constant case. Both these approximation strategies for  $\partial\phi/\partial n$  converge at rates between 2 and 3.

In this test case the best choice seems to be the continuous approximation for both  $\phi$  and  $\partial\phi/\partial n$  which has a fourth order convergence. The linear discontinuous approximation for  $\partial\phi/\partial n$  has almost the same number of degrees of freedom, but lower order of convergence than the reference case. The piecewise constant  $\partial\phi/\partial n$  approximation is not an efficient strategy, as the better convergence ensured by the quadratic potential approximation is lost. The quadratic discontinuous  $\partial\phi/\partial n$  approximation has a very high computational cost and also presents some problems in the normal derivative convergence. These kinds of problems may be due to the numeric integration of the kernels. For this reason new quadrature formula are under developing at the moment.

It is worth to remark here that there is the possibility that this fourth order convergence order is due to the isotropy of the sphere combined with the simplicity of the solution. For this reason other analyses will be performed in a non isotropic test case.

We will first present an alternative way to impose Neumann boundary condition.

### 3.1.5 Alternative implementation of Neumann condition

In many applications, when imposing a Neumann boundary condition, the field  $\partial\phi/\partial n$  is not directly available on the boundary collocation points. This is because the normal on such nodes is not uniquely defined, and only  $\nabla\phi$  is available. This is for instance the case when modeling the flow past a body. Here the velocity potential is often split into the far field potential  $\phi_\infty$  and perturbation potential  $\phi$ , namely

$$\mathbf{V} = \nabla\Phi = \nabla(\phi_\infty + \phi). \quad (3.6)$$

Where

$$\mathbf{V}_\infty = \nabla\phi_\infty. \quad (3.7)$$

If non penetration boundary condition are imposed on the body we have

$$\mathbf{V} \cdot \mathbf{n} = \nabla(\phi_\infty + \phi) \cdot \mathbf{n} = 0 \Rightarrow \frac{\partial\phi}{\partial n} = -\mathbf{V}_\infty \cdot \mathbf{n} \quad (3.8)$$

We present a method to impose such a Neumann boundary condition that may be interpreted as a weak imposition. As said, this is very meaningful because the normal, in most cases, is not known *a priori* at the collocation point. If a collocation point is on the edge of the cell in fact, there isn't uniqueness of the the normal, which is instead continuous on the quadrature points. Using the proposed technique, it is possible to obtain a weak solution which may be interpreted as a  $L_2$  projection of the normal derivative at the nodes.

On each quadrature point  $q$  we write:

$$\int_\Gamma \frac{\partial\phi^q}{\partial n} u \, d\gamma = \int_\Gamma -\mathbf{V}_\infty^q \cdot \mathbf{n}^q u \, d\gamma \quad \forall u \in Q \quad (3.9)$$

where  $\partial\phi^q/\partial n$  indicates the potential normal derivative valued at the quadrature points  $\mathbf{x}^q$ . The potential normal derivative  $\partial\phi/\partial n$  is discretized as

$$\frac{\partial\phi^q}{\partial n} = \sum_{j=1}^m \omega_j(\mathbf{x}_q) \frac{\partial\phi}{\partial n_j} \quad (3.10)$$

where  $\omega_j$  is one of the  $m$  basis functions of  $\partial\phi/\partial n$  on a single cell. With equation 3.10 a finite dimensional space has been introduced. Thus it is sufficient to test 3.9 for every of its basis functions. Multiplying this equation by the basis functions and integrating on the surface a new linear system is obtained.

$$\mathbf{M} \frac{\partial\phi}{\partial n} = \mathbf{b}, \quad (3.11)$$



Where a generic  $(i, j)$  element of  $\mathbf{M}$  is

$$M_{ij} = \sum_{k=1}^{N_c} \sum_{q=1}^{N_q} \omega_i(\mathbf{x}_q) \omega_j(\mathbf{x}_q) \quad (3.12)$$

Being  $N_c$  is the number of cells and  $N_q$  the number of quadrature points on each cell. Each element of  $\mathbf{b}$  is assembled as follows

$$\mathbf{b}_i = - \sum_{k=1}^{N_c} \sum_{q=1}^{N_q} \omega_i(\mathbf{x}_q) \mathbf{V}_\infty(\mathbf{x}_q) \cdot \mathbf{n}(\mathbf{x}_q) \quad (3.13)$$

The mass matrix is sparse because every basis function  $\psi_j$  has compact support. If the chosen finite element space is discontinuous  $\mathbf{M}$  is block-diagonal. This set of equations are readily applied to the previous BEM system. Every line where a Neumann boundary condition is imposed is replaced by the corresponding line of this new system. We compare the solutions obtained with the new treatment of Neumann conditions against the classical one by assessing the convergence rate in the  $L_2$  norm. The approximation for  $\phi$  and  $\partial\phi/\partial n$  are reported in Table 3.2 at page 50. Figure 3.8 presents the comparison between  $L_2$  norm of the error for the potential  $\phi$  between the two different implementations of Neumann condition. While Figure 3.9 presents the comparison between  $L_2$  norm of the error for the potential normal derivative  $\partial\phi/\partial n$  between the two different implementations of Neumann condition.

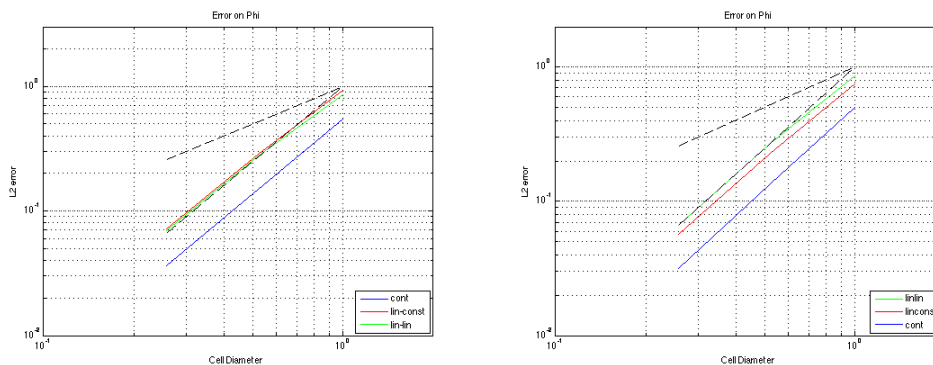


**Figure 3.8:** The blue line represents the  $L_2$  error of  $\phi$  for the reference case, which employs continuous linear elements both for  $\phi$ , and  $\partial\phi/\partial n$ . The red line refers to the results of the hybrid BEM with continuous element for  $\phi$ , and piecewise constant elements for  $\partial\phi/\partial n$ . The green line is the hybrid BEM error obtained with continuous linear elements for  $\phi$ , and discontinuous linear elements for  $\partial\phi/\partial n$ . The black dotted lines show reference slopes per linear and quadratic convergence. On the left, the typical implementation of Neumann boundary condition is reported, on the right, the implementation through the weak formulation

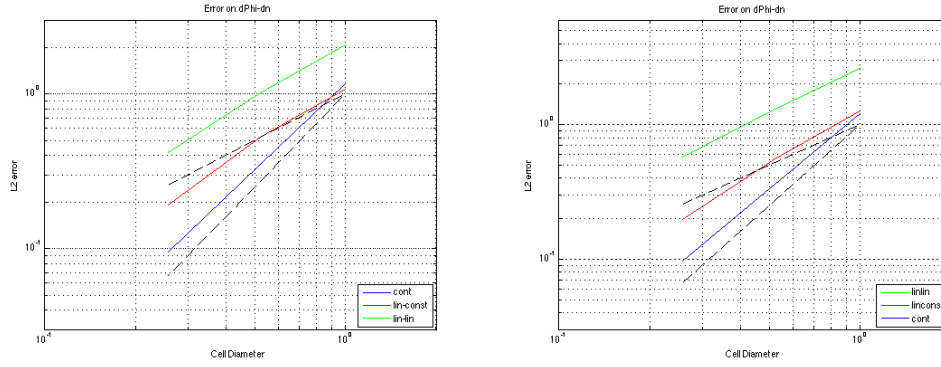


**Figure 3.9:** The blue line represents the  $L_2$  error of  $\partial\phi/\partial n$  for the reference case, which employs continuous linear elements both for  $\phi$ , and  $\partial\phi/\partial n$ . The red line refers to the results of the hybrid BEM with continuous element for  $\phi$ , and piecewise constant elements for  $\partial\phi/\partial n$ . The green line is the hybrid BEM error obtained with continuous linear elements for  $\phi$ , and discontinuous linear elements for  $\partial\phi/\partial n$ . The black dotted lines show reference slopes per linear and quadratic convergence. On the left, the typical implementation of Neumann boundary condition is reported, on the right, the implementation through the weak formulation

The convergence rate of the two formulations for  $\phi$ , in Figure 3.8, is identical. Through for this test case the weak formulation gives a slighter smaller error. Even for the normal derivative, see Figure 3.9, the three curves present the same behavior. It is worth to remark here that the absolute value of the  $\partial\phi/\partial n$  error if the Neumann condition is implemented in the weak formulation is the same as the Neumann condition are implemented in the typical form.

## 3.2 Test Problem 2: Spheroid

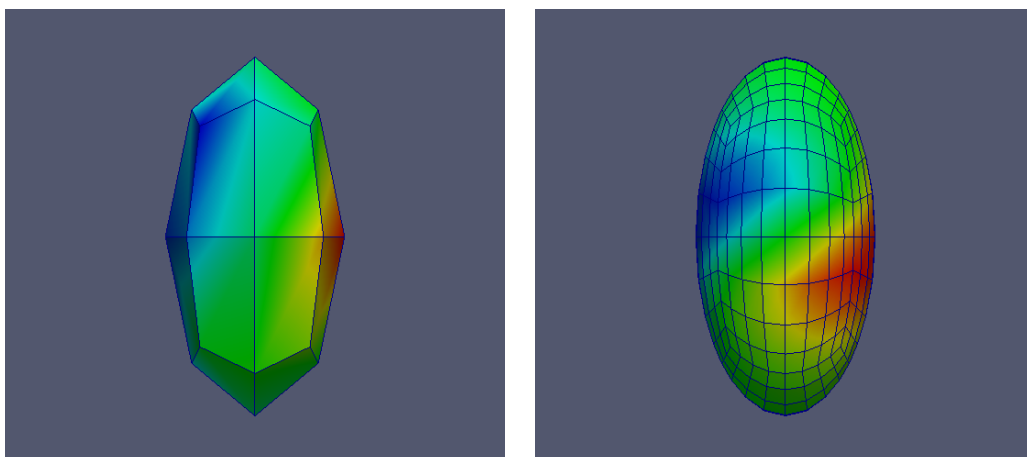


**Figure 3.10:** On the left the spheroid mesh with a single refinement, on the right, the final mesh obtained with three uniform refinement

The geometry studied in the previous problem was symmetric and this may have helped the convergence of the method. Even the solution imposed in the previous problem was very regular and simple, this may have contributed to the super-convergence of the second order scheme, a new, more complex solution, is considered to assess the presence of a super-convergence in the previous case.

The new surface where the BEM is used is a spheroid having principal axes which coincide with the reference frame axes  $x, y, z$ . The length of the spheroid is one along  $x$  and  $y$  axes and two along  $z$  axis. Hence the aspect ratios are  $1 : 1 : 2$ . The potential to be imposed is the following, see [16]

$$\phi = 2 \frac{xz}{(x^2 + y^2 + z^2)^{5/2}} - \frac{y}{(x^2 + y^2 + z^2)^{3/2}}, \quad (3.14)$$

the Neumann condition assumes the form

$$\begin{aligned}
\frac{\partial\phi}{\partial n} = & \frac{2x}{\left( (2x)^2 + (2y)^2 + \left(\frac{2z}{2}\right)^2 \right)^{1/2}} ((2z + 3xy)(x^2 + y^2 + z^2)^{-5/2} - 10x^2z(x^2 + y^2 + z^2)^{-7/2}) + \\
& + \frac{2y}{\left( (2x)^2 + (2y)^2 + \left(\frac{2z}{2}\right)^2 \right)^{1/2}} (-(x^2 + y^2 + z^2)^{-3/2} + 3y^2(x^2 + y^2 + z^2)^{-5/2} \\
& - 10xyz(x^2 + y^2 + z^2)^{-5/2}) + \frac{\frac{2z}{2^2}}{\left( (2x)^2 + (2y)^2 + \left(\frac{2z}{2}\right)^2 \right)^{1/2}} ((2x + 3yz)(x^2 + y^2 + z^2)^{-5/2} \\
& - 10xz^2(x^2 + y^2 + z^2)^{-5/2}).
\end{aligned} \tag{3.15}$$

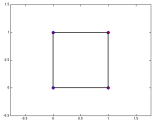
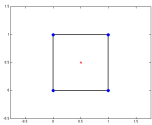
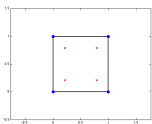
This condition will be imposed both in the classical way and using the new weak form to assess the performance of the proposed new formulation.

### 3.2.1 Convergence analysis

Even in this case the convergence analysis is performed considering both linear and quadratic approximations for  $\phi$  and  $\partial\phi/\partial n$ . In addition a separate convergence analysis will be performed to test the weak imposition of Neumann condition.

### 3.2.2 First order elements

In this test case the same mixed boundary conditions of the sphere case are imposed. The potential  $\phi$  from equation (3.14) is imposed when  $y < 0$ , and the potential normal derivative  $\partial\phi/\partial n$  from equation (3.15) is imposed when  $y \geq 0$ . The comparison between the reference continuous linear solution and two hybrid one is performed. As in the previous test case, the reference solution method is based on a continuous linear approximation for  $\phi$  and a continuous linear approximation for  $\partial\phi/\partial n$ . For this reason, only hybrid methods with linear discontinuous and piecewise constant approximations for  $\partial\phi/\partial n$  are here considered. As before, at each refinement cycle every cell is divided in four. The linear methods applied are illustrated in Table 3.4:

Label	Collocation points	Coarse	Medium	Refined
Cont		52 dofs	196 dofs	772 dofs
Lin-Const		50 dofs	194 dofs	770 dofs
LinLin		122 dofs	482 dofs	1922 dofs

**Table 3.4:** Scheme of the 2D reference cell employed. Blue dots depict the collocation points of the linear continuous approximation, used for  $\phi$  in all three methods. Red crosses indicate the collocation points for the discontinuous approximation of  $\partial\phi/\partial n$  used in the hybrid method. Coarse, Medium, and refined indicate the degrees of freedom employed by a single BEM at every refinement step.

Figure 3.11 shows the  $L_2$  norm of the error on  $\phi$

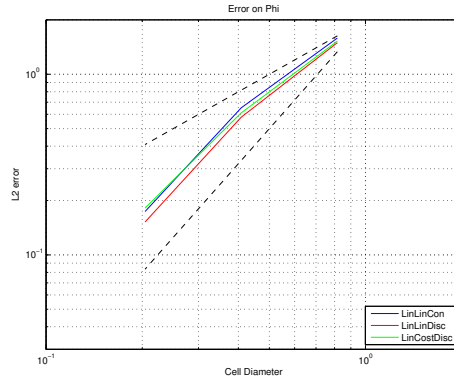


**Figure 3.11:** The blue line represents the  $L_2$  error of  $\phi$  for the reference case, which employs continuous linear elements both for  $\phi$ , and  $\partial\phi/\partial n$ . The green line refers to the results of the hybrid BEM with continuous element for  $\phi$ , and piecewise constant elements for  $\partial\phi/\partial n$ . The red line is the hybrid BEM error obtained with continuous linear elements for  $\phi$ , and discontinuous linear elements for  $\partial\phi/\partial n$ . The black dotted lines show reference slopes per linear and quadratic convergence.

It can be seen that the three methods present almost the same behavior.

They all tend in fact to a second order convergence degree as in the sphere test case. The lowest error value is that of the hybrid BEM with linear discontinuous  $\partial\phi/\partial n$  discretization still the three methods appear almost identical.

The  $L_2$  norm error on  $\partial\phi/\partial n$  is presented in figure 3.12

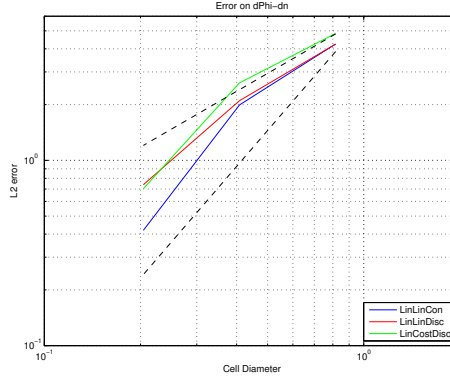


**Figure 3.12:** The blue line represents the  $L_2$  error of  $\partial\phi/\partial n$  for the reference case, which employs continuous linear elements both for  $\phi$ , and  $\partial\phi/\partial n$ . The green line refers to the results of the hybrid BEM with continuous element for  $\phi$ , and piecewise constant elements for  $\partial\phi/\partial n$ . The red line is the hybrid BEM error obtained with continuous linear elements for  $\phi$ , and discontinuous linear elements for  $\partial\phi/\partial n$ . The black dotted lines show reference slopes per linear and quadratic convergence.

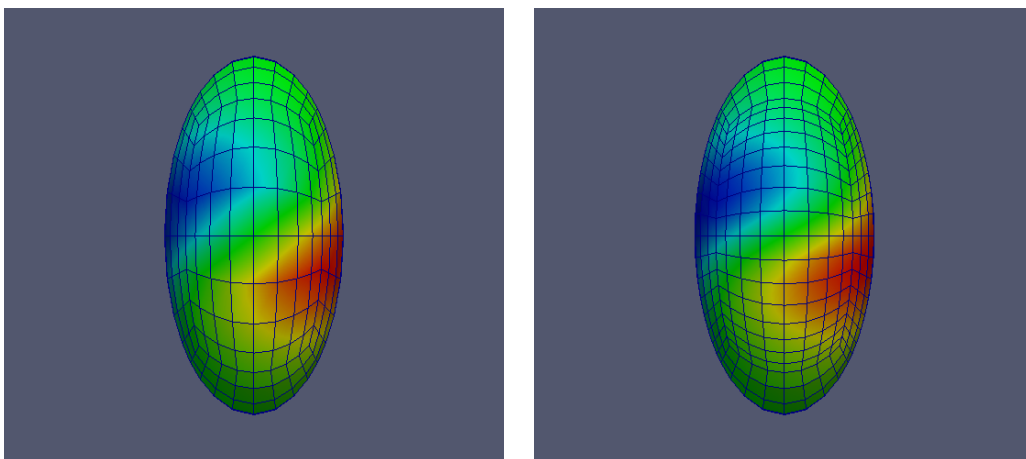
It is very interesting that the reference continuous linear approximation for both  $\phi$ , and  $\partial\phi/\partial n$ , and the method with piecewise constant hybrid approximation for  $\partial\phi/\partial n$  almost have the same behavior, being close to second order convergence. The method with linear discontinuous approximation for  $\partial\phi/\partial n$  shows an order of convergence which is closer to 1.5, with lower accuracy in respect to the other methods. In conclusion, the reference continuous linear method still seems to be the best choice because it has the better orders of convergence and the lowest values of error in the  $L_2$  norm. It is worth pointing out that the change in the geometry hasn't affected the orders of convergence of the method significantly. Nonetheless some jumps are present in these convergence plots, which may be caused by the stretching of the cells.

### 3.2.3 First order elements. Convergence Analysis with isotropic grids

The previous grid on the spheroid is simply obtained morphing the original grid of the sphere example. Every refinement is done on the original sphere and then projected on the prolate spheroid. With such procedure, some cell become

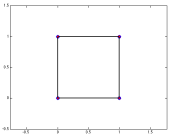
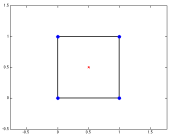
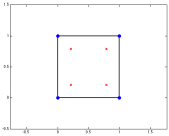
very stretched, which may introduce some numerical problems.

To avoid this, it is possible to introduce a new starting grid which is already stretched. In the sphere case the original unrefined mesh was a cube while now the refinement starts from a rectangular parallelepipedon. Over this new starting mesh it is possible to implement a function which removes the cell anisotropy through anisotropic cell refinement in order to have cells with a maximum aspect ratio of 1.5. The final mesh, after 3 refinement cycles can be seen in Figure 3.13



**Figure 3.13:** On the left, a sketch of the original mesh. On the right, the the corresponding mesh with the anisotropic cells removal

The removal of mesh anisotropies has increased the number of degrees of freedom. Table 3.5 reports the new approximations used with anisotropies removal. The convergence results, in  $L_2$  norm, obtained using isotropic meshes are reported in Figure 3.14 for the potential  $\phi$ , and in Figure 3.15 for  $\partial\phi/\partial n$  respectively.

Label	Collocation points	Coarse	Medium	Refined
Cont		84 dofs	324 dofs	1284 dofs
Lin-Const		82 dofs	322 dofs	1282 dofs
LinLin		122 dofs	482 dofs	1922 dofs

**Table 3.5:** Scheme of the 2D reference cell employed. Blue dots depict the collocation points of the linear continuous approximation, used for  $\phi$  in all three methods. Red crosses indicate the collocation points for the discontinuous approximation of  $\partial\phi/\partial n$  used in the hybrid method. Coarse, Medium, and refined indicate the degrees of freedom employed by a single BEM at every refinement step.

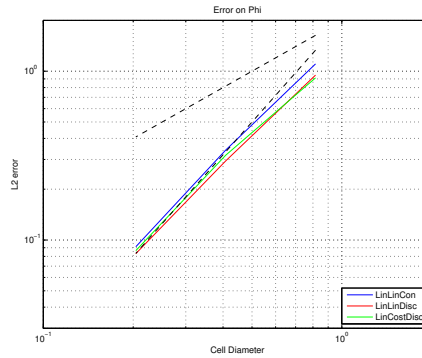


**Figure 3.14:** The blue line represents the  $L_2$  error of  $\phi$  for the reference case, which employs continuous linear elements both for  $\phi$ , and  $\partial\phi/\partial n$ . The green line refers to the results of the hybrid BEM with continuous element for  $\phi$ , and piecewise constant elements for  $\partial\phi/\partial n$ . The red line is the hybrid BEM error obtained with continuous linear elements for  $\phi$ , and discontinuous linear elements for  $\partial\phi/\partial n$ . The black dotted lines show reference slopes per linear and quadratic convergence.



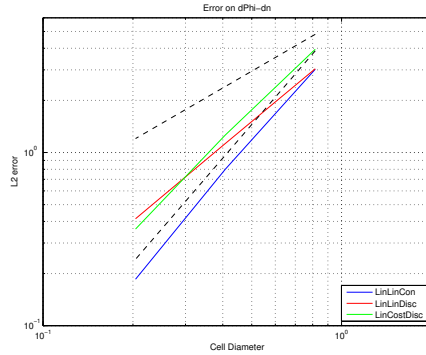


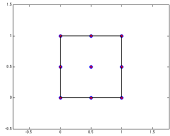
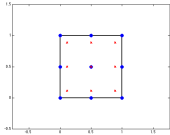
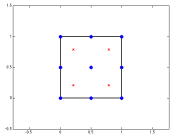
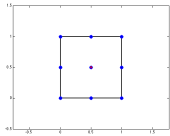
**Figure 3.15:** The blue line represents the  $L_2$  error of  $\partial\phi/\partial n$  for the reference case, which employs continuous linear elements both for  $\phi$ , and  $\partial\phi/\partial n$ . The green line refers to the results of the hybrid BEM with continuous element for  $\phi$ , and piecewise constant elements for  $\partial\phi/\partial n$ . The red line is the hybrid BEM error obtained with continuous linear elements for  $\phi$ , and discontinuous linear elements for  $\partial\phi/\partial n$ . The black dotted lines show reference slopes per linear and quadratic convergence.

Both for  $\phi$  and  $\partial\phi/\partial n$  error curves the convergence is more regular than that discussed in the previous section. For the potential field error the three methods show the same behavior. As for the potential normal derivative field error the reference continuous linear method and the hybrid method with piecewise constant  $\partial\phi/\partial n$  approximation presents a better behavior approaching second order accuracy. The method with discontinuous linear  $\partial\phi/\partial n$  approximation, which has the highest number of degrees of freedom, shows the worst order of convergence,  $\sim 1.5$ . Finally, it is also important to stress that these advantages in terms of error value coming from isotropic grids are not free, since such meshes have more degrees of freedom than stretched ones.

Nonetheless, it is more important to highlight that with the isotropic grids the convergence is more regular than in the previous cases, and this is due to the elimination of the elongated cells.

### 3.2.4 Quadratic Elements. Convergence Analysis with isotropic grids

To test whether the super convergence was due to the particular symmetry of the sphere combined with the simplicity of the problem a second order convergence analysis has been performed on a spheroid. For such analysis the chosen mesh is the isotropic mesh discussed in the previous paragraph. This way, errors due to excessive cell elongation are avoided. The same approximations already used in the sphere test case are considered. This means that  $\phi$  is always approximated with continuous quadratic elements, while continuous quadratic, discontinuous quadratic, linear discontinuous and piecewise constant elements have been tested for the approximation of  $\partial\phi/\partial n$ . The quadrilateral reference elements and corresponding location of the degrees of freedom on the reference cell are depicted in table 3.6

Label	Collocation points	Coarse	Medium	Refined
cont		324 dofs	1284 dofs	5124 dofs
Quad-Quad		522 dofs	2082 dofs	8322 dofs
Quad-Lin		322 dofs	1282 dofs	5122 dofs
Quad-Const		202 dofs	792 dofs	3202 dofs

**Table 3.6:** Scheme of the 2D reference cell employed. Blue dots indicate the collocation point of the linear continuous approximation. Red crosses indicate collocation points for the discontinuous approximation. Coarse, Medium, and refined indicate the degrees of freedom employed by a single BEM at every refinement step.

Figure 3.16 shows the curves of the  $L_2$  error for  $\phi$  and  $\partial\phi/\partial n$

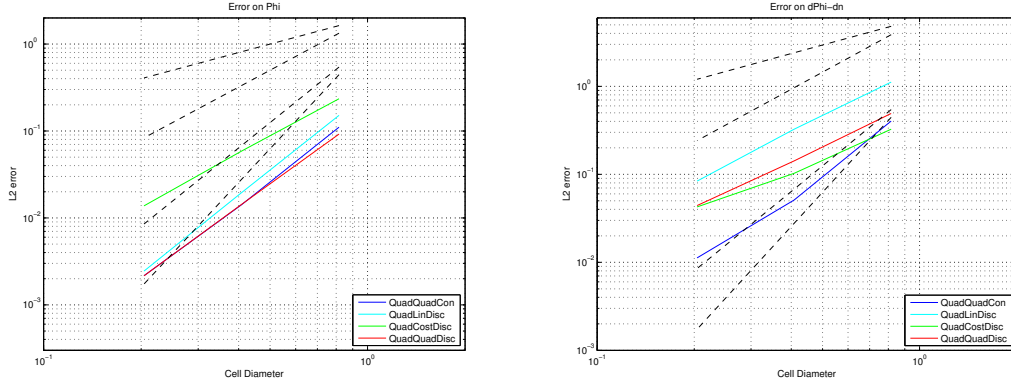
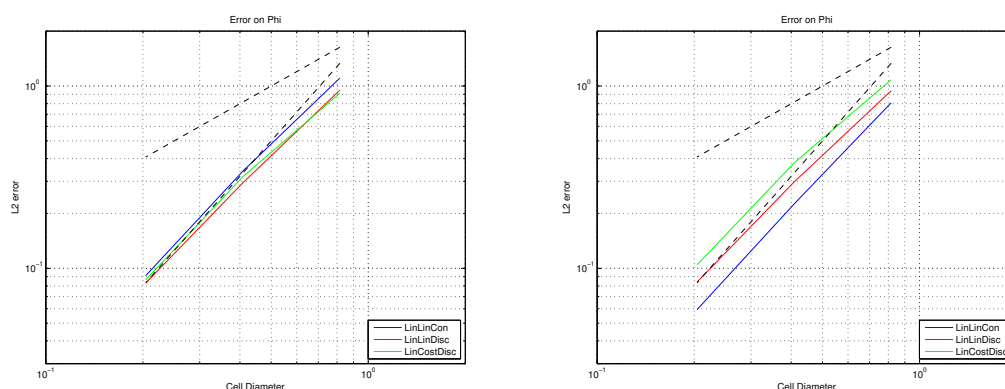


**Figure 3.16:** On the left, the convergence analysis for  $\phi$ . On the left, the convergence analysis for  $\partial\phi/\partial n$ . The blue line represents the  $L_2$  error of  $\phi$  for the reference case, which employs continuous quadratic elements both for  $\phi$ , and  $\partial\phi/\partial n$ . The red line refers to the results of the hybrid BEM with continuous quadratic element for  $\phi$ , and quadratic discontinuous elements for  $\partial\phi/\partial n$ . The cyan line is the hybrid BEM error obtained with continuous quadratic elements for  $\phi$ , and discontinuous linear constant elements for  $\partial\phi/\partial n$ . The green line is the hybrid BEM error obtained with continuous quadratic elements for  $\phi$ , and discontinuous piecewise constant elements for  $\partial\phi/\partial n$ . The black dotted lines show reference slopes per first, second, third and fourth order of convergence.

The plots of Figure 3.16 show that the fourth order accuracy obtained in the sphere test case was indeed a result of the simplicity of the first test case. Here the approximation reference continuous and quadratic both for  $\phi$ , and  $\partial\phi/\partial n$  only shows a third order convergence with respect to the fourth order on of the sphere case. The hybrid method with piecewise constant  $\partial\phi/\partial n$  approximation has almost degree two, which is the same degree obtained with the linear approximation of  $\phi$  reported in the previous section. Thus, the additional degrees of freedom of the quadratic approximation does not translate in higher accuracy. The hybrid BEM with quadratic discontinuous approximation for  $\partial\phi/\partial n$  shows almost the same order of convergence then the one with  $\partial\phi/\partial n$  continuous quadratic approximation, but it has much higher computational costs. The most efficient hybrid scheme appears to be the one with linear discontinuous  $\partial\phi/\partial n$  approximation. It almost recovers the same order of convergence of the BEM with quadratic continuous  $\partial\phi/\partial n$  approximation, and it roughly has the same computational cost.

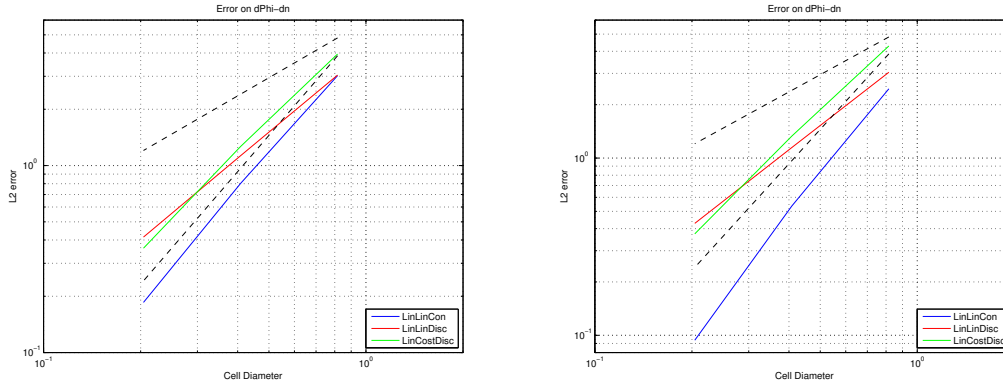
### 3.2.5 Alternative implementation of Neumann condition

Table 3.4 at page 61 reports the tested approximation. Figure 3.17 presents the comparison between  $L_2$  norm of the error for the potential  $\phi$  obtained using the two different implementations of Neumann condition discussed in section 3.1.5



**Figure 3.17:** The blue line represents the  $L_2$  error of  $\phi$  for the reference case, which employs continuous linear elements both for  $\phi$ , and  $\partial\phi/\partial n$ . The green line refers to the results of the hybrid BEM with continuous element for  $\phi$ , and piecewise constant elements for  $\partial\phi/\partial n$ . The red line is the hybrid BEM error obtained with continuous linear elements for  $\phi$ , and discontinuous linear elements for  $\partial\phi/\partial n$ . The black dotted lines show reference slopes per linear and quadratic convergence. On the left, the typical implementation of Neumann boundary condition is reported, on the right, the implementation through the weak formulation

The curves obtained with the weak implementation of Neumann condition have lower error. The behavior of the curves is the same for both the implementations. Figure 3.18 presents the comparison between  $L_2$  norm of the error for the potential normal derivative  $\partial\phi/\partial n$  between the two different implementations of Neumann condition



**Figure 3.18:** The blue line represents the  $L_2$  error of  $\partial\phi/\partial n$  for the reference case, which employs continuous linear elements both for  $\phi$ , and  $\partial\phi/\partial n$ . The green line refers to the results of the hybrid BEM with continuous element for  $\phi$ , and piecewise constant elements for  $\partial\phi/\partial n$ . The red line is the hybrid BEM error obtained with continuous linear elements for  $\phi$ , and discontinuous linear elements for  $\partial\phi/\partial n$ . The black dotted lines show reference slopes per linear and quadratic convergence. On the left, the typical implementation of Neumann boundary condition is reported, on the right, the implementation through the weak formulation

The three convergence curves present the same behavior for both implementations of Neumann boundary condition. It is worth to remark here that the absolute value of the  $\partial\phi/\partial n$  error is lower if the Neumann condition is implemented in the weak formulation. Thus, the weak formulation appears to be a reliable methodology to impose Neumann boundary data in BEM computations. The advantage of the weak formulation will be clearer when we treat more irregular geometries.

### 3.2.6 Local refinement

To perform the convergence analysis of the previous sections we have followed a global refinement strategy *i.e.* every cell has been divided into four new ones at every cycle. In the present section we follow a local refinement strategy, this means that not all the cells are refined at every cycle but only those in which satisfied a chosen criterium based on a error estimator. This adaptive local refinement strategy should distribute a major number of cells in the regions where the solution is more rapidly changing. This refinement is based on an error estimator which depends on the approximated solution and its gradient, hence it does not require that the exact solution is available.

The error indicator used is the one proposed by Kelly, Gago, Zienkiewicz and Babuska, [17]. It approximates the error on each cell by considering the  $L_2$  norm of the jump of the gradient of the approximated solution.

The Kelly error estimator estimates the error for the generalized Poisson equation  $-\nabla a(x)\nabla u = f$  with either Dirichlet or generalized Neumann boundary condition. The following error indicator is computed on each cell

$$\eta_K = \sqrt{\frac{h}{24} \int_{\partial K} \left[ a \frac{\partial u_h}{\partial n} \right]^2 d\sigma} \quad (3.16)$$

The operator  $[x]$  indicates the jump  $x_{in} - x_{out}$ , where  $x_{in}$  and  $x_{out}$  represent the values of the field  $x$  inside and outside the cell boundary respectively.

The estimator returns a vector holding the error estimates for each cell, which is used to set the refining flags on the cells. In the present example a fixed fraction, 30%, of the total cells is refined starting from those with the highest error indicator. This kind of refinement strategy is the only choice when a large domain is involved because a global refinement would introduce an excessive number of degrees of freedom making the computational cost prohibitive.

### 3.2.7 Hanging nodes

Our local refinement procedure leads to nonconformal meshes, *i.e.* to the possibility of having different number of cells on different sides of the same edge. In such situations, on one side of the edge there are more unknowns than on the other, leading to solution with jumps and discontinuities, even for those variables with continuous approximations. To avoid this problem it is necessary to introduce a set of hanging nodes constraints. To clear the meaning of the hanging node constraint let's consider a linear continuous approximation of a generic function  $\gamma$

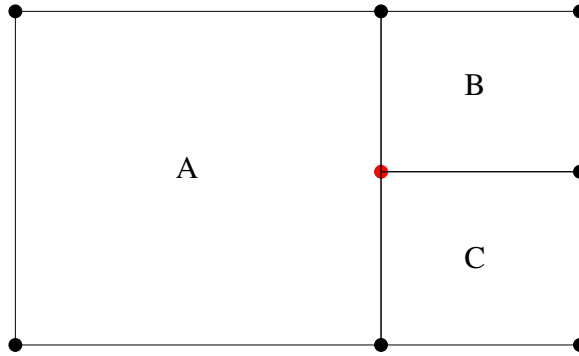


**Figure 3.19:** The red node is the hanging node

In the framework of the proposed method, the hanging nodes created by the local refinement are not truly free as the other ones. They have to satisfy a condition coming from the type of element used in the approximation. For instance

in the linear continuous approximation shown in Figure 3.19, on a side of cell A the solution must be linear and the degrees of freedom are located on the vertices of the cell. If the adjacent cell has been refined, there is a new hanging node on an edge of cell A. The solution must remain continuous across this edge, so the following condition must be satisfied for the generic function  $\gamma$

$$\gamma(x_{hn}) = \gamma_{hn} = 1/2\gamma_i + 1/2\gamma_j, \quad (3.17)$$

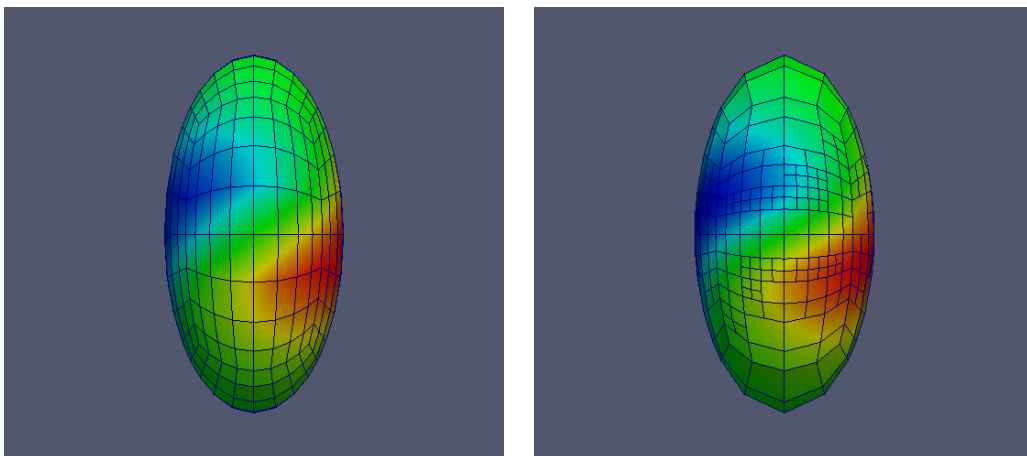
where  $x_{hn}$  is the position of the hanging node and  $\gamma_i, \gamma_j$  the unknowns on the vertexes of the cell A.

In a more general case equation (3.17) becomes

$$\gamma_{hn} + \sum_{i=1}^N \gamma_{hn,i} x_i = 0. \quad (3.18)$$

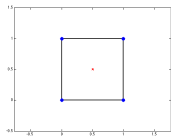
To ensure that the solution for  $\phi$  is continuous the constraint represented by equation (3.18) substitutes the line corresponding to the BIE collocated on hanging node in the algebraic BEM system. This correction is used only with continuous approximations. For example, no hanging node continuity constraints are needed by the potential normal derivative if a hybrid method is applied, since the solution may be discontinuous over the edge.

### 3.2.8 Results



**Figure 3.20:** On the left, the mesh after three global refinement cycles. On the right, the final mesh refined after 6 local refinement cycles

In this section an example of local refinement is reported for the prolate spheroid test case. The local refinement is here applied to the hybrid method with continuous linear approximation for the potential and piecewise constant approximation for the potential normal derivative, since it has been proved that with global refinements this approximation matches sufficiently well the continuous linear reference method.

Label	Collocation points
Lin-Const	

**Table 3.7:** Scheme of the 2D reference cell employed. Blue dots depict the collocation point of the linear continuous approximation. Red crosses indicate collocation points for the discontinuous approximation

It is expected that a refinement concentrated where the solution gradients are higher can produce a better convergence rate, or at least equivalent results, in terms of error absolute value with respect to a simple global refinement.

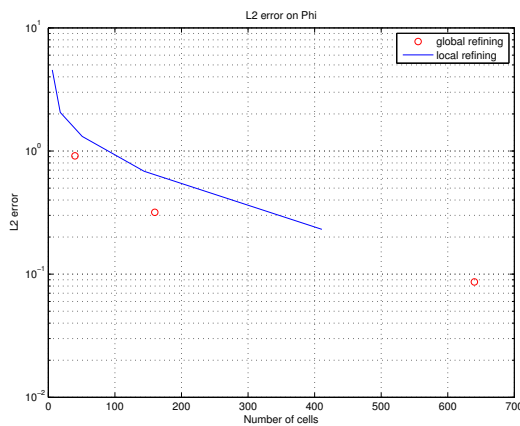


**Figure 3.21:** The blue line represents the  $L_2$  error of  $\phi$  for the hybrid method combined with the local refinement strategy. The red dots represent the  $L_2$  error of  $\phi$  for the hybrid method combined with the global refinement strategy



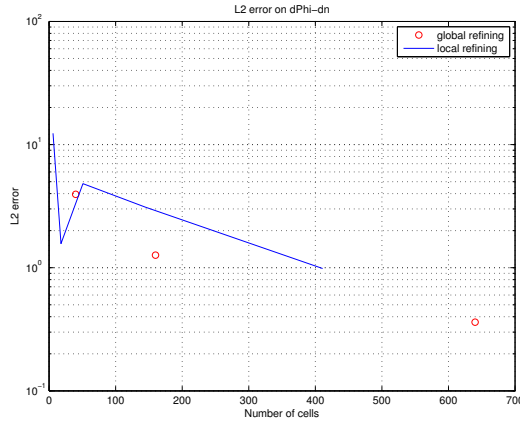


**Figure 3.22:** The blue line represents the  $L_2$  error of  $\partial\phi/\partial n$  for the hybrid method combined with the local refinement strategy. The red dots represent the  $L_2$  error of  $\partial\phi/\partial n$  for the hybrid method combined with the global refinement strategy

As far as the potential  $\phi$  is concerned, it can be seen that when a similar number of cell is considered, a similar error is achieved with both refinement strategies. The fact that the exact solution appears to be quite regular must be pointed out, as the global refinement in such situation may still be the best choice. For  $\partial\phi/\partial n$  it can be seen that the locally refined solution has, for high number of cells, a similar behavior with respect to the globally refined one. At the first refinement step  $\partial\phi/\partial n$  error is growing, but it must be remembered that the local refinement is based on the  $\phi$  solution, so the solution for its potential derivative is not expected to have a regular behavior. The developed hybrid method will be tested with different, and possibly better, error estimator in order to assess wether a better convergenceit can be obtained, yet this task is not a scope of the present work.

In the present test case the global refinement appears to be the best choice in terms of absolute error value. This test case is simple and it is based on a little domain to be discretized so a global refinement strategy can be applied. Nonetheless in more complex cases such a strategy is too expensive to be applied while significative solution gradients are concentrated in limited regions of the computational domain. Therefore, what is important to stress here, is that the local refinement is adequately working on the present method, as it reduces the error at the same rate of the global refinement strategy.

### 3.3 Test Problem 3: solution over a sharp edge

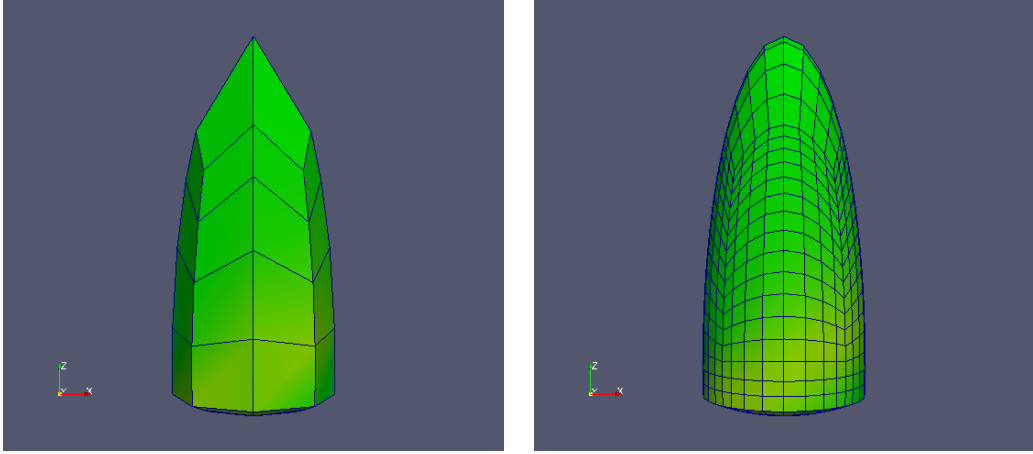


**Figure 3.23:** On the left, the mesh after one global refinement cycle. On the right, the final mesh after four global refinement cycles

The purpose of the present test case is to study the behavior of the hybrid method on a geometry which presents a sharp edge and compare it with the performance of a classical BEM formulation. The body considered in this test is the boolean union between portions of a sphere and of a spheroid. Along the  $z$  axis the sphere has radius 2.5 and is centered in  $P = (0, 0, 1.89)$ . The spheroid has aspect ratio 4 and it is connected to the sphere for  $z = -0.4$ . Thus the domain presents a jump in the normal vector at  $z = -0.4$ . The normal vector has two different analytical expressions on the sides of the conjunction at  $z = -0.4$ , namely

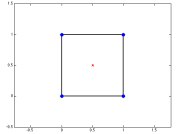
$$\mathbf{n}_{sphere} = \begin{pmatrix} \frac{2x}{\sqrt{4x^2 + 4y^2 + 4z^2}} \\ \frac{2y}{\sqrt{4x^2 + 4y^2 + 4z^2}} \\ \frac{2(z - 1.893)}{\sqrt{4x^2 + 4y^2 + 4(z - 1.893)^2}} \end{pmatrix} \quad (3.19)$$

$$\mathbf{n}_{spheroid} = \begin{pmatrix} \frac{2x}{\sqrt{4x^2 + 4y^2 + 1/64z^2}} \\ \frac{2y}{\sqrt{4x^2 + 4y^2 + 1/64z^2}} \\ \frac{z}{8\sqrt{4x^2 + 4y^2 + 1/64z^2}} \end{pmatrix}. \quad (3.20)$$

A continuous approximation for  $\partial\phi/\partial n$  does not represent this case accurately, as the value of  $\partial\phi/\partial n$  on the edge is in fact discontinuous.

### 3.3.1 Convergence analysis

This test case introduces a new type of problem. Here continuous approximation of  $\partial\phi/\partial n$  is expected to have a worse behavior than a discontinuous one. A possible improvement to the continuous approximation is the introduction of double nodes, as explained in [12, 11]. In the present work no additional treatment is considered over the edge. The same exact potential expression already used for the prolate spheroid, in equation (3.14), is considered. To evaluate the problems introduced by the new geometry, a pure Dirichlet problem has been considered. Only the derivative and its error from the exact solution are here computed. It has been shown in the previous test cases that the hybrid BEM with linear piecewise constant approximation for  $\partial\phi/\partial n$ , coupled with a linear continuous approximation for  $\phi$ , gives equivalent result to the classical BEM with continuous linear approximation both for  $\phi$ , and  $\partial\phi/\partial n$ , only this hybrid method is considered in this last test case.

Label	Collocation points
Lin-Const	

**Table 3.8:** Scheme of the 2D reference cell employed. Blue dots depict the collocation point of the linear continuous approximation. Red crosses indicate collocation points for the discontinuous approximation.

Figure 3.24 shows the results of the convergence analysis. For this test case four global refinement cycles have been performed.

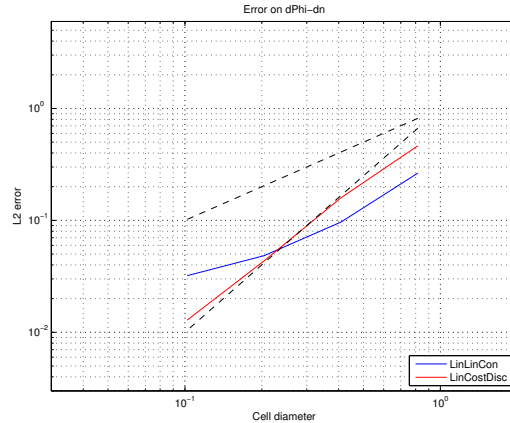


**Figure 3.24:** The blue line represents the  $L_2$  error of  $\partial\phi/\partial n$  for the reference case. The red line refers to the results with piecewise constant discontinuous hybrid BEM. The black dotted lines show reference slopes per linear and quadratic order convergence. On the left, the curves without the implementation of double nodes. On the right, the curves with such an implementation for the continuous case.

In plot of Figure 3.24 the continuous approximation for the derivative has been employed without any correction on the conjunction. This approximation method gives worse results than the hybrid piecewise constant one. This because the method isn't able to treat well the jump of the normal vector. The hybrid method instead naturally deals with such a discontinuity, and it is able to compute accurate values of the potential normal derivative.

In conclusion, the hybrid method has the advantage of not needing any *ad hoc* modification to treat discontinuities of the normal vectors, which are typically associated with sharp edges. This is a great advantage of the hybrid formulation, as sharp edges appears in many practical BEM applications like the waterline on a boat, or the trailing edge of a wing.

To better evaluate the advantage of using a discontinuous approximation for the potential normal derivative, its local error with respect to the exact solution is displayed in Figure 3.25

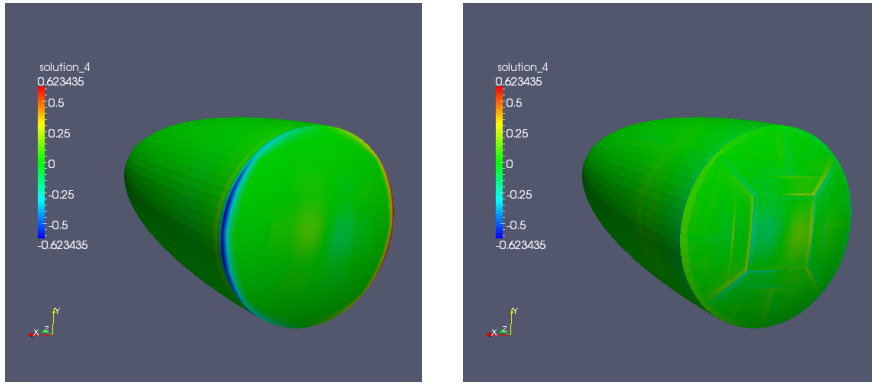


**Figure 3.25:** On the left, the error of  $\partial\phi/\partial n$  for the reference linear continuous approximation without the double nodes. On the right, the error of  $\partial\phi/\partial n$  when it is approximated via piecewise constant discontinuous elements.

The maximum value of the error is higher for the linear continuous approximation of  $\partial\phi/\partial n$ . Such maximum is situated on the edge between the sphere and the spheroid. This is due to the incapacity for a continuous approximation to treat a discontinuity in the normal vector appropriately. In the hybrid BEM with discontinuous piecewise constant approximation the maximum error is situated where the mesh is too coarse to follow the solution properly, but on the edge the solution is computed quite accurately.



# Chapter 4

## Free-Surface Flows

We now consider the problem of a body moving at a constant speed in calm water. The purpose is to study the creation of gravitational waves around the body. Chapter 5.1 deals with the motion of a submerged prolate spheroid, while Chapter 5.2 focuses on the problem of a boat advancing in calm water. Here we present the general algorithm.

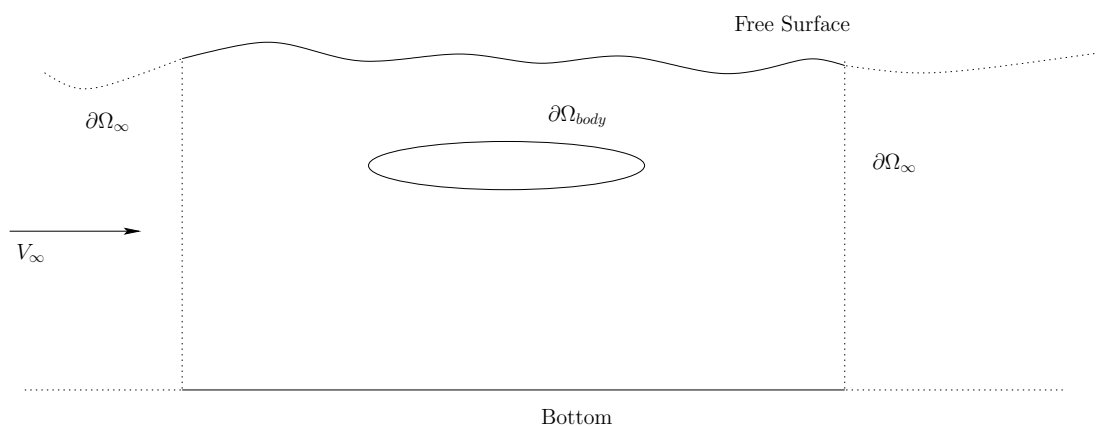


**Figure 4.1:** Vertical section of the domain for the simulation of the flow past a body beneath the water free surface.

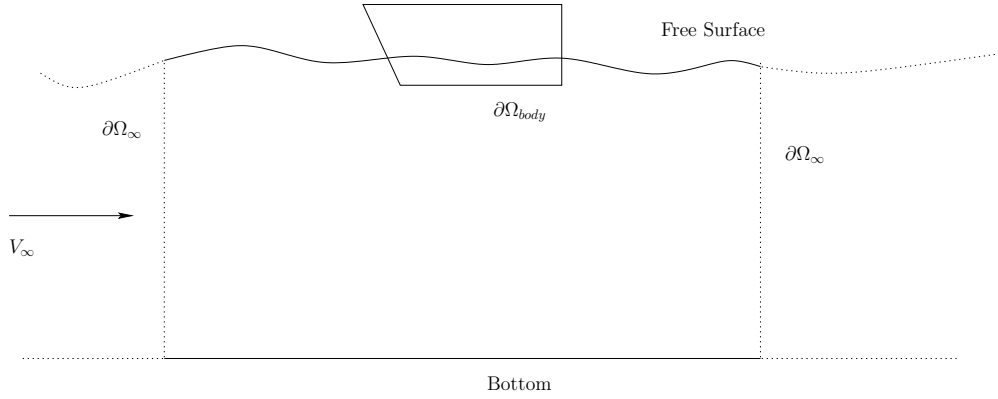


**Figure 4.2:** Vertical section of the domain for the simulation of the flow past a boat located across the water free surface

The flow domain considered in the present work is the portion of water surrounding the body, as referred in Figures 4.1 and 4.2. In this chapter, a model for free surface waves based on linearized potential theory will be presented. The model can deal both with a fully immerse body moving close to the water surface, and with a body located across the free surface.

The flow domain of the BEM simulations employed is bounded by the free surface, the body and by the bottom surfaces, see Figures 4.1 4.2. Also  $\partial\Omega_{\infty}$  is indicated, it represents the truncation surfaces of the numerical domain, it must be far enough from the body to approximate the condition  $\mathbf{x} \rightarrow \infty$ .

If a body is located across the free surface, as Figure 4.2 shows, the domain comprehends only the part of the body beneath the water surface. The dry part of the body is not considered. In the following section the equations of fluid dynamics describing the problem are introduced, with particular regard to the boundary conditions that must be applied on the water free surface.

## 4.1 Basic notation and governing equations

The model considered in the present study is that of the flow of an incompressible inviscid fluid past a body at rest, which is equivalent to that of a body moving at constant speed in a fluid at rest. We neglect viscous forces, so the governing equations of such problem are the incompressible Euler equations of fluid dynamics:

$$\begin{cases} \frac{\partial}{\partial t} \mathbf{v} + (\mathbf{v} \cdot \nabla) \mathbf{v} = -\frac{1}{\rho} \nabla p + \mathbf{g} & \text{in } \Omega \\ \nabla \cdot \mathbf{v} = 0 & \text{in } \Omega \end{cases}, \quad (4.1)$$

where the constant fluid density  $\rho$  and the acceleration  $\mathbf{g}$  due to external forces are given, while the velocity  $\mathbf{v}$  and the pressure  $p$  are the unknowns. Here  $\Omega$  is a



closed region bounded by the body, the free surface and the bottom, in which the fluid moves.

Uniqueness of the solution can be proved if the following boundary conditions are applied, as is reported in David Scullen Phd thesis [25]

$$\begin{aligned} \mathbf{n} \cdot \mathbf{v} &= 0 && \text{on } \partial\Omega \\ \mathbf{v} &= \mathbf{v}_\infty && \text{when } |\mathbf{x}| \rightarrow \infty, \end{aligned} \tag{4.2}$$

which respectively mean that the body is not permeable, and that the fluid is assumed in uniform motion at infinity. These equations can be derived from the Navier–Stokes equations assuming that the viscosity contribution is negligible. Only the stationary solution of the problem will be studied in the present work. For both stationary and non stationary flow, the solution is sought by solving firstly for the velocity in the second equation, and then by substituting in the first equation in order to obtain the pressure.

It is common practice to decompose the fluid velocity into two parts. The former is a uniform constant background field  $\mathbf{v}_\infty$ , and the latter is a perturbation field  $\mathbf{v}_p$  which is due to the presence of the body  $\Omega_{body}$ , such approach has been followed in the present work. Therefore,

$$\nabla \cdot \mathbf{v} = \nabla \cdot (\mathbf{v}_\infty + \mathbf{v}_p) = \nabla \cdot \mathbf{v}_p = 0.$$

If the flow is assumed irrotational, *i.e.*  $\nabla \times \mathbf{v} = 0$  in  $\Omega$ , the velocity  $\mathbf{v}_\infty$ , and consequently also the perturbation velocity  $\mathbf{v}_p$ , can be represented as the gradient of a scalar function. This is consistent with the hypothesis of inviscid flow done before, as in absence of a viscous term, if the initial condition of undisturbed flow is irrotational so it must be the flow at all times, that is

$$\mathbf{v}_p = \nabla\phi.$$

These hypotheses, incompressible and inviscid fluid, uniform initial  $\mathbf{v}_\infty$  and irrotational flow are consistent with many problems involving a flow past a body where the viscosity can be assumed to be confined in a boundary layer of negligible thickness. Thus the total potential can be expressed as formed by two terms

$$\Phi = \phi_\infty + \phi. \tag{4.3}$$

Considering Figure 4.1 and 4.2 the relations expressed in equations (4.4) and (4.5) are satisfied

$$\mathbf{V}_\infty = \nabla\phi_\infty \tag{4.4}$$

$$U_\infty = \|\mathbf{V}_\infty\| \tag{4.5}$$

The second of equations (4.1) above can be rewritten as a Laplace equation. If pure Neumann conditions are imposed on the boundary of the body, and Dirichlet on the outer, infinity,  $\partial\Omega_\infty$  boundary

$$\begin{aligned} \Delta\phi &= 0 && \text{in } \Omega \\ \mathbf{n} \cdot \nabla\phi &= -\mathbf{n} \cdot \mathbf{v}_\infty && \text{on } \partial\Omega_{body} \end{aligned} \quad (4.6)$$

$$\phi = \bar{\phi} \quad \text{when } |\mathbf{x}| \rightarrow \infty. \quad (4.7)$$

Where the last condition ensures unicity. The boundary condition applied on the free surface,  $\partial\Omega_{fs}$ , is the result of a particular free surface modelling, which will be described next. The problem is to be solved numerically, so it is necessary to introduce truncation surfaces at  $\partial\Omega_\infty$  where the boundary condition expressed in (4.7) have to be imposed. These truncation surfaces are often referred to as a numerical tank. In the present work Dirichlet boundary conditions are applied to ensure that away from the body the perturbation potential tends to zero. Under the present assumptions the momentum balance equation, the first of equations (4.1), reduces to Bernoulli's equation that expresses the pressure  $P$  as a function of the potential  $\phi$ , namely

$$\frac{\partial\phi}{\partial t} + \frac{1}{2}\nabla\phi \cdot \nabla\phi + gz + \frac{P}{\rho} = C(t). \quad (4.8)$$

A consequence of irrotational the flow assumption is that the conservation mass equation has completely decoupled from the momentum balance one. Thus, the two problems can be solved one after the other. For example, in order to compute the forces exerted on the body, the Laplace equation is solved first, and then the Bernoulli equation is used with the computed potential solution to evaluate the pressure fields.

## 4.2 Boundary Condition on the Free Surface

A very important hypothesis is introduced on the free surface. As in [20, 22] the free surface elevation along the  $z$  axis is assumed to be representable as a function of  $x$  and  $y$ . That is, the free surface can be expressed as

$$\sigma(x, y, z, t) = z - \eta(x, y, t) = 0 \quad (4.9)$$

It is here remarked that using the hypothesis expressed by (4.9) means that no breaking waves are considered in the present work.

By a kinematic stand point, one requires that the surface  $\sigma(x, y, z, t)$  moves along

with the fluid. Thus the surface  $\sigma(x, y, z, t)$  must be a flow surface. In addition a second, dynamic assumption is introduced. On the free surface the water pressure is assumed to be always equal to the atmospheric pressure  $P_a$ . We have

$$\frac{D}{Dt}(\sigma) = \frac{D}{Dt}(z - \eta) = 0 \quad (4.10)$$

$$\frac{\partial \Phi}{\partial t} + \frac{1}{2} \nabla \Phi \cdot \nabla \Phi + g\eta = C(t). \quad (4.11)$$

The first expression is the so-called kinematic condition and it states that the substantial derivative of the quantity  $z - \eta$  vanishes on the free surface boundary. This because the constraint  $\sigma$  is always null on the free surface. The second equation is the Bernoulli equation, evaluated on the free surface. The time dependent expression  $C(t)$  can be found considering (4.11) at infinity, where the flow is assumed uniform, the perturbation potential, and the free surface elevation are zero.

$$C(t) = \frac{\partial \phi_\infty}{\partial t} + \frac{1}{2} \nabla \phi_\infty \cdot \nabla \phi_\infty + g\eta = \frac{1}{2} \nabla \phi_\infty \cdot \nabla \phi_\infty = \frac{1}{2} U_\infty^2. \quad (4.12)$$

### 4.3 Linearized Free Surface Boundary Condition

In the present section perturbation theory is used to obtain a single linearized boundary condition for the free surface. In equation (4.11) there are two unknown quantities, *i.e.*  $\Phi$  and  $\eta$ . If small perturbation, with respect to the undisturbed asymptotic flow, are considered they can be written as

$$\Phi = \Phi_0 + \epsilon \Phi_1 + O(\epsilon^2) = \phi_\infty + \epsilon \phi + O(\epsilon^2) \quad (4.13)$$

$$\eta = \eta_0 + \epsilon \eta_1 + O(\epsilon^2) = 0 + \epsilon \eta_1 + O(\epsilon^2). \quad (4.14)$$

The kinematic boundary condition, can be written as

$$\frac{D}{Dt}(z - \eta) = \frac{\partial z}{\partial t} + \frac{\partial \Phi}{\partial z} - \frac{\partial \eta}{\partial t} - \frac{\partial \Phi}{\partial x} \frac{\partial \eta}{\partial x} - \frac{\partial \Phi}{\partial y} \frac{\partial \eta}{\partial y} - \frac{\partial \Phi}{\partial z} \frac{\partial \eta}{\partial z} = 0. \quad (4.15)$$

Substituting expressions (4.13) and (4.14) we have, neglecting higher order terms in  $\epsilon$ ,

$$\begin{aligned}
\frac{D}{Dt}(z - \eta) &= \frac{\partial z}{\partial t} + \frac{\partial \Phi_0}{\partial z} + \epsilon \left( \frac{\partial \Phi_1}{\partial x} \frac{\partial z}{\partial x} + \frac{\partial \Phi_1}{\partial y} \frac{\partial z}{\partial y} + \frac{\partial \Phi_1}{\partial z} \frac{\partial z}{\partial z} \right) - \\
&\quad \frac{\partial \eta_0}{\partial t} - \epsilon \frac{\partial \eta_1}{\partial t} - \frac{\partial \Phi_0}{\partial x} \frac{\partial \eta_0}{\partial x} - \frac{\partial \Phi_0}{\partial y} \frac{\partial \eta_0}{\partial y} - \frac{\partial \Phi_0}{\partial z} \frac{\partial \eta_0}{\partial z} + \\
&\quad \epsilon \left( -\frac{\partial \Phi_1}{\partial x} \frac{\partial \eta_0}{\partial x} - \frac{\partial \Phi_1}{\partial y} \frac{\partial \eta_0}{\partial y} - \frac{\partial \Phi_1}{\partial z} \frac{\partial \eta_0}{\partial z} \right) + \\
&\quad \epsilon \left( -\frac{\partial \Phi_0}{\partial x} \frac{\partial \eta_1}{\partial x} - \frac{\partial \Phi_0}{\partial y} \frac{\partial \eta_1}{\partial y} - \frac{\partial \Phi_0}{\partial z} \frac{\partial \eta_1}{\partial z} \right) + \\
&\quad \epsilon^2 \left( -\frac{\partial \Phi_1}{\partial x} \frac{\partial \eta_1}{\partial x} - \frac{\partial \Phi_1}{\partial y} \frac{\partial \eta_1}{\partial y} - \frac{\partial \Phi_1}{\partial z} \frac{\partial \eta_1}{\partial z} \right) = 0.
\end{aligned} \tag{4.16}$$

As  $\eta_0 = 0$  it represents the undisturbed free surface condition. The terms are regrouped to highlight the dependence on  $\epsilon$ .

$$\epsilon \left( \frac{\partial \Phi_1}{\partial z} - \frac{\partial \eta_1}{\partial t} - \frac{\partial \Phi_0}{\partial x} \frac{\partial \eta_1}{\partial x} - \frac{\partial \Phi_0}{\partial y} \frac{\partial \eta_1}{\partial y} - \frac{\partial \Phi_0}{\partial z} \frac{\partial \eta_1}{\partial z} \right) + \epsilon^2 \left( -\frac{\partial \Phi_1}{\partial x} \frac{\partial \eta_1}{\partial x} - \frac{\partial \Phi_1}{\partial y} \frac{\partial \eta_1}{\partial y} - \frac{\partial \Phi_1}{\partial z} \frac{\partial \eta_1}{\partial z} \right). \tag{4.17}$$

Since we want to obtain a linearized boundary condition only the terms linear with respect to  $\epsilon$  are considered, obtaining

$$-\frac{\partial \Phi_1}{\partial z} + \frac{\partial \eta_1}{\partial t} + \frac{\partial \Phi_0}{\partial x} \frac{\partial \eta_1}{\partial x} + \frac{\partial \Phi_0}{\partial y} \frac{\partial \eta_1}{\partial y} + \frac{\partial \Phi_0}{\partial z} \frac{\partial \eta_1}{\partial z} = 0. \tag{4.18}$$

In addition  $\Phi_0 = U_\infty x$ , and since we consider only steady state solutions, the previous equation reduces to

$$-\frac{\partial \Phi_1}{\partial z} + \frac{\partial \Phi_0}{\partial x} \frac{\partial \eta_1}{\partial x} = 0. \tag{4.19}$$

Equation (4.19) is the linearized kinematic boundary condition. It can be rewritten using the unknowns of the original problem  $\eta, \phi$  considering  $\Phi_1 = \phi, \eta_1 = \eta$ ,

$$\frac{\partial \phi}{\partial z} - U_\infty \frac{\partial \eta}{\partial x} = 0. \tag{4.20}$$

The same technique is now applied to equation (4.11)

$$\begin{aligned}
\frac{\partial \Phi}{\partial t} + \frac{1}{2} \nabla \Phi \cdot \nabla \Phi + g\eta &= \frac{\partial \Phi_0}{\partial t} + \epsilon \frac{\partial \Phi_1}{\partial t} + \frac{1}{2} \nabla \Phi_0 \cdot \nabla \Phi_0 + \epsilon \frac{1}{2} \nabla \Phi_0 \cdot \nabla \Phi_1 + \\
&\quad \epsilon \frac{1}{2} \nabla \Phi_1 \cdot \nabla \Phi_0 + \epsilon^2 \frac{1}{2} \nabla \Phi_1 \cdot \nabla \Phi_1 + g\eta_0 + \epsilon g\eta_1 = \frac{1}{2} U_\infty^2.
\end{aligned} \tag{4.21}$$

Regrouping the terms with the same power of  $\epsilon$  and considering that  $\frac{1}{2}\nabla\Phi_0 \cdot \nabla\Phi_0 = \frac{1}{2}U_\infty^2$ ,  $\partial\Phi_0/\partial t = 0$  and  $\eta_0 = 0$  results in

$$\epsilon \left( \frac{\partial\Phi_1}{\partial t} + \nabla\Phi_0 \cdot \nabla\Phi_1 + g\eta_1 \right) + \epsilon^2 \left( \frac{1}{2}\nabla\Phi_1 \cdot \nabla\Phi_1 \right) = 0. \quad (4.22)$$

If again only linear terms, with respect to  $\epsilon$  are considered, and a steady state solution is assumed, the dynamic condition becomes

$$\nabla\Phi_0 \cdot \nabla\Phi_1 + g\eta_1 = 0. \quad (4.23)$$

In terms of the usual variables  $U_\infty, \phi, \eta$ , it yields

$$U_\infty \frac{\partial\phi}{\partial x} + g\eta = 0. \quad (4.24)$$

Equations (4.24) and (4.19) represent the linearized boundary conditions on the free surface. If (4.24) is differentiated with respect to  $x$ , namely

$$U_\infty \frac{\partial^2\phi}{\partial x^2} + g \frac{\partial\eta}{\partial x} = 0, \quad (4.25)$$

it is possible to combine (4.25) with (4.24) to write a linearized free surface boundary condition in which only  $\phi$  appears:

$$U_\infty^2 \frac{\partial^2\phi}{\partial x^2} + g \frac{\partial\phi}{\partial z} = 0. \quad (4.26)$$

Equation (4.26) is imposed on the undisturbed free surface  $z = 0$ , where the normal vector  $\mathbf{n}$  is directed as the  $z$  axis, so (4.26) is in fact equivalent to

$$U_\infty^2 \frac{\partial^2\phi}{\partial x^2} + g \frac{\partial\phi}{\partial n} = 0 \quad \text{at } z = 0. \quad (4.27)$$

Such linearized free surface boundary condition will be used in this work to study the interactions between moving bodies and the free surface.

## 4.4 Waves behavior

In Figure 4.3 real ship waves are displayed



**Figure 4.3:** Typical Kelvin wake for a piercing surface body. Well defined V-shaped wake with typical featherlets.

A well defined pattern is recognizable. This kind of pattern is very peculiar as it forms a kind of a V with the boat at the point. The waves along each wake line are "feathery" in appearance. The individual featherlet waves also have a limited extension along their crests. Another clearly visible component of the wave pattern is a transverse curved waves behind the body. In this section a simplified qualitative model for the wave pattern of a body moving near a free surface is described. Such model is that proposed by Frank S. Crawford in [7]. It is based on the boundary conditions for the bottom and the free surface introduced in the previous sections. For the sake of simplicity let's consider a harmonic wave in the  $(x, z)$ .

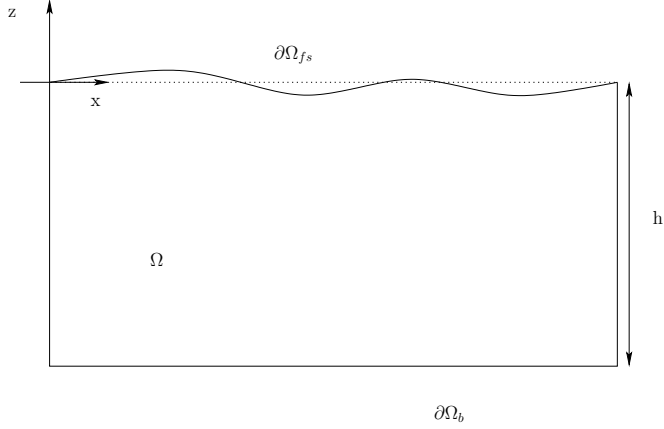


**Figure 4.4:** The domain of the model for 2D waves

The bottom is considered at depth  $z = -h$ . In this section there isn't any exterior flow and the solution is not at steady state. From equation (4.17) it can be derived that

$$\frac{\partial \eta_1}{\partial t} - \frac{\partial \Phi_1}{\partial z} = 0 \Rightarrow \frac{\partial \eta}{\partial t} - \frac{\partial \Phi}{\partial z} = 0, \quad (4.28)$$

and from equation (4.22)

$$\frac{\partial \Phi_1}{\partial t} + g\eta_1 = 0 \Rightarrow \frac{\partial \Phi}{\partial t} + g\eta = 0. \quad (4.29)$$

Combining equations (4.28) with (4.29), a single linearized free surface boundary condition is obtained

$$\frac{\partial^2 \Phi}{\partial t^2} + g \frac{\partial \Phi}{\partial z} = 0. \quad (4.30)$$

Let's recall the set of equations to be satisfied.

$$\Delta \Phi = \frac{\partial^2 \Phi}{\partial x^2} + \frac{\partial^2 \Phi}{\partial z^2} = 0 \quad \text{in } \Omega \quad (4.31)$$

$$\frac{\partial \Phi}{\partial z} = 0 \quad \text{on the Bottom } z = -h \quad \partial \Omega_b \quad (4.32)$$

$$\frac{\partial^2 \Phi}{\partial t^2} + g \frac{\partial \Phi}{\partial z} = 0 \quad \text{on the Free surface } \partial \Omega_{fs}. \quad (4.33)$$

Every wave can be expressed as a sum of harmonic waves. Thus the kinematic potential of the flow field can be written as

$$\Phi = \text{Re} \left( Z(z) e^{-ikx + i\omega t} \right). \quad (4.34)$$

Where  $\omega$  is the angular frequency, and  $k$  is the wavenumber, which represents the spatial frequency of such a wave. A moving observer with velocity equal to  $\omega/k$  would see the wave as steady state so it is possible to introduce the phase velocity

$$V_{phase} = V_p = \frac{\omega}{k}. \quad (4.35)$$

It must be pointed out that the free surface elevation wave is strictly connected with the potential by (4.29). Using expression (4.34) to solve the Laplacian governing equation and imposing the boundary condition at  $z = -h$  yields the ordinary differential equation

$$\begin{cases} \frac{d^2 Z}{dz^2} - k^2 Z = 0 \\ \frac{\partial \Phi}{\partial z} = \frac{dZ}{dz} = 0 \text{ at } z = -h. \end{cases} \quad (4.36)$$

Which is used to compute

$$Z = C \frac{\cosh(k(z+h))}{\cosh(kh)}. \quad (4.37)$$

At this point, the free surface boundary condition is imposed and the so called dispersion relation can be found

$$-Re(\omega^2 Z(z) e^{-ikx+i\omega t}) + g Re\left(\frac{dZ(z)}{dz} e^{-ikx+i\omega t}\right) = 0 \quad (4.38)$$

$$-\frac{\omega^2}{g} \cosh(k(z+h)) + k \sinh(k(z+h)) = 0 \quad (4.39)$$

$$k \operatorname{tgh}(kh) = \frac{\omega^2}{g} \quad (4.40)$$

Given  $h, \omega$  it is possible to compute  $V_p, k$  of the wave. From this two interesting consideration can be done

$$\begin{cases} k^2 h = \frac{\omega^2}{g} & h \rightarrow 0 \\ k = \frac{\omega^2}{g} & h \rightarrow \infty \end{cases} \quad (4.41)$$

$$\begin{cases} V_p = \frac{\omega}{k} = \sqrt{gh} & h \rightarrow 0 \\ V_p = \frac{\omega}{k} = \sqrt{\frac{g}{k}} & h \rightarrow \infty. \end{cases} \quad (4.42)$$



With shallow water hypothesis nondispersive waves can be seen because their velocity doesn't depend on their wavenumber. In infinite depth case the phase velocity depends on the wavenumber, so there is the formation of the so called frequency dispersion. This is the case studied in the present work. The frequency dispersion implies that there can be interactions between waves having different wavelengths. If there is a single wave its phase will propagate with  $V_p$ , if there is a band of wavelengths, every wave travels with its own phase velocity. Thus the overall wave results distorted. When a narrow band of wavelengths is considered, the different phase velocities may cause destructive interaction causing the waves to travel with a well defined group velocity  $V_g$  and  $V_g \neq V_p$ , since there isn't only one  $V_p$ . The group velocity is defined as

$$V_g = \frac{\partial \omega}{\partial k} = \frac{1}{2} \sqrt{\frac{g}{k}} = \frac{1}{2} V_p \quad \text{if } h \rightarrow \infty. \quad (4.43)$$

These consideration can justify the classic Kelvin's wake that can be observed downstream a boat as the peaks of the groups of waves, for the usual phase velocities this relation implies that the peaks are located on a line at around  $17^\circ / 21^\circ$  from the centerline.

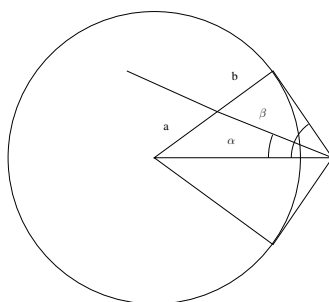


**Figure 4.5:** Graphic construction of the Kelvin waves angle for a little wavenumber

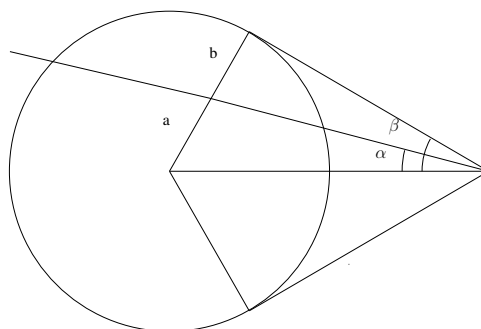


**Figure 4.6:** Graphic construction of the Kelvin waves angle for a large wavenumber

From these two figures it can be seen that even if two different wavenumber have been considered the geometric construction, suggested in [7], shows quite well that the group angle, the one at which the Kelvin wake is seen, remains very similar. In the figures the segments  $a, b$  have the same length  $V_g T = 0.5V_p T$ , where  $T$  is the period of the wave oscillation, so their common point can be seen as the point where the peak corresponding to the group velocity appears. In the following table 4.1 numeric results are reported in order to show that the Kelvin angle remains in proximity of  $20^\circ$ .

**Table 4.1:** Kelvin angle for the 2D model

Case	Phase angle $\beta$	Group angle $\alpha$
1	$40^\circ$	$17^\circ$
2	$55^\circ$	$19^\circ$
3	$70^\circ$	$16^\circ$

We now discuss the transverse component of the wave pattern that we have highlighted at the beginning of this section. These waves are generated by point disturbances of the water induced by the boat as it moves along its trajectory. These disturbances produce circular waves. Far from their origin they can be approximated as straight waves propagating in the same direction as the boat. This wave pattern is attached to the boat so we expect their phase velocities to be in a narrow band centered on the boat speed. When the boat crosses a point, that we call  $B_1$ , it sets that point oscillating. Then the boat crosses a second point,  $B_2$ , and it sets also this point oscillating. Because of the destructive interactions that we have highlighted before, the only crests visible between  $B_1$  and  $B_2$  are those in a region half way between them.

Thus we have the rule that any curved way we see following the boat and lagging behind the boat a distance  $L$ , has its most important parent at a point  $B_1$  located a distance  $2L$  behind the boat.

# Chapter 5

## Test Cases

To validate the behavior of our method in the treatment of free surface flows, three different problems are considered. In the first test case we have treated the motion of a submerged prolate spheroid at constant speed. In the second problem we have considered the motion of a surface piercing body, the Wigley hull. In the last case we have treated a non analytic CAD hull the DTMB5415.

These flows are benchmarks in the naval literature so there are many available references to value the method we have developed.

### 5.1 Submerged prolate spheroid

The purpose of this section is to study the flow field caused by of the motion past a fully submerged prolate spheroid advancing at constant speed in calm water. The domain we have considered is a box of fluid surrounding the spheroid. The longest axis of the spheroid is oriented along the  $x$  axis of the global frame of reference. The spheroid has been placed at a prescribed depth, intended as the distance between the main axis and the free surface. The considered free surface portion is represented by the upper face of the parallelepiped. The truncation faces of the domain,  $\Gamma_{in} \cup \Gamma_{out} \cup \Gamma_{tank}$  in Figure 5.1 are placed far enough from the spheroid, so as not to influence the solution near it.

The considered prolate spheroid has an axis of length 1 meter along the  $x$  direction, of length 0.2 meter along  $y$  direction, axis of length 0.2 meter along  $z$  direction. So we compute  $L_{sph} = 1$  meter.

The truncation faces along the  $x$  axis are placed at  $L_{\infty x} = 9 * L_{sph}$ , along the  $y$  axis at  $L_{\infty y} = 5 * L_{sph}$ , along the  $z$  axis at  $L_{\infty z} = 10 * L_{sph}$ . Along the  $z$  axis there is instead enough water to consider an infinite depth approximation, so as to compare the data with the theory introduced by Havelock in 1931, and reported in [13], which will be used here as a benchmark. Havelock derived an analytical

expression for the the wave resistance of a spheroid submerged in water.

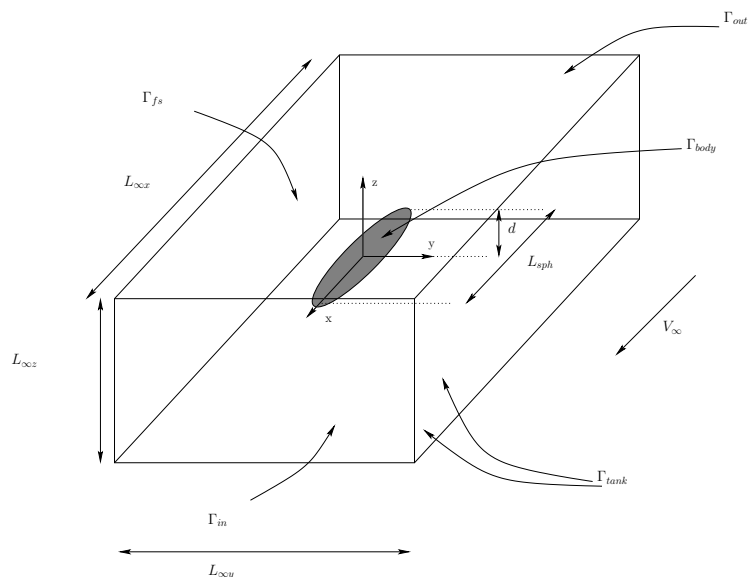


**Figure 5.1:** The spheroid is put under the free surface at a defined depth and it is possible to see also the outer tank set with  $L_{\infty x}$ ,  $L_{\infty y}$ ,  $L_{\infty z}$ . The flow enters from  $\Gamma_{in}$ ,  $\Gamma_{tank}$  are the lateral surfaces and the bottom

Figure 5.2 depicts the corresponding computational domain,

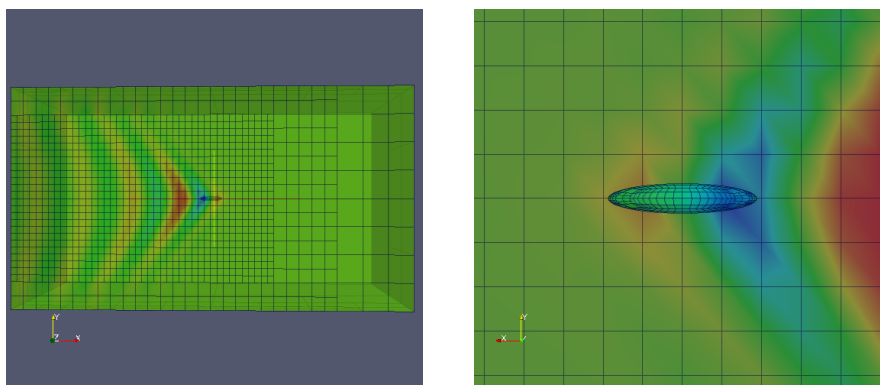


**Figure 5.2:** On the left, a view of the mesh on the free surface. On the right, a detail of the mesh on the submerged spheroid.

As can be noticed in Figure 5.2 the possibility of having nonconformal and unstructured meshes has been effectively exploited here allowing for the concentration of the degrees of freedom where the waves are expected to be, i.e. on the

free surface around the spheroid.

The results reported in the first part of the present work show that the hybrid BEM with a discontinuous approximation for the potential normal derivative  $\partial\phi/\partial n$  gives results comparable with the typical continuous BEM formulation.

In free surface flow simulations, computing properly the unknowns on the edges is mandatory, in particular when a surface piercing hull is considered. In facts, the highest solution gradients are located near the hull, so it is important to compute the unknowns correctly on the edge formed by water and body. One way to solve the problem is to implement the classical continuous BEM with specific edge treatments as proposed by Grilli in [12, 11]. Another possibility is to use the developed hybrid BEM to treat discontinuous solutions naturally.

For this reason a hybrid BEM has been chosen in the following tests, where a linear continuous approximation is used for the potential  $\phi$ , and a piecewise constant discontinuous approximation is used for  $\partial\phi/\partial n$ .

### 5.1.1 Treatment of the linearized free surface boundary condition

As a result of the discussion of Chapter 4 we write the Laplace problem, with the complete set of boundary conditions that will be used for the simulations of the water flow past the ellipsoid, namely

$$\Delta\phi = 0 \quad \text{in } \Omega \quad (5.1a)$$

$$\frac{\partial\phi}{\partial n} = -U_\infty \cdot \mathbf{n} \quad \text{on } \Gamma_{body} \quad (5.1b)$$

$$\frac{\partial\phi}{\partial n} = -\frac{U_\infty^2}{g} \frac{\partial^2\phi}{\partial x^2} \quad \text{on } \Gamma_{fs} \quad (5.1c)$$

$$\frac{\partial\phi}{\partial n} = 0 \quad \text{on } \Gamma_{out} \cup \Gamma_{tank} \quad (5.1d)$$

$$\phi = 0 \quad \text{on } \Gamma_{in}. \quad (5.1e)$$

In this chapter we will discuss the discretization method based on the Boundary Element Method described in Chapters 2, and 3. In particular we will show how such method can be modified to deal with the linearized boundary condition (4.27). Such equation is treated on the free surface through the collocation of the usual Boundary Integral Equation

$$\alpha(\mathbf{x})\phi(\mathbf{x}) = \phi_\infty + \frac{1}{4\pi} \int_{\partial\Omega} \frac{1}{|\mathbf{x} - \mathbf{y}|} \mathbf{n} \cdot \mathbf{v}_\infty ds_y + \frac{1}{4\pi} \int_{\partial\Omega} \frac{(\mathbf{x} - \mathbf{y}) \cdot \mathbf{n}_y}{|\mathbf{x} - \mathbf{y}|^3} \phi(\mathbf{y}) ds_y. \quad (5.2)$$

The lines of the BEM algebraic matrix corresponding to the degrees of freedom of  $\partial\phi/\partial n$  on the free surface are replaced by a line built from two different sparse matrices. These are not regular Neumann conditions, where only a mass matrix line and a right hand side element have to be assembled, see section 3.1.5. On the free surface, boundary condition (5.1c) relates the normal derivative  $\partial\phi/\partial n$  with the second derivative of the potential along the  $x$  axis. Thus in the line corresponding to such a condition there will be two components coming from the matrices that describe those operators. The way this method has been implemented is explained in more detail at the end of the present section.

The geometry is symmetric with respect to  $y, z$  and to  $x, z$  planes. While the second symmetry is physically meaningful, the first one is not, as waves generated by the surging body only propagate in the downwind direction with respect to relative the flow velocity.

However, the proposed free surface condition cannot reproduce this lack of symmetry, as it is clearly satisfied by solutions which presents symmetry with respect to  $y, z$  plane. Thus, it is necessary to implement an additional condition, described in [25, 21, 4], called radiation condition.

A common way to solve this problem, and obtain a physical Kelvin wake, is to implement a particular Green function, called Kelvin source, which automatically satisfies the free surface condition and employ the radiation condition. This is rather complicated because Kelvin sources are much more complex than the classic Rankine sources.

Another strategy, proposed in 1977 by C.W.Dawson [8], is to use upwind finite difference scheme to compute the second derivative of the potential appearing in (5.1c) so that upstream waves are suppressed. More precisely he proposed to solve a different condition coming from the splitting of  $\Phi_{tot}$  into a double body potential and a perturbation potential. The double body potential is obtained by solving a BEM problem, where the body and the Rankine Green function have been mirrored above the free surface, or equivalently considering homogeneous Neumann boundary condition on the undisturbed free surface.

The implementation is complex and the method is suitable only for structured cartesian grids. We wanted to adopt a simpler formulation. In the present work the boundary condition (5.1c) is imposed directly, using the standard usual potential decomposition  $\Phi_{tot} = \phi_{ext} + \phi$ . To satisfy a radiation condition we impose a homogeneous Dirichlet condition on the inflow surface of the domain, as suggested by David Scullen in [25]. A closer look on what really led to the suppression of the upstream waves in Dawson's work, indicates that it was the use of the upwind finite differences for the computation of the second order derivative of the potential, appearing in equation (5.1c). Although this strategy proved to be successful, it presents two main drawbacks. Firstly it introduces a considerable amount of nu-

merical dissipation. But more importantly, it forces the use of structured meshes which do not allow for local refinement strategies.

To avoid these drawbacks, we resorted to a set of tools used in finite element computations. First off, we compute the potential derivatives in weak form, so as to use unstructured grids too. In addition, to perform such derivative in an upwind way, we use a Streamline Upwind Petrov Galerkin (SUPG) method. To do so we define the SUPG basis functions, as suggested by J.E. Akin in [1]:

$$H_j^{SUPG}(x) = H_j(x) + \alpha h \nabla H_j(x) \cdot \frac{v(x)}{\|v\|}. \quad (5.3)$$

Here the constant  $0 \leq \alpha \leq 1$  sets the relative amount of upwinding on each cell. We have tried different values for this quantity as proposed in [1]. The results in the present work are obtained considering  $\alpha = 1/\sqrt{2}$ . Since the diameter  $h$  of the cell is used in case of square cells, the streamwise cell dimension is recovered. Since the major part of the flow velocity is given by  $U_\infty$  directed along the  $x$  axis, the SUPG weight function we have implemented reads

$$H_j^{SUPG}(x) = H_j(x) + \frac{1}{\sqrt{2}} d \nabla_x H_j(x) \cdot \frac{U_\infty(x)}{\|U_\infty\|}. \quad (5.4)$$

The most important advantage of using the weak formulation combined with the SUPG method is that it allows the use of unstructured grids. In particular, it is possible to employ a grid which is more refined near the position of the spheroid under the water, or to adopt a local refinement strategy based on the solution estimated errors. In addition, SUPG is a strongly consistent method and does not introduce numerical dissipation in the system.

In order to compute in a correct way the second derivative along the  $x$  axis, an additional degree of freedom is added to the system, representing the potential derivative along the direction  $x$ ,  $\phi_x$ . In this way the linearized free surface boundary condition is imposed using the SUPG derivative along  $x$  of  $\phi_x$ . The potential derivative along  $x$  is recovered using a weak formulation. The unknowns of the problem become

$$\phi = \sum_{i=1}^N \psi(\mathbf{x})_i \phi_i \quad (5.5)$$

$$\frac{\partial \phi}{\partial n} = \sum_{i=1}^R \omega(\mathbf{x})_i \frac{\partial \phi}{\partial n_i} \quad (5.6)$$

$$\frac{\partial \phi}{\partial x} = \sum_{i=1}^M \chi(\mathbf{x})_i \frac{\partial \phi}{\partial x_i}. \quad (5.7)$$

the weak formulations of the derivative along  $x$  and the imposition of the linearized free surface boundary condition are

$$\int_{\Gamma} \chi_i^{SUPG} \chi_j \frac{\partial \phi}{\partial x_j} d\gamma = \int_{\Gamma} \chi_i^{SUPG} \frac{\partial}{\partial x} (\phi) d\gamma \quad (5.8)$$

$$\int_{\Gamma} \omega_i^{SUPG} \omega_j \frac{\partial \phi}{\partial n_j} d\gamma = -\frac{U_{\infty}^2}{g} \int_{\Gamma} \omega_i^{SUPG} \frac{\partial}{\partial x} \left( \frac{\partial \phi}{\partial x} \right) d\gamma. \quad (5.9)$$

The presence of the degree of freedom  $\partial\phi/\partial x$  adds to the global algebraic system other  $M$  lines, formed by the sparse system obtained by the discretization equation (5.8). It is also necessary to choose a proper finite element approximation for  $\partial\phi/\partial x$ . In the present work it has been approximated with the same linear continuous approximation used for the potential  $\phi$ .

The procedure is similar to what has been done to implement the boundary condition on the body surface, see section 3.1.5. The derivative can be written in two different ways. The derivative along  $x$  must be found, this is composed by the  $x$  surface derivative and by the normal derivative along the  $x$  component of the normal vector  $\mathbf{n}$

$$\frac{\partial \phi}{\partial x} = \nabla \phi \cdot \mathbf{e}_x = \nabla_s \phi \cdot \mathbf{e}_x + \frac{\partial \phi}{\partial n} \mathbf{n} \cdot \mathbf{e}_x, \quad (5.10)$$

where considering a generic variable  $y$   $\nabla_s$  is defined as follows

$$\nabla_s y = \nabla y - \mathbf{n} (\nabla y \cdot \mathbf{n}). \quad (5.11)$$

On the free surface  $\mathbf{n} \cdot \mathbf{e}_x = 0$ . This term is present if there are degrees of freedom in common between the boat and the free surface. Since the finite element approximation for  $\partial\phi/\partial x$  could be continuous the term involving the normal derivative must be taken into account. Using the finite boundary element approximations introduced in (5.7), equation (5.8) becomes

$$\sum_{c=1}^{N_c} \sum_{q=1}^{N_q} \sum_{j=0}^N \chi_i(\mathbf{x}) \frac{\partial \psi_j(\mathbf{x})}{\partial x} \phi_j + \sum_{c=1}^{N_c} \sum_{q=1}^{N_q} \sum_{r=0}^R \chi_i(\mathbf{x}) \omega_r(\mathbf{x}) n_x \frac{\partial \phi}{\partial n_r} = \sum_{c=1}^{N_c} \sum_{q=1}^{N_q} \sum_{j=0}^M \chi_i(\mathbf{x}) \chi_j(\mathbf{x}) \frac{\partial \phi}{\partial x_j}. \quad (5.12)$$

Where  $N_c$  is the number of cells and  $N_q$  the number of quadrature points in each cell. The quantity  $n_x = \mathbf{n} \cdot \mathbf{e}_x$  is known since it is evaluated on the quadrature points inside the cells. If a SUPG technique is applied, it is sufficient to modify  $\chi_i(\mathbf{x})$  into  $\chi_i^{SUPG}(\mathbf{x})$ . The definition of the SUPG basis is applied as explained in (5.4). To simplify the notation the normal expression of  $\chi_i(\mathbf{x})$  is used in the rest of this explanation. The following system can be written

$$[\mathbf{A}] \frac{\partial \phi}{\partial \mathbf{x}} - [\mathbf{B}] \phi - [\mathbf{C}] \frac{\partial \phi}{\partial \mathbf{n}} = 0, \quad (5.13)$$



where the bold vectors held the unknowns of the finite element approximations of the potential and its derivatives, the generic elements of the matrices can be written as

$$A_{ij} = \sum_{c=1}^{N_c} \sum_{q=1}^{N_q} \chi_i(\mathbf{x}) \chi_j(\mathbf{x}), \quad (5.14a)$$

$$B_{ij} = \sum_{c=1}^{N_c} \sum_{q=1}^{N_q} \chi_i(\mathbf{x}) \frac{\partial \psi_j(\mathbf{x})}{\partial x}, \quad (5.14b)$$

$$C_{ij} = \sum_{c=1}^{N_c} \sum_{q=1}^{N_q} \chi_i(\mathbf{x}) \omega_j(\mathbf{x}) n_x, \quad (5.14c)$$

$$\boldsymbol{\phi} = \{\phi_1, \dots, \phi_{N_\phi}\}, \quad (5.14d)$$

$$\frac{\partial \boldsymbol{\phi}}{\partial \mathbf{n}} = \left\{ \frac{\partial \phi}{\partial n_1}, \dots, \frac{\partial \phi}{\partial n_{N_{\partial\phi/\partial n}}} \right\}, \quad (5.14e)$$

$$\frac{\partial \boldsymbol{\phi}}{\partial \mathbf{x}} = \left\{ \frac{\partial \phi}{\partial x_1}, \dots, \frac{\partial \phi}{\partial x_{N_{\partial\phi/\partial x}}} \right\}. \quad (5.14f)$$

This system is added to the original one introduced in the first part of this work, see section 2.4, so now three scalar unknowns are present  $\phi, \partial\phi/\partial n, \partial\phi/\partial x$ . Once an approximation of  $\partial\phi/\partial x$  is available by system (5.13) the surface boundary condition (4.27) is computed starting from

$$\frac{\partial \phi}{\partial n} = -\frac{U_\infty^2}{g} \frac{\partial}{\partial x} \left( \frac{\partial \phi}{\partial x} \right) = -\frac{U_\infty^2}{g} \nabla \frac{\partial \phi}{\partial x} \cdot \mathbf{e}_x = -\frac{U_\infty^2}{g} \left( \nabla_s \frac{\partial \phi}{\partial x} \cdot \mathbf{e}_x + \frac{\partial}{\partial n} \left( \frac{\partial \phi}{\partial x} \right) \mathbf{n} \cdot \mathbf{e}_x \right). \quad (5.15)$$

The finite element approximation for  $\partial\phi/\partial n$  is surely discontinuous. To recover a weak formulation of the free surface boundary condition it is necessary to multiply the former expression by the corresponding basis function  $\omega_i$  (see (5.9)). Since we are using a piecewise constant approximation,  $\omega_i$  corresponds to the characteristic function associated to cell  $i$  only. The condition involving the second derivative is on the free surface, where  $\mathbf{n} \cdot \mathbf{e}_x = 0$ , so the second derivative is computed using only the first term  $\nabla_s \frac{\partial \phi}{\partial x} \cdot \mathbf{e}_x$ , yielding

$$-\frac{U_\infty^2}{g} \sum_{c=1}^{N_c} \sum_{q=1}^{N_q} \sum_{j=0}^M \omega_i(\mathbf{x}) \frac{\partial \chi_j(\mathbf{x})}{\partial x} \frac{\partial \phi}{\partial x_j} = \sum_{c=1}^{N_c} \sum_{q=1}^{N_q} \sum_{j=0}^R \omega_i(\mathbf{x}) \omega_j(\mathbf{x}) \frac{\partial \phi}{\partial n_j}. \quad (5.16)$$

Where M is the total number of  $\partial\phi/\partial x$  degrees of freedom and R the total number of  $\partial\phi/\partial n$  degrees of freedom. Repeating the same consideration made for the

potential derivative along  $x$  it is possible to write a similar linear system

$$[\mathbf{D}] \frac{\partial \phi}{\partial \mathbf{n}} + [\mathbf{E}] \frac{\partial \phi}{\partial x} = 0. \quad (5.17)$$

where

$$D_{ij} = \sum_{c=1}^{N_c} \sum_{q=1}^{N_q} \psi_i(\mathbf{x}) \psi_j(\mathbf{x}), \quad (5.18)$$

$$E_{ij} = \frac{U_\infty^2}{g} \sum_{c=1}^{N_c} \sum_{q=1}^{N_q} \psi_i(\mathbf{x}) \frac{\partial \psi_j(\mathbf{x})}{\partial x}. \quad (5.19)$$

The lines of this system are substituted to the lines of the BEM subsystem corresponding to the support points of the normal derivative approximation that are located on the free surface.

It is worth remarking here, that given the choice of discontinuous approximation method for  $\partial \phi / \partial n$ , in particular in presence of piecewise constant elements, the SUPG correction in (5.16) can be ineffective if  $\nabla \omega_i = 0$  in each point of the cell, as can be seen by the definition of shape function reported in equations (5.3) and (5.4).

We have added the variable  $\phi_x$  to the system, and we compute it through a derivation in weak form. Then we use another derivation in weak form to obtain  $\phi_{xx}$  to impose the linearized free surface boundary condition. In [8, 24] the second derivative is obtained directly through a finite difference scheme, we have instead the possibility to impose the SUPG upwinding two times separately. This is very important, because to obtain the potential derivative along  $x$  at least a linear approximation of the considered variable is needed to effectively employ the SUPG. To compute  $\phi_n$  instead, we have followed two different strategies. It is possible to use another time the SUPG so another at least linear approximation is needed. If we have already used a SUPG upwinding in the computation of  $\phi_x$  it is possible to use a piecewise constant approximation for  $\phi_n$  since the system already has enough upwinding to suppress upstream waves. Employing this second strategy, the degrees of freedom are sensibly reduced (we remind that we do not want any special treatment on the edge so we choose discontinuous elements to describe  $\phi_n$ ). In the present work linear continuous approximations both for the potential and its derivative along  $x$  have been chosen, while piecewise constant elements have been chosen for  $\phi_n$ .

The free surface condition (5.1c) has been treated with the SUPG method and the condition on the inflow and outflow are the ones which impose, along with the SUPG approximation, the radiation condition that sets the right direction to the wave propagation. The free surface elevation will be computed postprocessing the flow potential computed via the resolution of the BEM problem.

We want to highlight the importance of the SUPG method in the approximation of the second derivative in the linearized free surface boundary condition (5.1c). We have chosen as example  $U_\infty = 1.88$  m/sec and we show the isolines of the wave elevation, both when SUPG is used and not used.

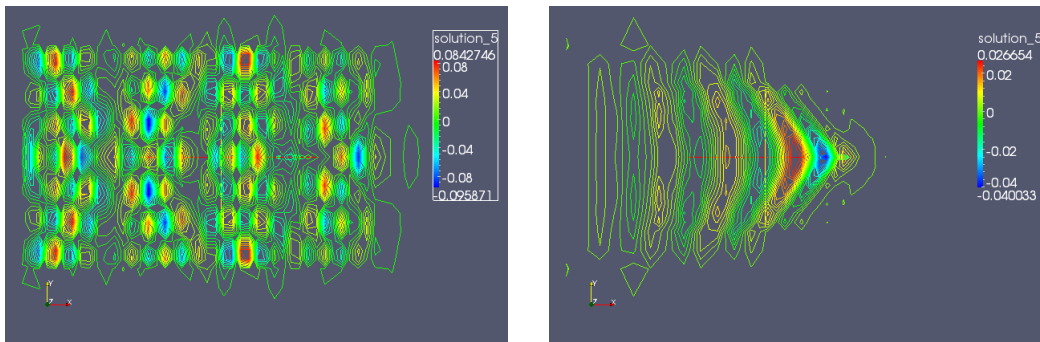


**Figure 5.3:** On the left, isolines representation of free surface elevation field for the chosen velocity without the SUPG stabilization. On the right, isolines representation of free surface elevation field for the chosen velocity with the SUPG stabilization. The colors on the free surface represent numerical contour of the free surface elevation

We can see that the SUPG stabilization plays a key role in our model. As suggested in [8, 25] the upwinding in (5.1c) suppresses the non physical upward propagating waves. In facts, we see that without the SUPG there is a strong presence of waves which propagates upward the body and any physical meaning of the solution is lost. Instead if we consider a SUPG stabilization the physical V-shaped Kelvin wake is recovered. The descriptions of such a wave system, together with its dependency on the flow velocity, are treated in the next section.

### 5.1.2 Qualitative analysis of the wave pattern

The purpose of the present section is to see whether the developed method leads to solutions that are consistent with what can be found in literature about the waves created by a submerged prolate spheroid. To this end it is very interesting to compare the present results to what is explained by David C. Scullen in his Phd thesis [25]. First of all, we chose a sufficient depth of the spheroid axis in order to avoid the presence of strong nonlinear effects. As suggested by Scullen, a good depth is  $f = 1.25d$  where  $d$  is the diameter of the spheroid.

The wave system is expected to present two different features. Firstly, a transverse system should be located after the spheroid. Such wave pattern should appear to be contained in the classic V-shape of the Kelvin wave system. These two peculiarities may be more or less evident in dependence on the velocity oh the

spheroid, which in this section is commonly expressed in terms of Froude number, defined as

$$Fr = \frac{U_\infty}{\sqrt{gL_{spheroid}}}. \quad (5.20)$$

The dependence of the wave pattern on the Froude number will be highlighted in the following discussion.

The wave system is expected to present a clear transition, while the Froude number increases, from one dominated by the transverse system to one with a very clear V-shape. Another typical characteristic is the presence of featherlets on the sides of the system wake. These peak waves, aligned along the arms of the V-shaped pattern, represent a very typical nonlinear effect of a free surface wave, see section 4.4.

In order to visualize the free surface elevation the isolines of the free surface elevation are displayed in Figures 5.4, 5.5, 5.6 and 5.7.

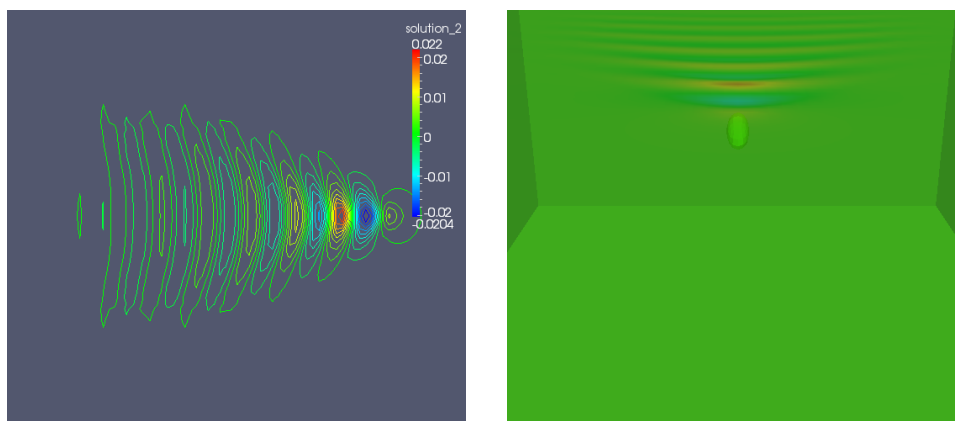


**Figure 5.4:** On the left, isolines representation of free surface elevation field for  $Fr = 0.4$ . On the right, a view of the domain, including spheroid and far field surfaces. The colors on the free surface represent numerical contour of the free surface elevation

At Froude  $Fr = 0.4$  (see Figure 5.4) a clear predominance of a transverse wave can be seen. The V-shaped wave with its typical featherlet pattern it's not evidently present. V-shaped peaks are however present and they are visible near the spheroid, which is located between the first two peaks of the isolines representation.

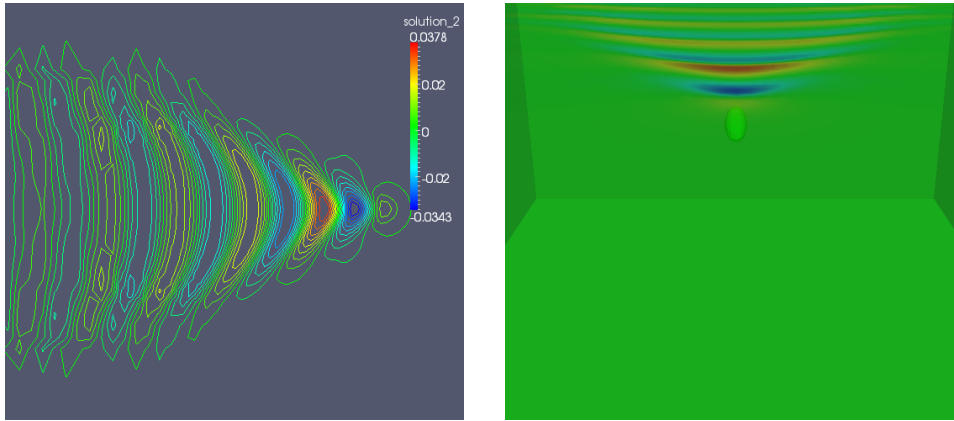


**Figure 5.5:** On the left, isolines representation of free surface elevation field for  $Fr = 0.5$ . On the right, a view of the domain, including spheroid and far field surfaces. The colors on the free surface represent numerical contour of the free surface elevation

At Froude  $Fr = 0.5$  (see Figure 5.5) the spheroid is still between the first two peaks. There is also a noticeable transverse wave which is located after the spheroid. This is consistent with the behavior of the waves as described in the previous sections. There is a stronger V-shaped wave component which can be seen following the peaks, the featherlets, of each transverse wave. The peaks are at an angle of about  $20^\circ$  from the horizontal axis as expected.

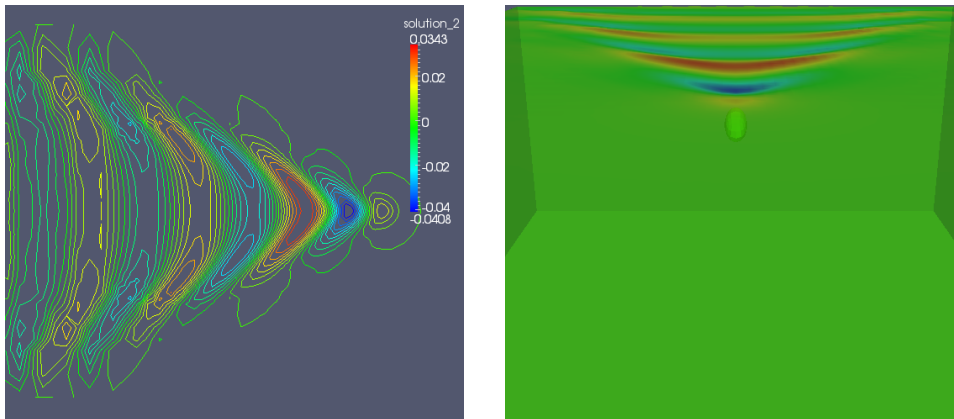


**Figure 5.6:** On the left, isolines representation of free surface elevation field for  $Fr = 0.6$ . On the right, a view of the domain, including spheroid and far field surfaces. The colors on the free surface represent numerical contour of the free surface elevation

At Froude  $Fr = 0.6$  (see Figure 5.6) the spheroid is still between the first two peaks. The transverse wave is visible and, at its sides, the peaks are at an

angle of almost  $20^\circ$  as before. These peaks now are taking the classical shape of the featherlets that are clearly visible in an actual Kelvin wake.

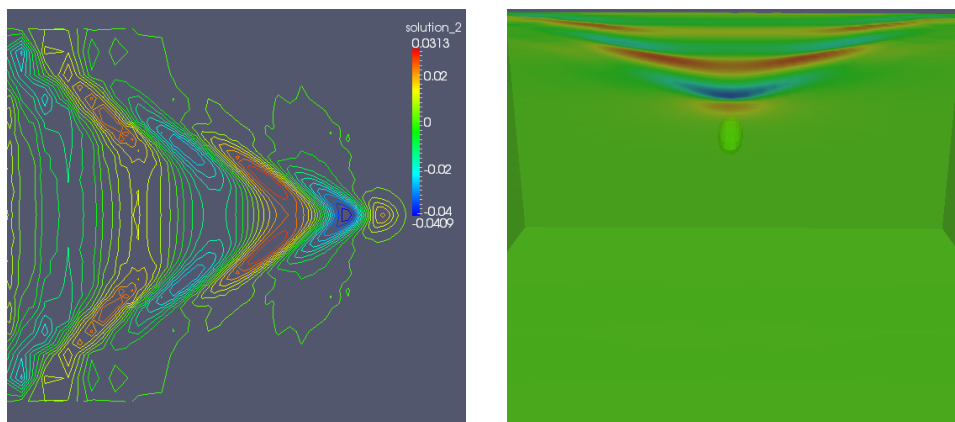


**Figure 5.7:** On the left, isolines representation of free surface elevation field for  $Fr = 0.7$ . On the right, a view of the domain, including spheroid and far field surfaces. The colors on the free surface represent numerical contour of the free surface elevation

At Froude  $Fr = 0.7$  (see Figure 5.7) the most evident component is the V-shaped wave. However the transverse wave remains visible, while the featherlets are now clearly visible. To show that the V-shape angle behaves consistently with the simple model previously described (in section 4.4), the wave angle has been indicated in Figure 5.8 for  $Fr = 0.5$  and for the  $Fr = 0.7$ .

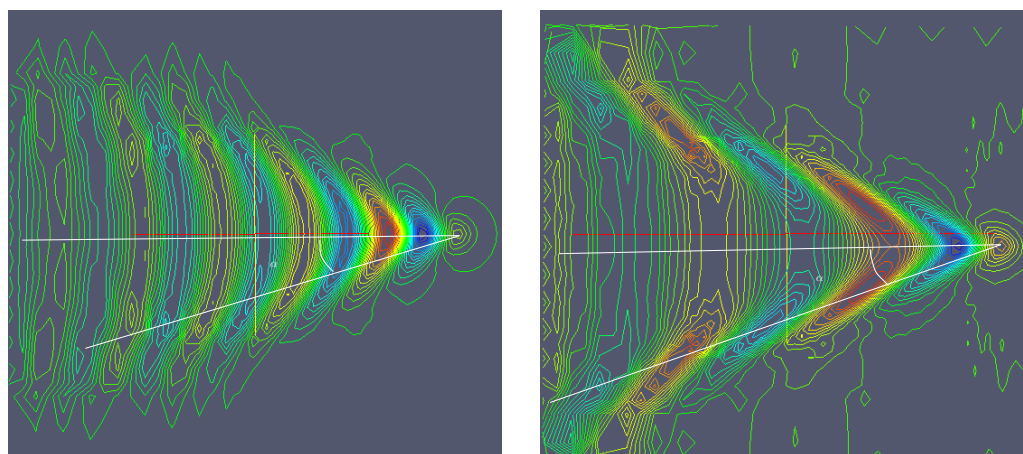


**Figure 5.8:** On the left the Kelvin wave angle for  $Fr = 0.5$ . On the right, the Kelvin wave angle for  $Fr = 0.7$

At  $Fr = 0.5$ , an angle  $\alpha = 16.11^\circ$  is observed, while at  $Fr = 0.7$  the angle is of  $18.02^\circ$ . This fact suggests that the developed method is able to reproduce one

of the most important features of a Kelvin wake.

### 5.1.3 Free surface maximum variation and drag computation

From the previous qualitative analysis it is possible to extract the maximum absolute displacement of the free surface elevation from the reference value  $z = \eta = 0$ . These values can be compared to the ones reported in the literature and in particular to what found in 1998 by David C. Scullen [25]. In Scullen's work a nonlinear steady method was implemented on a structured grid. Even if the present method is based upon a linearization, a comparison is interesting. The comparison of wave elevation peak function as a function of  $Fr$  number is presented in Figure 5.9

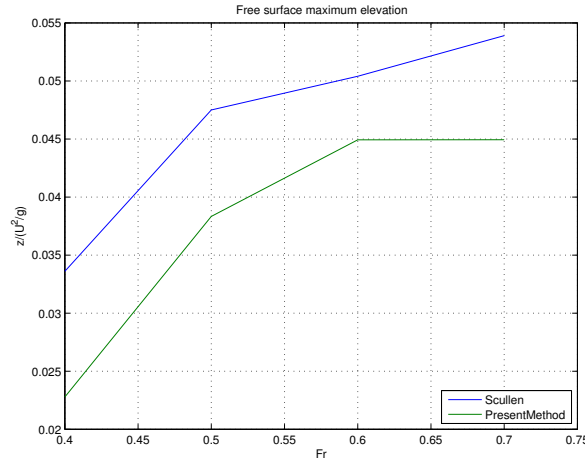


**Figure 5.9:** The blue line represents the results by Scullen. The green line represent the results obtained with the present method

We see that the expected behavior is recovered by the developed method. It can also be seen that the present method underestimates the actual elevation found by the more realistic and accurate nonlinear method. This would be consistent with an underestimation of the drag on the spheroid.

This is because to generate a wave system the spheroid (and in general every kind of boat) displaces a certain quantity of fluid. It is therefore interesting to analyze the drag induced by the wave creation. In 1931 Havelock, in [13], managed to compute an analytical theory to predict the drag of a submerged spheroid. The spheroid was approximated by a series of doublets with a uniform volume distribution and

their axis parallel to the spheroid main axis which, in the present work, is the same direction as that of the external flow velocity. Calling the major semiaxis  $a$  length and the minor semiaxis length  $b$ :

$$e_c = \sqrt{1 - b^2/a^2} \quad (5.21)$$

$$A^{-1} = \frac{4e_c}{1 - e_c^2} - 2 \log \frac{1 + e_c}{1 - e_c} \quad (5.22)$$

$$D_w = 128\pi^2 g \rho a^3 e_c^3 A^2 e^{-p} \int_0^\infty e^{-pt^2} J_{3/2}(k_0 a e_c \sqrt{1 + t^2}) dt \quad (5.23)$$

Where  $J_{3/2}$  is the Bessel function with base 3/2,  $p = 2gf/u^2$ ,  $k_0 = g/U_\infty$  and  $f$  is the depth of the spheroid major axis. Considering a spheroid with  $f = 0.25$  it is possible to compute the drag coefficient predicted by this theory for the present test case. Introducing the spheroid length  $L$  and its diameter  $d$ , the drag coefficient is defined as.

$$C_w = \frac{D_w}{\pi/6 \rho g L d^2} \quad (5.24)$$

Figure 5.10 displays a comparison of wave drag coefficients between Havelock theory and the present method, for several values of Froude numbers (or of flow velocity). Recalling equation (4.12) we compute the pressure on the body as:

$$P = P_\infty + \frac{1}{2} \rho (U_\infty^2 - U^2) - \rho g z,$$

where  $z$  states for the height of the point in the considered framework. The drag coefficient can be obtained as integral of the pressure coefficient as:

$$C_p = \frac{P - P_\infty}{1/2 \rho U_\infty^2}$$

$$C_w = \frac{1/2 \rho U_\infty^2}{\pi/6 \rho g L d^2} \int_S C_p dS$$



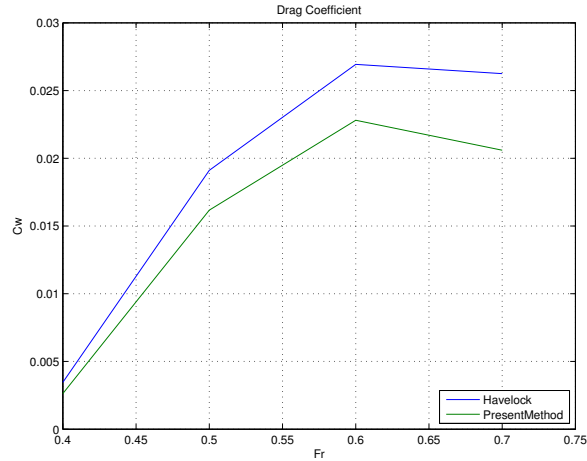


**Figure 5.10:** Wave drag coefficients as function of Froude number. The blue line represents the Havelock theory, and the green line represents the results of the present method

It can be seen that the two curves have a similar behavior. The present method appears however to underestimate the drag. This error seems to be dependent on the Froude number, since it increases with the velocity. The same kind of error pattern has been observed also for different values of the depth  $f$ . This problem appears to be linked with what pointed out in Figure 5.9. Since the present method underestimates the height of the waves, it also underestimates the energy dissipated in the wave creation process leading to an underestimation of the drag force.

In the present work the wave coefficient only depends on the Froude number, as reported by Newmann in [22] (page 31) this follows the so-called Froude's hypothesis. This hypothesis states that the wave drag coefficient only depends on the Froude number, with a complete separation from the viscous resistance. This is confirmed by experimental data only when we are in presence of a thin boundary layer (theoretically of negligible thickness). This verified especially for very big hulls, when the Reynolds number  $Re = \rho U_\infty L_{boat} / \mu$  is higher than  $10^5$ ,  $\mu$  being the viscosity of the fluid.

## 5.2 Wigley Hull

This chapter will describe how our model deals with a surface piercing body. To treat this kind of problems, some modifications are required, especially in the mesh generation part, as in the previous test case the body and the free surface were interacting only indirectly, while now they are in contact. To give the algorithm more generality several tools of the OpenSource library OpenCascade [6], have been integrated. In particular, OpenCascade routines have been used to import and query CAD descriptions of the hull, so as to place the mesh points on the actual boat geometry.

To have some comparison with numerical and experimental data, the Wigley hull is the model considered for this test case. Given its simple shape the Wigley hull is in fact a commonly used benchmark in hydrodynamics simulations and several experimental data for such geometry are available in the literature.

### 5.2.1 Wigley Hull formulation

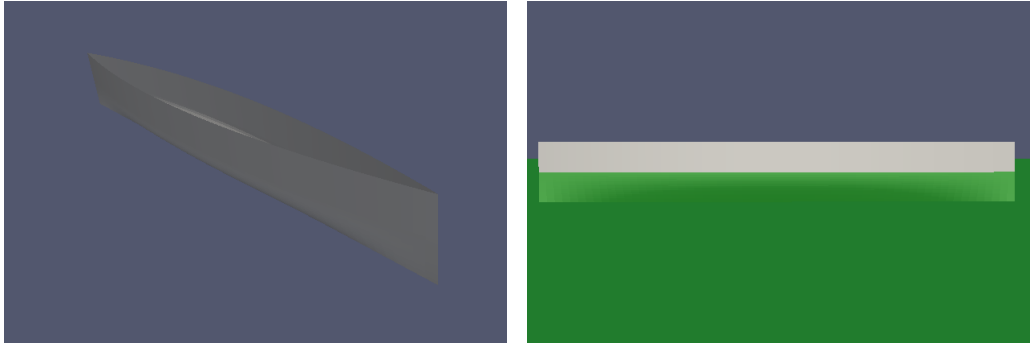


**Figure 5.11:** On the left, the CAD surfaces of the Wigley hull. The picture on the right shows the displacement imposed.

The Wigley Hull is analytically described by the following equation

$$y(x, z) = \frac{B}{2} \left[ 1 - \left( \frac{2x}{L} \right)^2 \right] \left[ 1 - \left( \frac{z}{T} \right)^2 \right] \quad (x, y) \in [-1, 1]^2. \quad (5.25)$$

Where  $y$  is the span of the hull,  $x$  its length and  $z$  its depth; in the present calculations the hull length used is  $L_{boat} = 2.5\text{m}$ , the span of the whole hull  $B = 0.25\text{m}$ , and its total depth beneath the undisturbed free surface is  $T = 0.15625\text{m}$ .

This geometrical configuration coincides with that of a set of experiments performed at the university of Tokyo [18], which will be used as a benchmark in this

test case. Six different velocities will be tested in order to compare them with the experimental results of [18]. The Froude number is defined again as

$$Fr = \frac{U_\infty}{\sqrt{gL_{boat}}} \quad (5.26)$$

## 5.2.2 Domain of the problem

The domain is extremely similar to that used for the submerged spheroid. The numerical tank of dimension  $L_{\infty x} \cdot L_{\infty y} \cdot L_{\infty z}$ , while the free surface is still located at  $z = 0$ . The hull is located at the center of the free surface.

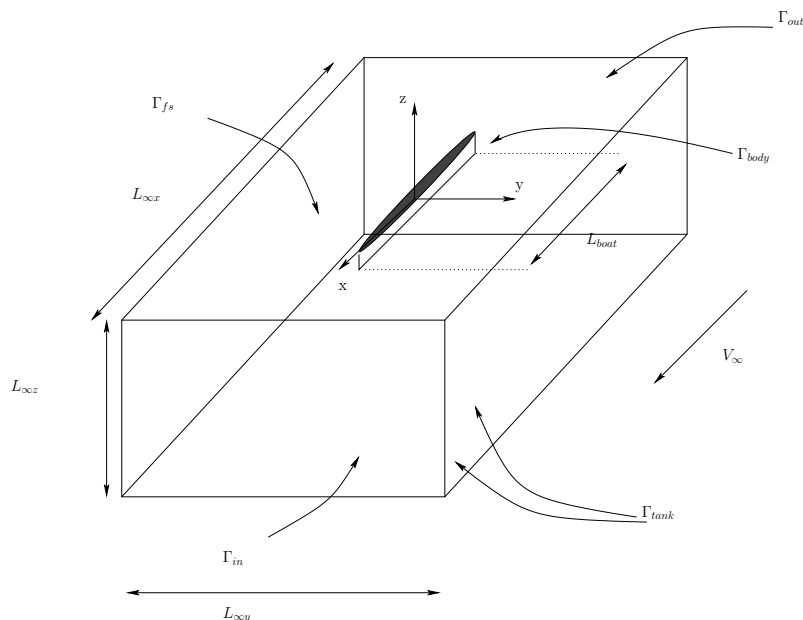


**Figure 5.12:** A sketch of the numerical domain. The wigley hull is placed in the center of the free surface. In the picture it is possible to see also the outer tank set with  $L_{\infty x}, L_{\infty y}, L_{\infty z}$ . The fluid enters from  $\Gamma_{in}$ ,  $\Gamma_{tank}$  are the lateral surfaces and the bottom

Figure 5.12 shows a sketch of the Wigley hull test case domain, the upper part is the free surface, where the waves are simulated. In the first tests of this section it was used a prebuilt mesh based on the expected waves position, depicted in Figure 5.13.

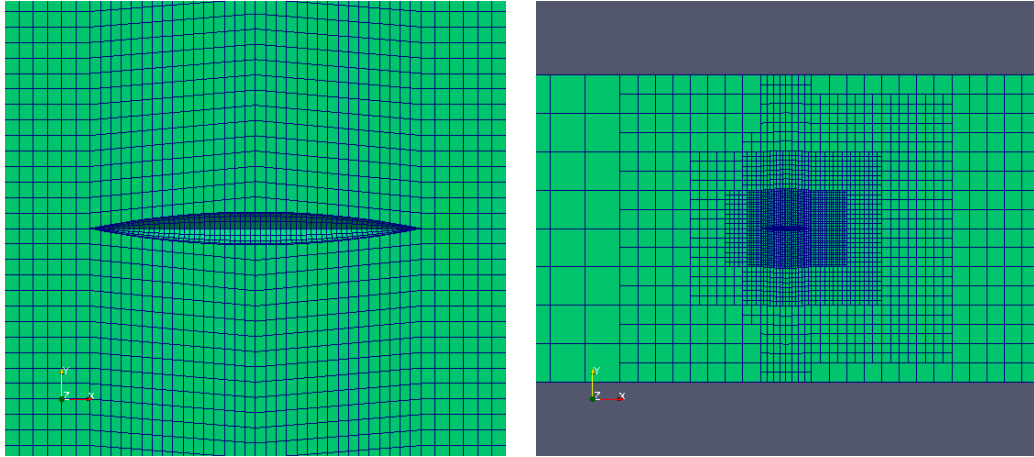


**Figure 5.13:** Views of the mesh generated for the Wigley hull test case. On the left a detail of the mesh around the Wigley hull. On the right, the free surface mesh and its gradual and non conformal refinement around the boat

On the boat, the grid is composed of 4 cells along the height of the hull, and 32 cells along its length. On the free surface, the mesh is set to be more refined around the hull and, to concentrate the degrees of freedom where the waves are expected to be.

### 5.2.3 Qualitative analysis of the wave pattern

As done for the prolate spheroid the purpose of the present section is to understand whether the method gives consistent results in reproducing the Kelvin wave pattern. The behavior expected is similar to that highlighted for the spheroid. The V-shape wave should be more evident as the Froude number increases, and the transverse wake should be present after the boat. Figures 5.14, 5.15, 5.16, 5.17, 5.18, 5.19 show flow visualizations of the simulations performed at each of the six Froude numbers considered.

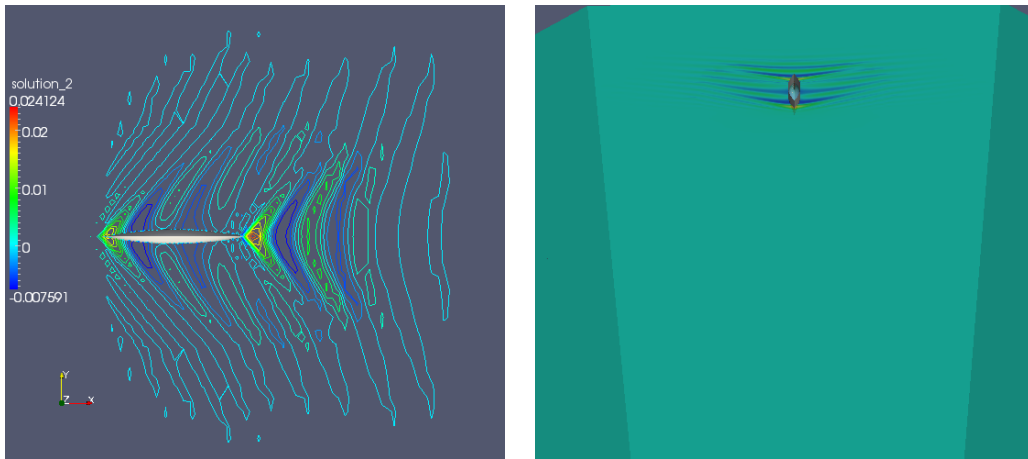


**Figure 5.14:** On the left, isolines representation on free surface elevation for  $Fr = 0.250$ . On the right, a view of the hull advancing in calm water, in which the external boundaries of the flow domain are also shown. The plots are colored according to water elevation.

The main difference from what seen with spheroid wake is the presence of a double V-shape pattern, generated by pressure peaks occurring both on the bow and on the stern. Between the peaks of the stern, the transverse wave can be clearly observed, another transverse wave system is formed between the bow and stern peaks.

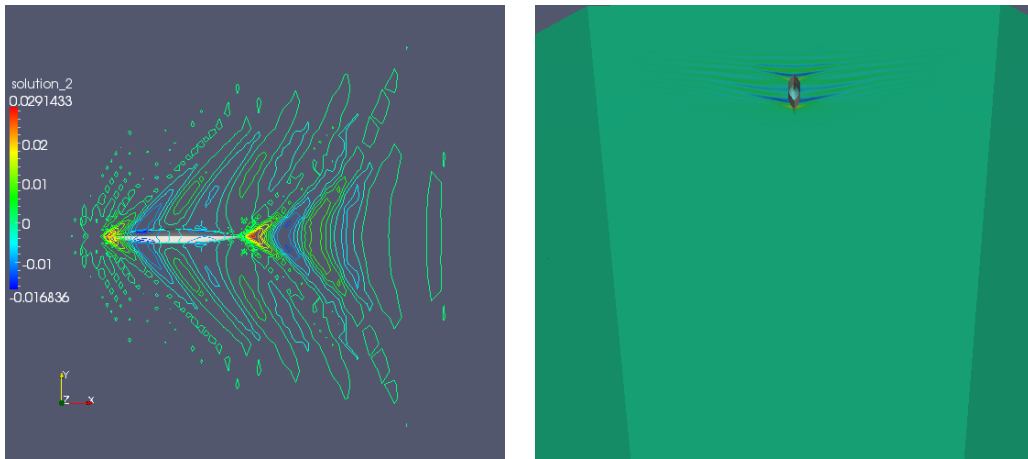


**Figure 5.15:** On the left, isolines representation on free surface elevation for  $Fr = 0.267$ . On the right, a view of the hull advancing in calm water, in which the external boundaries of the flow domain are also shown. The plots are colored according to water elevation.

At the highest Froude numbers the featherlets in the bow system are clearly

visible, and so are the ones in the stern system. As observed in experimental results, the two highest peaks are located around the bow and immediately after the stern.

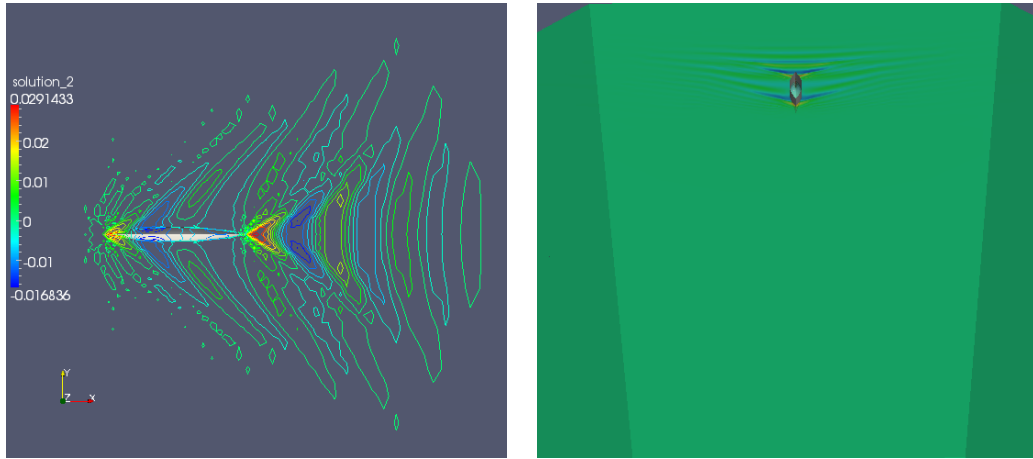


**Figure 5.16:** On the left, isolines representation on free surface elevation for  $Fr = 0.289$ . On the right, a view of the hull advancing in calm water, in which the external boundaries of the flow domain are also shown. The plots are colored according to water elevation.

Even at Froude  $Fr = 0.289$  observing the stern system it is visible the formation of the typical transverse wave clearly observable in the nature.

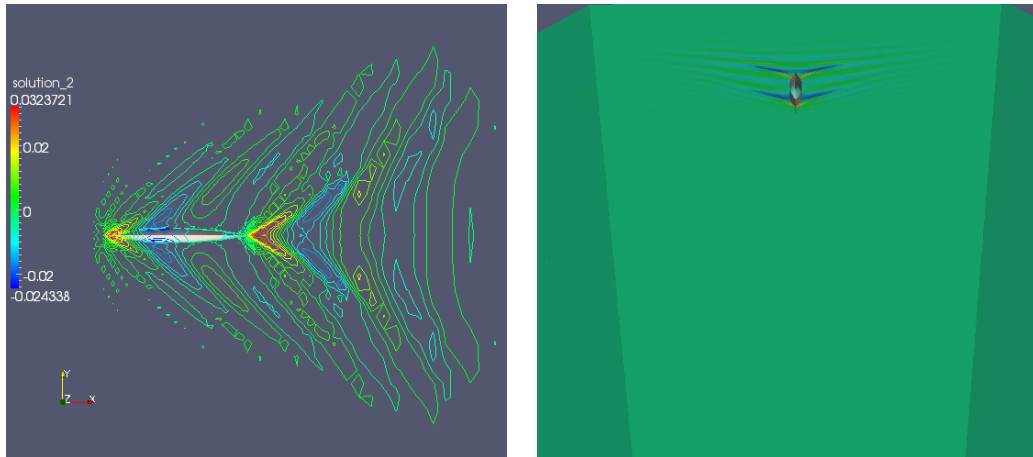


**Figure 5.17:** On the left, isolines representation on free surface elevation for  $Fr = 0.316$ . On the right, a view of the hull advancing in calm water, in which the external boundaries of the flow domain are also shown. The plots are colored according to water elevation.

Just as observed in the case of the submerged prolate spheroid, increasing the Froude number makes the V-shaped wave system (with its typical featherlets) more visible.

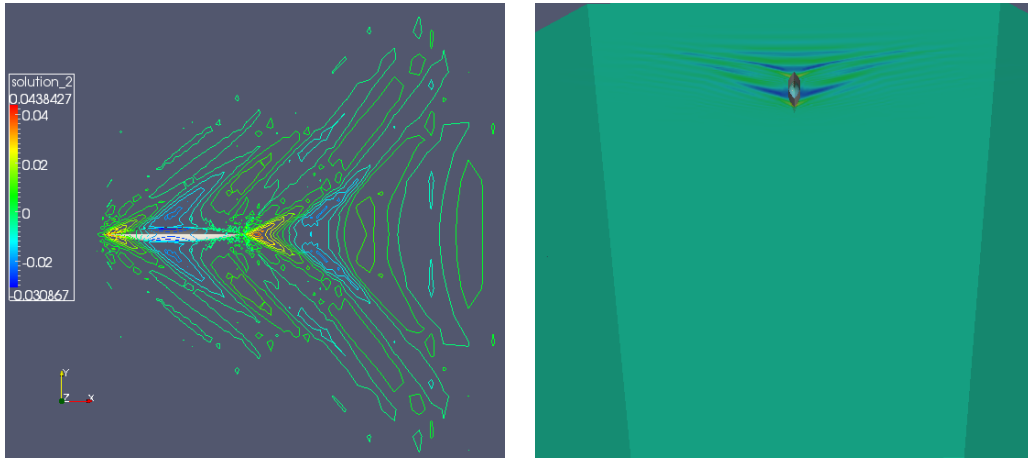


**Figure 5.18:** On the left, isolines representation on free surface elevation for  $Fr = 0.354$ . On the right, a view of the hull advancing in calm water, in which the external boundaries of the flow domain are also shown. The plots are colored according to water elevation.

For  $Fr = 0.354$  and  $Fr = 0.408$  the featherlets presence is clearly visible from the location of the water height peaks.

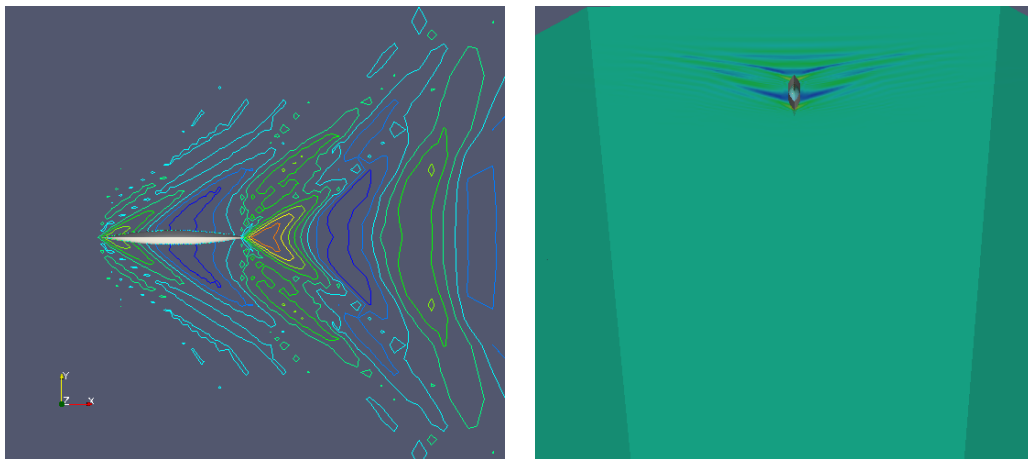


**Figure 5.19:** On the left, isolines representation on free surface elevation for  $Fr = 0.408$ . On the right, a view of the hull advancing in calm water, in which the external boundaries of the flow domain are also shown. The plots are colored according to water elevation.

Also in this case, we can see the double V-shape wave. The peaks are more evident than in the previous case, due to the higher Froude number. It is important to highlight that the present linearized method is more accurate at smaller Froude numbers because, in such a case, the waves are smaller therefore the hypotheses used for the linearization are more realistic. Another peculiar characteristic of the wave pattern is that the wavelength on the waterline on the hull increases along with the Froude number. This is typically observed with nonplaning hulls.



## 5.2.4 Free surface elevation on the water line

The comparison between the water elevation, and experimental results of the University of Tokyo is now presented in figure 5.20

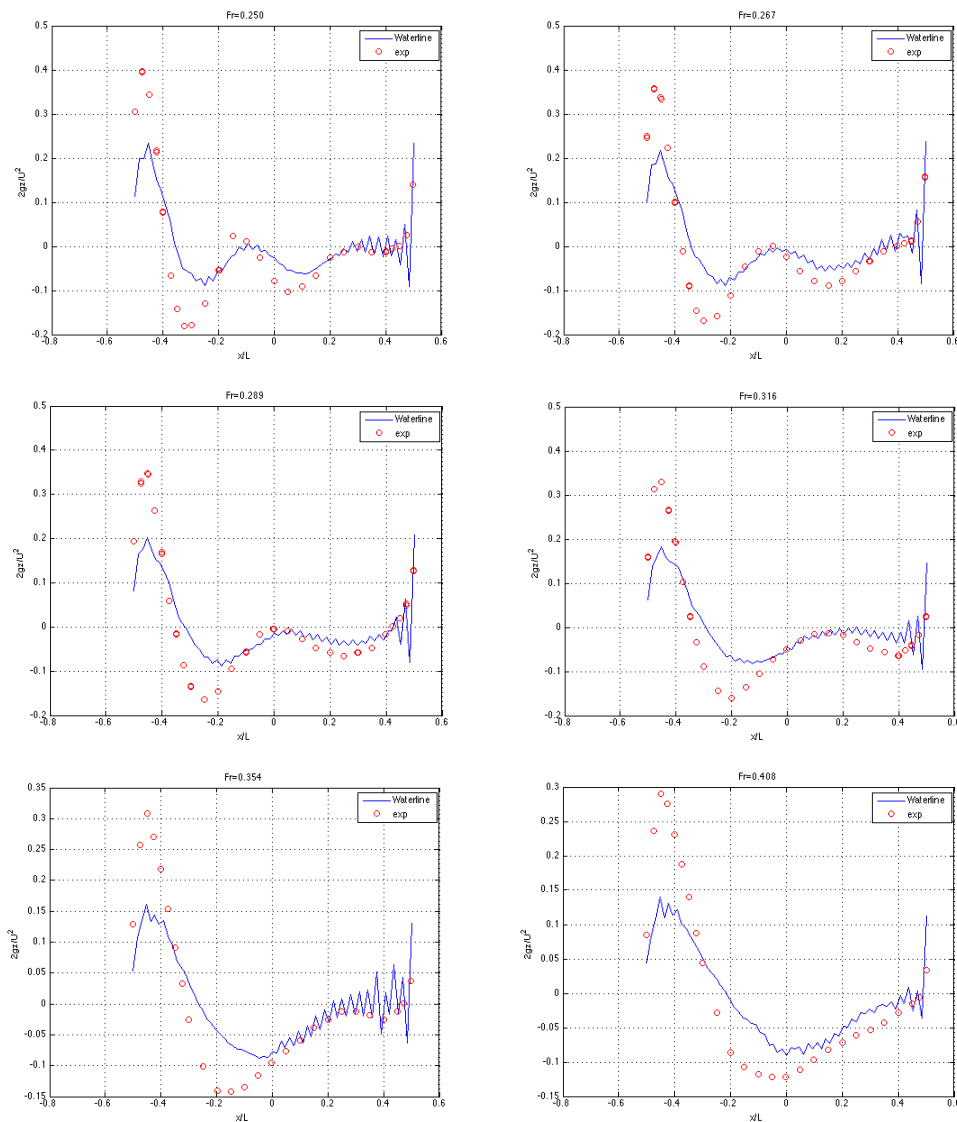


**Figure 5.20:** Non dimensional free surface elevation  $2gz/U_\infty^2$  on the Wigley hull surface as a function of non dimensional longitudinal coordinate, at different Froude numbers. The blue continuous line represents the result of the present method. The dots represent the university of Tokyo measurements [18]

Figure 5.20 shows a comparison between experimental and computed wave

heights along the boat, for  $Fr = 0.250, 0.267, 0.289, 0.316, 0.354, 0.408$ . It can be seen that in agreement with the experimental results the positive peak on the hull is just after the bow and that near the stern there is another positive peak. The plots suggest that, from a quantitative point of view, the software reproduces rather correctly the horizontal position of the peaks. Also the wavelength along the hull is correctly reproduced. As the Froude number increases the experimental water wave wavelength increases. The present method is able to reproduce such behavior. So in the location of the peaks remains quantitatively correct for all the Froude number considered. Despite this, the present model clearly underestimates the wave elevation, which also presents a significant high frequency oscillation, in particular around the stern of the hull. The former problem is probably due to the choice of linearized free surface conditions. A linearized model is in fact not able to fully recover the wave creation process, as suggested in [24]. The instability around the stern instead may have two different causes. The first hypothesis is that since our problem has a very strong transport term due to the external flow the SUPG strategy (the way we have implemented it) may not be enough to tackle it completely. The second hypothesis is that the choice of finite element spaces may not be proper. If this second hypothesis is true this problem arises only when a surface piercing body is considered since we didn't see such a problem in the submerged spheroid case. The results of figure 5.20 have been obtained using a linear continuous approximation for  $\phi$  and  $\partial\phi/\partial x$  and a piecewise constant approximation for  $\partial\phi/\partial n$ . This choice might not be the best, because it causes the SUPG strategy to be present only in the first derivative of the potential  $\phi$ , as explained in the previous chapter, the usage of the piecewise constant approximation might also causes the underestimation of the peak heights. The most natural choice would be a quadratic continuous approximation for  $\phi$ , a linear discontinuous approximation for  $\partial\phi/\partial x$ , and a piecewise constant approximation, or alternatively a linear discontinuous approximation, for  $\partial\phi/\partial n$ . In the following sections we will investigate these two hypotheses, in order to understand better the nature of such an oscillation.

### 5.2.5 Local Refinement

As highlighted in the previous chapters, the choice of having an unstructured grid allows for a local refinement strategy. In this way it should be possible to concentrate the degrees of freedom where the solution has deeper gradients. The same Kelly Error Estimator already used in the spheroid test case of Chapter 3 has been here used. The local refinement strategy has been set so that at every step the thirty percent of cells with highest error estimator are refined. The cells are not refined on the hull. The hull mesh is in fact refined before the simulation

starts. The cells on the free surface adjacent to the hull are forced not to become smaller than the ones already refined on the hull. Now that a refinement cycle has been set, it is possible to perfect the SUPG stabilization strategy. In the previous chapter, following [1] the SUPG stabilization has been defined as

$$H_j(x)^{SUPG} = H_j(x) + \alpha h \nabla H_j(x) \cdot \frac{v(x)}{\|v\|} \quad (5.27)$$

only the asymptotic flow has been considered in  $v(x)$ . Namely  $v(x) = U_\infty$ . It has been seen that this was good enough in the case of the submerged spheroid, since the streamlines on the free surface are almost parallel to the main external flow. Now that a surface piercing body is considered, the streamlines follow the shape of the body. Introducing this further approximation may worsen the already unstable situation near the stern of the boat. In the refinement cycle there is the possibility to use the potential solution at the previous refinement step, namely  $\phi_{old}$ , to compute the velocity  $v(x)$  as

$$v(x) = \nabla \phi_{old}(x) + U_\infty \quad (5.28)$$

In this case local refinement may play a key role because, differently from the test cases of chapter 3, global refinement strategy has an extremely high computational costs. The hull discretization used is the same one considered in the previous section.

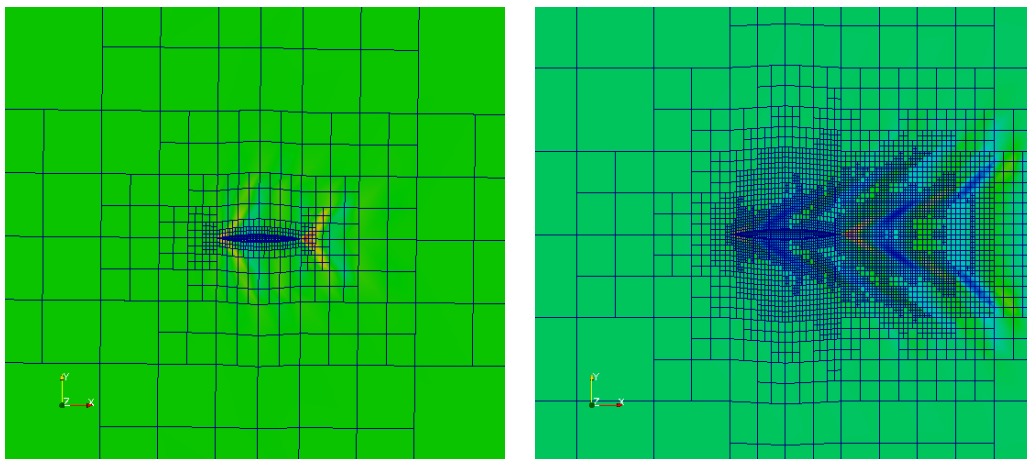


**Figure 5.21:** On the left, the free surface mesh at the initial level of refinement. On the right, the free surface mesh obtained after five refinement cycles

## 5.2.6 Free surface elevation on the water line with local refinement

In this section the flow field is computed using local refinement strategy for the same six Froude numbers of Tokyo university experiments [18]. The results are compared with the previous ones in order to highlight the differences between the two calculations. This comparison is presented in figure 5.22.

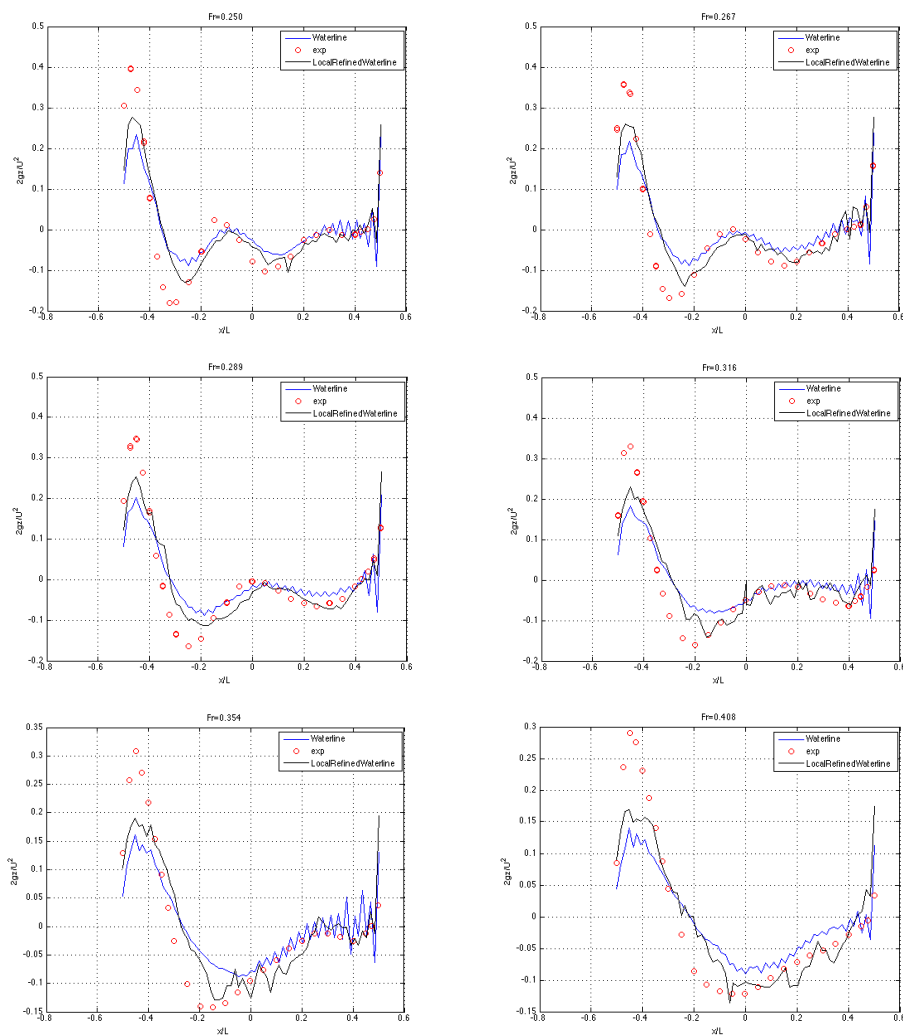


**Figure 5.22:** Non dimensional free surface elevation  $2gz/U_\infty^2$  on the Wigley hull surface as a function of non dimensional longitudinal coordinate, at different Froude numbers. The blue continuous line represents the waterline obtained with the prebuilt mesh. The red dots represent the experimental results as reported in [18]. The black continuous line represents the waterline obtained with the local refinement strategy

Qualitatively, the peaks computed by the present method are around the bow and near the stern. This is consistent with the experimental data. The horizontal peak position is quantitatively quite well recovered especially for  $Fr = 0.267$ ,  $Fr = 0.289$  and  $Fr = 0.316$ . The principal wavelength is well visible, and accordingly with the experimental data it increases as the Froude number increases. The local refinement strategy has improved the estimation of peaks heights and, for  $Fr = 0.267$ ,  $Fr = 0.289$ ,  $Fr = 0.316$ , it has reduced the amplitude of the high frequency oscillation. The underestimation of the peaks is still present and this is consistent with the linearization adopted in the present work. In Figure 5.23 we show the comparison with other two classic linearized method as reported in [24].

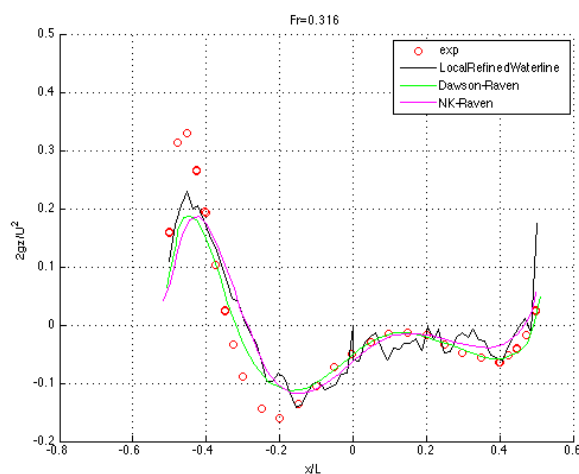


**Figure 5.23:** Non dimensional free surface elevation  $2gz/U_\infty^2$  on the Wigley hull surface as a function of non dimensional longitudinal coordinate, at different Froude numbers. The black continuous line represents the waterline obtained with the local refinement strategy. The red dots represent the experimental results as reported in [18]. The green line represents the result obtained using the classic Dawson method. The magenta line represent the result obtained using the classic Neumann-Kelvin method

All the linearized methods considered underestimate the height of the peaks in the waterline. Thus it was correct our comment that the underestimation was due to the choice of a linearized boundary condition on the free surface. Our model has less numerical dissipation than the other linearized strategies because we have applied a strongly consistent method in the upwinding. A drawback of this strategy appears to be the instability at the stern. Nonetheless the instability may be due to the choice of finite element spaces. In the next section we will investigate another possibility for these spaces and, at the present moment, we are testing other combinations.

For the Wigley hull at two of the Froude numbers considered in the local refinement tests, we perform a qualitative comparison with the simple model described in Chapter 4.

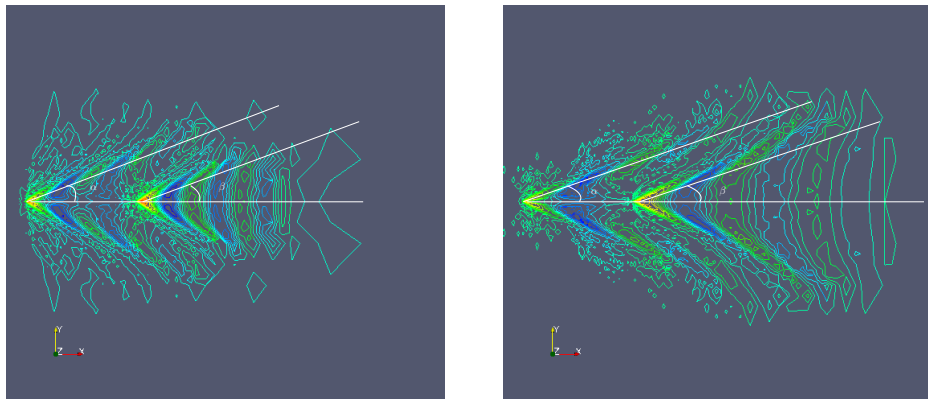


**Figure 5.24:** On the left, the Kelvin wave angle for  $Fr = 0.267$  and on the right, the Kelvin wave angle for  $Fr = 0.354$

**Table 5.1:** Kelvin angle for the Wigley hull

Fr	angle $\alpha$	angle $\beta$
0.267	21°	20°
0.354	19°	18°

The two angles remain almost constant varying the Froude of the simulation. This fact agrees with what has been introduced, using the simple model in Chapter 4, and confirms that the present method is able to reproduce one of the most important feature of a Kelvin wake.

The local refinement strategy has a disadvantage in respect to the prebuilt mesh one. This strategy needs to solve many linear system to refine the grid where the gradients of the unknowns are the highest. It also uses a large number of cell in its latest cycle. This situation increases the computational costs of the present method, the results of the local refinement strategy have been obtained in about 8 hours each. The results obtained with the prebuilt mesh where instead obtained in about 4 hours.

The local refinement strategy has improved our method since the peaks over the waterline are better recovered. Their horizontal position is consistent with the experimental data, as we have already stress using the prebuilt mesh. The oscillation is still present especially at very high Froude numbers, we can see that for  $Fr = 0.289$  the oscillation has been considerably reduced.

## 5.2.7 Comparison with other models

In this section we want to compare the results of our hybrid BEM with those obtained with different models. In a first case we will consider a continuous linearized BEM in which the presence of the edges is taken into account via the implementation of a peculiar technique proposed by Grilli and Svendsen [12, 11]. This continuous linearized method is a modification of our hybrid model. We have considered linear continuous approximation for all of our unknowns:  $\phi$ ,  $\partial\phi/\partial n$  and  $\partial\phi/\partial x$ . Since our considerations in section 3.3, about the problem of having sharp edges in the domain, we have included some non trivial modifications in order to treat properly these edges. The SUPG stabilization is implemented in the same way we have used in the previous section. The simulation is done using the same local refinement strategy of the previous section.

In a second case, the present model will be compared to an unsteady potential model with fully non linear free surface boundary conditions [20].

Firstly we compare our method with the continuous linear BEM that we have modified with the addition of the double nodes

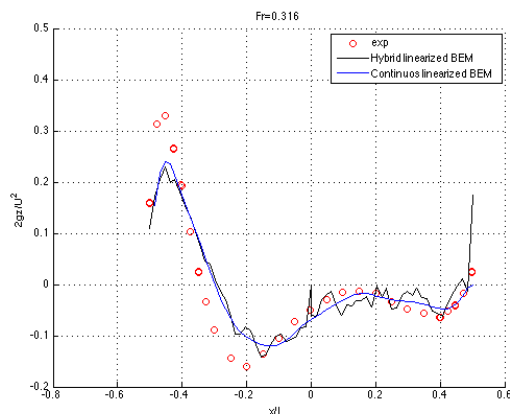


**Figure 5.25:** Non dimensional free surface elevation  $2gz/U_\infty^2$  on the Wigley hull surface as a function of non dimensional longitudinal coordinate, at different Froude numbers. The black continuous line represents the waterline obtained with our hybrid BEM. The red dots represent the experimental results as reported in [18]. The blue line represents the result obtained using a continuous BEM with the double nodes as explained in [12, 11].

We can see that the continuous BEM recovers the height of the peaks as well as our hybrid BEM. As we have stressed in the previous sections, the underestimation of the waterline is due to the choice of the linearized free surface condition (5.1c). We can also notice that the instability present in the waterline obtained with the hybrid BEM is erased using a continuous approximation both for  $\phi$  and  $\partial\phi/\partial n$ . So we can infer that this instability is not due to a lack of performance

of the SUPG stabilization, since it is the same in both cases. We instead come to understand that the instability is related to the usage of a discontinuous solution when a surface piercing body is considered. For this reason, a more accurate study of the boundary condition will be performed because this problem does not arise if a submerged body is considered. The continuous solution has a major drawback since it requires the non trivial treatment of the edges. If we do not introduce such a treatment, the continuous solution results extremely inaccurate, since the normal derivative approximation is an average of the values on the boat and on the free surface, which are extremely different. Yet, even when a discontinuous solution is considered, the potential second derivative appearing in equation (5.1c), which should only be computed on the water free surface, seems to have a small contribution of the boat surface potential. This might lead to the instabilities observed in the solutions, which are not observed in the continuous BEM modified with the edge treatment. In fact, such treatment consists in doubling the nodes on the domain edges, so as to separate the two sides of the edge. The correct choice of spaces that might tackle the oscillation is currently under investigation. In Figure 5.26 we compare our method with the non linear unsteady BEM

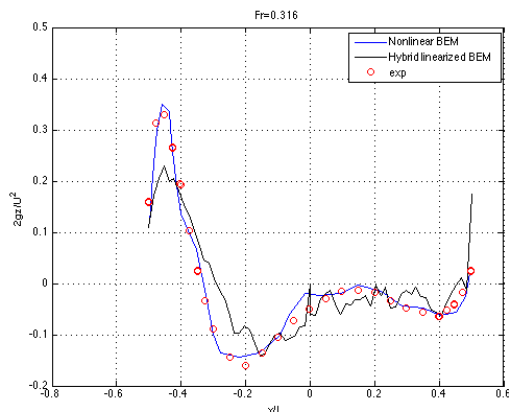


**Figure 5.26:** Non dimensional free surface elevation  $2gz/U_\infty^2$  on the Wigley hull surface as a function of non dimensional longitudinal coordinate, at different Froude numbers. The black continuous line represents the waterline obtained with our hybrid BEM. The red dots represent the experimental results as reported in [18]. The blue line represents the result obtained using a non linear BEM as explained in [20].

We see that the non linear BEM recovers more accurately the waterline. It has a greater computational cost than our method but it is able to simulate completely the phenomena related to this kind of water waves. For this reason, the fully non linear potential model will be used in the next section as a benchmark to evaluate how the linearized BEM performs on a CAD hull of industrial interest.



### 5.3 DTMB5415

In this chapter we describe how our model treats a hull characterized by a complex geometry. By complex geometry we intend here a shape which is not represented by a single (and possibly simple) analytical equation, but it is prescribed by means of a CAD file, which is typically composed by a set of b-splines patches. We consider a DTMB5415 hull. Such hull was conceived in 1980 as a preliminary design for a navy surface combatant, and later it became a common benchmark for hydrodynamic simulations.

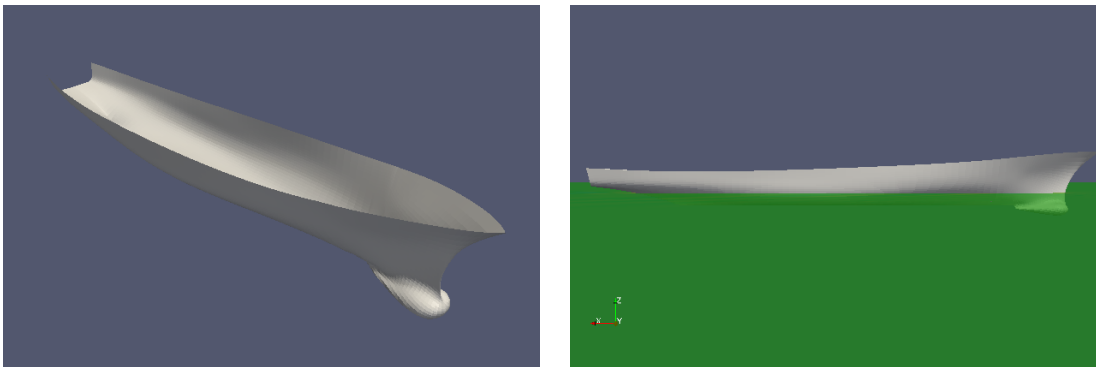


**Figure 5.27:** On the left, the CAD model of DTMB5415 hull. As can be seen the hull presents both a sonar dome and a transom stern. The picture on the right shows the chosen displacement imposed, in which the dry transom stern is clearly visible.

Even if no full scale ship exists this model is in fact very used in naval literature for the presence of both a sonar dome and a transom stern. In the present work we have considered a dry transom stern in order to test the model developed without the introduction of additional treatments needed at the transom stern. The primary purpose of the present work is to investigate the possibility of use a hybrid BEM to compute free surface flows. For this reason we didn't want to add a treatment for the transom stern. Some possible ways of treat such a typical situation, in naval engineering, is under investigation at the moment.

The geometrical configuration of the domain is similar to that reported in Figure 5.12. We have decided to maintain the same approximations used in the previous sections, *i.e.* a linear continuous approximation for  $\phi$ ,  $\phi_x$  and a piecewise constant approximation for  $\phi_n$ . In the numerical simulation we have considered the initial mesh shown in Figure 5.28.

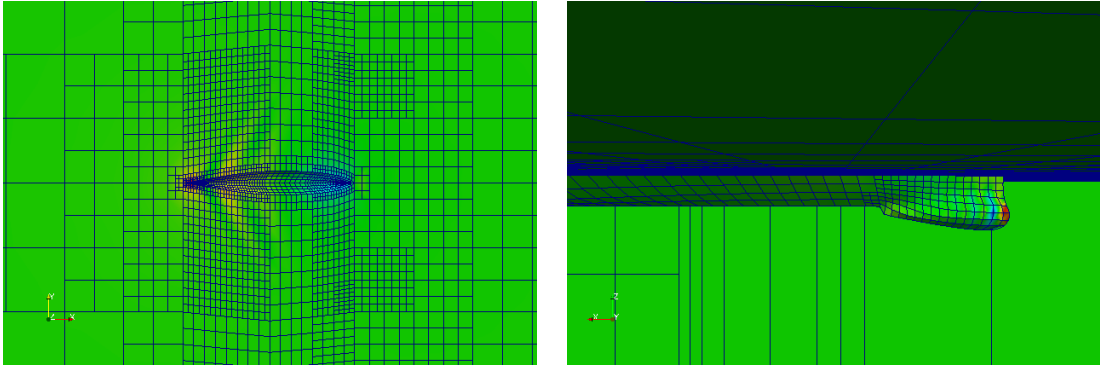


**Figure 5.28:** Views of the mesh generated for the DTMB5415 hull test case. On the left, a detail of the mesh around the hull. On the right, the mesh around the sonar dome of the hull.

The picture on the left shows the initial prebuilt mesh around the DTMB5415 hull. We have chosen a more refined mesh on the bow of the hull in order to represent properly the sonar dome high curvature shape. Since our algorithm uses the CAD of the hull to generate the mesh, we are able to reproduce quite naturally this geometry. This is achieved making use of the software library OpenCASCADE [6] for the generation and the managing of CAD models.

In the Wigley hull test case we have seen that the results are improved using a local refinement strategy. So, also in this test, we have decided to have three refinement cycles with the usual Kelly error estimator. In this way we can choose whether to use or not the SUPG strategy as discussed in section 5.2.5.

The final numerical simulation is performed on the following mesh

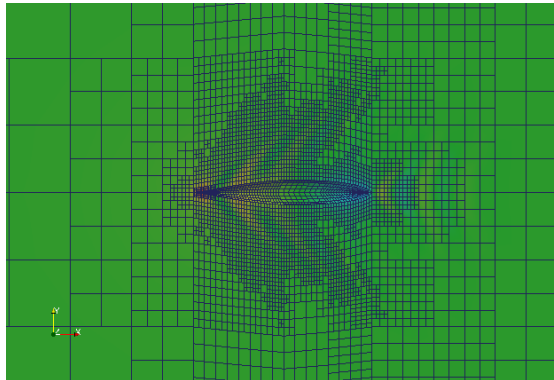


**Figure 5.29:** View of the final mesh around the DTMB5415 after 3 local refinement cycles.

As in the Wigley hull test case, we impose that the mesh is refined only on the free surface. We remark that having unstructured non conformal grids

is extremely important in this test case, because cell dimensions are extremely variable to adapt to region where the high curvature of the geometry determines steep gradients of the flow field.

### 5.3.1 Free surface elevation on the water line

In naval literature there aren't any experimental data for the DTMB5415, with the considered displacement, so we have decided to compare our results with what is obtained with the full nonlinear unsteady potential model explained in [20].

Figure 5.30 reports the waterline obtained with the two models at  $Fr = 0.175$ , and  $Fr = 0.2$ .

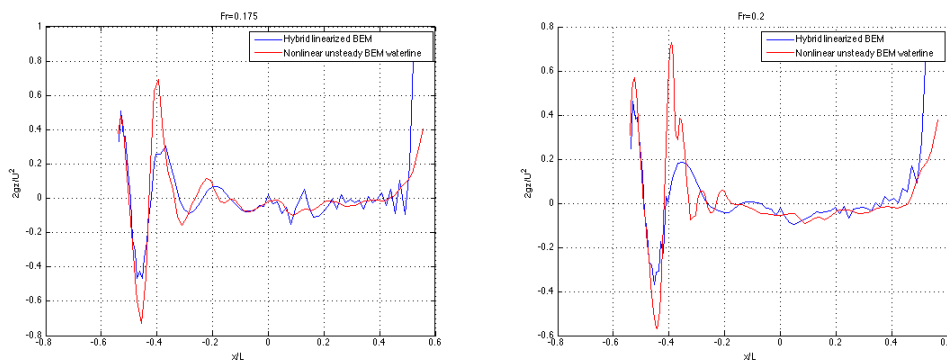


**Figure 5.30:** On the left, the simulation for  $Fr = 0.175$ , on the right, for  $Fr = 0.2$ . Non dimensional free surface elevation  $2gz/U_\infty^2$  on the Wigley hull surface as a function of non dimensional longitudinal coordinate, at different Froude numbers. The blue continuous line represents the waterline obtained with the present hybrid BEM. The red line represents the waterline using a nonlinear unsteady BEM.

The comparison shows that the present method reproduces rather well the first two peaks on the waterline elevation. In this case, not only the horizontal position of such peaks is recovered but also their height is reproduced with sufficient accuracy; especially for the first positive peak. We can also see that the macroscopical behavior of the waterline is well reproduced, *i.e.* a precise wavelength is present along the boat length. This wavelength increases with the Froude number as we have stressed in the previous test cases.

For  $Fr = 0.2$  the instability highlighted in the Wigley hull test case is still present, but for this Froude number it seems less critical. The horizontal positions and heights of the secondary peaks are not well recovered away from the bow. In addition there is quite a large difference near the stern of the hull; this fact may depend on the linearized free surface boundary condition employed. As explained

in section 4.3 the free surface is considered undisturbed *i.e.* the nodes can't follow the surface of the hull. In the reference BEM instead the free surface is free to move and it is forced to follow the hull shape.

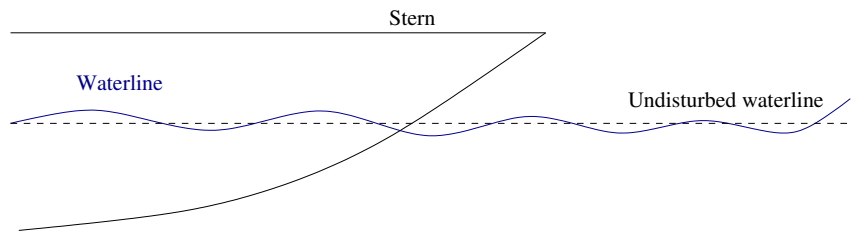


**Figure 5.31:** Qualitative sketch of the stern of the DTMB5415.

Hence some differences are expected, because the elevation computed by the present method does not take into account the effective shape of the hull. From Figure 5.31 it can be seen that the problem may be critical around the stern. In the Wigley hull test case this was a minor effect due to its peculiar shape with a vertical sharp stern. This fact may be an explanation of the differences between the two waterlines near the stern, which is nearly horizontal. We want to point out that in the non linear simulation the waterline tends to extend at the stern assuming a more hydrodynamic shape. In our linearized potential model the shape of the body remains quite bluff forcing the flow to have great acceleration near the stern, resulting in an increased height of the waterline. For these two reasons the results of our method on this kind of sterns might not be completely reliable. Also in this case, we compute the Kelvin wake angle for the considered DTMB5415 hull.

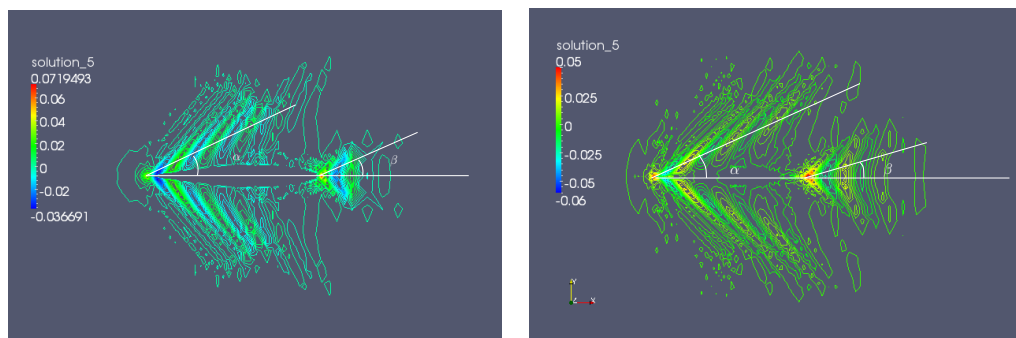


**Figure 5.32:** On the left, the Kelvin wave angle for  $Fr = 0.175$ , on the right, the angle for  $Fr = 0.2$

**Table 5.2:** Kelvin angle for the DTMB5415 hull

Fr	angle $\alpha$	angle $\beta$
0.175	25°	23°
0.2	23°	18.5°

As stressed for the two previous test cases, in sections 5.1 and 5.2, our hybrid BEM is able to recover the physical behavior of free surface flows sufficiently well.



# Chapter 6

## Conclusions

This work has been carried out at Matlab laboratory, at SISSA, in Trieste. The first purpose of the present thesis was the implementation of a new hybrid boundary element method able to solve the Laplace equation. We have successfully tested such a strategy on three different test cases and the results are in agreement good with the reference continuous methods already available at Matlab. The hybrid method has proved to treat easily the presence of sharp edges, in presence of which the continuous method needs the implementation of an *ad hoc* strategy [12, 11].

The second goal was the modification of the hybrid method in order to treat the linearized free surface boundary condition (5.1c) for the simulation of free surface flow past cruising ships. Following the idea of C.W. Dawson [8] we have relied on upwind techniques to recover the derivatives in the linearized boundary condition and suppress unphysical upstream waves. But differently from Dawson, we have used a weak formulation with a SUPG strategy, [1], to be able to use unstructured non conformal meshes. This possibility plays a key role in many of our simulations since we deal with big domains and the solution gradients are concentrated in small regions surrounding the hull.

The results obtained with such a method have been compared with available analytical and experimental results in naval literature, both on a fully submerged spheroid and a Wigley hull. We have obtained quite good agreement especially for what concerns the submerged spheroid. On the Wigley hull we have matched the well established results of the linearized methods.

Finally, we have shown that our hybrid method is able of treat a hull design of industrial interest, the DTMB5415, without the need of any additional meshing tools. We have obtained rather satisfactory results, in comparison to a non linear method [20], in the computation of the waterline.

In all of our simulations of free surface flows, we have noticed an underestimation of the waves created by the motion of the body. This is consistent to our choice

of using a linearized free surface model (5.1c). This is particularly evident in the waterline computations on the Wigley hull and on the DTMB5415. To recover a more accurate wave pattern it is necessary to use at least a non linear potential method. Nonetheless our linearized method presents a great computational advantage since it takes only eight hours to produce its results while the non linear method requires about twenty hours.

Developing an efficient, robust and marketable software was definitely beyond the scope of this thesis. Yet, this work pointed out some problems and shortcomings that need to be addressed to increase the software accuracy and robustness. In particular the hybrid BEM presents a very peculiar oscillation on the waterline of every surface piercing body we have considered. We have attested that this instability does not depend on how we have implemented the SUPG in the imposition of (5.1c). We have also noted that such an instability does not appear if we consider a submerged body. For these reasons we believe that the oscillation depends on how a discontinuous approximations behaves when the two different boundary conditions on the potential normal derivative (5.1c), and (5.1b) are applied on neighbour cells. A specific study to isolate and possibly eliminate the problem is underway. We remark that the main purpose of this work was to implement a hybrid BEM and assess whether it is suitable for the application to ship hydrodynamics simulations.

The treatment of a sharp edge with a continuous method is not trivial but, as we expected, it becomes natural with a hybrid BEM approach. In the present thesis we have proved that such a strategy can be effectively applied to free surface flows, producing physically sound results. Yet, the results of this work show that if any industrial application is desired, more accurate mathematical studies on the coupling between free surface and body boundary condition is needed. In addition, this work has shown some important limitations of the physical model adopted. For this reason, industrial applications can be effective only if a proper treatment for transom stern hull is introduced and, more importantly, if in the ship design process the linearized method is used as a fast and possibly less accurate alternative to a nonlinear potential method.

Some developments of the presented method are still underway. The first is the substitution of the UMFPACK direct solver with the iterative method GMRES using an appropriate preconditioner. This different choice of the system solver should reduce the computational cost of the method, especially for the local refinement strategy. GMRES computational cost is proportional to the square of the degrees of freedom and the actual solving strategy to the cube, resulting in a bottle neck in many simulations. The choice, made at the beginning of this work, of using the direct UMFPACK solver has been done not to deal with the choice of a preconditioner. Another improvement to the local refinement strategy may come from a



different choice of error estimator. Yet, improves in this area are mandatory for any ship design proposal. The search of such an estimator as well as the study of an optimal preconditioner for iterative solvers were not a purpose of the present work.



# Bibliography

- [1] J. E. Akin. *Finite Element Analysis with Error Estimators*. Elsevier, 2005.
- [2] W. Bangerth, R. Hartmann, and G. Kanschat. deal.II – a general purpose object oriented finite element library. *ACM Trans. Math. Softw.*, 33(4):24/1–24/27, 2007.
- [3] W. Bangerth, T. Heister, and G. Kanschat. deal.II *Differential Equations Analysis Library, Technical Reference*. <http://www.dealii.org>.
- [4] K. A. Belibassakis, C. Feurer, Th. P. Gerostathis, A. I. Ginnis, P. D. Kaklis, J. Karigiannis, K. V. Kostas, D. Mourkogiannis, C. G. Politis, and A. Theodoulides. A BEM-Isogeometric Method with Application to the Wave-making Resistance Problem of Ship at Constant Speed. In *ASME 2011 30th Conference on Ocean, Offshore and Arctic Engineering*, 2011.
- [5] C.A. Brebbia. *The Boundary Element Method for Engineers*. Pentech Press, 1978.
- [6] OPEN CASCADE Company. OpenCASCADE technology. <http://www.opencascade.org>, 2013.
- [7] Frank S. Crawford. Elementary derivation of the wake pattern of a boat. *Am. J. Phys.*, 52:782–785, 1984.
- [8] C. W. Dawson. A practical computer method for solving ship-wave problems. In *Second International Conference on Numerical Ship Hydrodynamics*, pages 30–38, 1977.
- [9] Antonio DeSimone, Luca Heltai, and Cataldo Manigrasso. Tools for the solution of PDEs defined on curved manifolds with the deal.II library . *SISSA Technical Report*, 2009.
- [10] S. Grilli, J. Skourup, and I. A Svendsen. An efficient boundary element method for nonlinear water waves. *Eng. Analysis with boundary elements*, 1989.

- [11] S.T. Grilli and I.A. Svendsen. Corner problems and global accuracy in the boundary element solution of nonlinear wave flows. *Engineering Analysis with Boundary Elements*, pages 178–195, 1990.
- [12] Stephan T. Grilli, Philippe Guyenne, and Frédéric Dias. A fully non-linear model for three-dimensional overturning waves over an arbitrary bottom. *International Journal for Numerical Methods in Fluids*, 2001.
- [13] T. H. Havelock. The Wave Resistance of a Spheroid. *Proceedings of the Royal Society*, pages 275–285, 1931.
- [14] Luca Heltai. Step 34. [http://www.dealii.org/developer/doxygen/deal.II/step\\_34.html](http://www.dealii.org/developer/doxygen/deal.II/step_34.html), 2009.
- [15] Sriganesh R. Karur and P. A. Ramachandran. Orthogonal collocation in the non-conforming boundary element method. *Journal of Computational Physics*, 1995.
- [16] University College London, University of Reading, and University of Durham. Exterior Dirichlet problem for the Laplace equation. [http://www.bempp.org/tutorial\\_dirichlet](http://www.bempp.org/tutorial_dirichlet).
- [17] J. Tinsley Oden Mark Ainsworth. *A Posteriori Error Estimation in Finite Element Analysis*. Hoepli, 2000.
- [18] M.Ikehata, H.Tanaka, H.Adachi, M.Namimatsu, and S.Ogiwara. The summary of the cooperative experiment on Wigley parabolic model in Japan, 1983.
- [19] Andrea Mola. *Model for Olympic Rowing Boats*. PhD thesis, Politecnico di Milano, 2009.
- [20] Andrea Mola, Antonio DeSimone, and Luca Heltai. A stable and adaptive semi-Lagrangian potential model for unsteady and nonlinear ship-wave interactions. *Engineering Analysis with Boundary Elements*, 2013.
- [21] J. N. Newman and J. M. Clarisse. Evaluation of the wave-resistance Green function near the singular axis. *J Ship Research*, 38, 2004.
- [22] J. N. Newmann. *Marine Hydrodynamics*. the MIT Press, 1977.
- [23] Francis Noblesse, Fuxin Huang, and Chi Yang. The Neumann-Michell theory of ship waves . *J Eng Math*, 2012.

- [24] Hoyte C. Raven. *A Solution Method for the Nonlinear Ship Wave Resistance Problem*. PhD thesis, Technische Universiteit Delft, 1996.
- [25] David C. Scullen. *Accurate Computation of Steady Nonlinear Free-Surface Flows*. PhD thesis, University of Adelaide, 1998.
- [26] Ronal W. Yeung. Numerical methods in free-furface flows. *Ann Rev. Fluid. Mech.*, pages 395–442, 1982.